

OHIO STATE
UNIVERSITY
OCT 5 1961
LIBRARY

Kippen

OCT 6 1961

MONTHLY NOTICES

OF THE DOLE MEMORIAL LIBRARY

ROYAL ASTRONOMICAL SOCIETY

Volume 122 No. 6 1961

Published and Sold by the
ROYAL ASTRONOMICAL SOCIETY
BURLINGTON HOUSE
LONDON, W.1

Price £1 4s. 6d. (US \$3.50)
Subscription for volume £6 (US \$18)

NOW AVAILABLE

MEMOIRS
OF THE
ROYAL ASTRONOMICAL SOCIETY

VOL. LXVIII—PART III

CONTENTS

CLASSIFICATION AND RADIAL VELOCITIES OF
BRIGHT SOUTHERN GALAXIES

by

GERARD DE VAUCOULEURS

AND

ANTOINETTE DE VAUCOULEURS

AND

ANALYSIS OF LIME DARKENING OBSERVATIONS

by

A. KEITH PIERCE AND JOHN H. WADDELL

PRICE £1 (US \$3)

Orders to:

ASSISTANT SECRETARY, ROYAL ASTRONOMICAL SOCIETY,
Burlington House, London, W.1
England

MONTHLY NOTICES
OF THE
ROYAL ASTRONOMICAL SOCIETY

Vol. 122 No. 6

ON THE EFFECT OF A HELICAL MAGNETIC FIELD ON THE
POLARIZATION OF STARLIGHT

J. G. Ireland

(Communicated by F. Hoyle)

(Received 1961 January 26)

Summary

The observational data on the interstellar polarization of starlight is shown to be generally favourable to a helically twisted model of the spiral arm magnetic field. The data is, in some respects, seriously opposed to the normal cylindrical model. There is also evidence that a halo field dips through the galactic plane in interarm regions.

1. *Introduction.*—It was noted by Hiltner, several years ago, that interstellar polarization effects tend to attain a maximum intensity for stars in galactic longitudes close to 102° . The directions of polarization in such longitudes are close to being parallel to the plane of the Galaxy. These facts have been interpreted in accordance with the theory of Davis and Greenstein, which will first be briefly discussed.

According to this theory, the interstellar grains are needle-shaped. They are subject to hysteresis effects that cause their long axes to tend to become perpendicular to the magnetic field. They are otherwise free to rotate; in particular they rotate about short axes parallel to the magnetic field. Consider, now, initially unpolarized light travelling toward the Earth. The light has two independent directions of linear polarization, both perpendicular to the line of sight. At any point of the path of the light we choose one of these directions to lie in the plane determined by the line of sight and by the direction of the magnetic field at that point, the other component being taken perpendicular to this plane. Initially, the electric field components of the unpolarized light are closely equal. Scattering by the interstellar grains can produce measurable inequality, however, for the reason that the grains do not possess equal average projections in the two directions—the average projection perpendicular to the plane being the greater by a factor $(\cos \theta)^{-1}$, where θ is the angle between the magnetic field and the line of sight at the point in question. This causes the electric field component perpendicular to the plane to be more weakened by scattering than the component in the plane.

These considerations, relating to a particular point on the path of the light, have application to the case where the main scattering occurs within a particular localized interstellar cloud, provided the magnetic field inside the cloud can be taken to be approximately uniform. Then we have effectively the same plane (defined by the line of sight and the magnetic field) at all points of the light path within the cloud—and if scattering is unimportant outside the cloud, other parts of the light path need no discussion. Scattering causes a greater weakening of the electric field component perpendicular to the plane than of the component in

the plane, except in the special case where $\theta = 0$. Write A for the latter component, as measured by the terrestrial observer, and B for the former. The degree of polarization P is then defined by

$$P = \frac{A-B}{A+B}. \quad (1)$$

Now we can write $A = I \exp(-a \cos \theta)$, $B = I \exp(-a)$, where I is the initial unscattered intensity, and a is a constant for the particular cloud in question, depending on the size distribution and number of the grains that it happens to contain. Evidently P does not depend on I . Furthermore, since the observed values of P are $\ll 1$ we can infer that in general $a \ll 1$, since θ cannot be close to zero in all cases. With $a \ll 1$ we evidently have

$$P \simeq \frac{1}{2}a(1 - \cos \theta). \quad (2)$$

By determining observationally the maximum and minimum values of the electric field, the quantities A, B are obtained. The direction in which the maximum is found determines the plane of vibration containing the line of sight and the magnetic field. Although both the value of P and the plane of vibration are thus observable, the value of θ cannot unfortunately be found directly, since the value of a is not known—and indeed a presumably varies from one cloud to another. The line in which the plane of vibration intersects the sky can readily be determined, however. This gives the projection of the magnetic field on to a plane perpendicular to the observer's line of sight. A convenient way of representing the observational data in any particular case is to draw a segment of a line with length proportional to the value of P on a map of the sky (cf. 1), the centre of the segment being at the position of the observed star and the direction being that of the projected magnetic field.

When represented in this way, the facts mentioned in the first paragraph show up as segments of maximum length in galactic longitude $l \simeq 102^\circ$, the directions of the segments being nearly parallel to the plane of the Galaxy. If we make the reasonable postulate that the values of a for the interstellar clouds possess no statistical correlation with respect to *heliocentric* galactic longitude, then maximum values of P in $l \simeq 102^\circ$ imply that $\cos \theta \simeq 0$ for this longitude. This would be the case if the solar system lies close to or within a spiral arm in which the magnetic lines of force are everywhere parallel to direction $l \simeq 12^\circ$.

The situation described in the previous paragraphs constitutes the main evidence for the frequently quoted view that magnetic lines of force within a spiral arm run everywhere parallel to the arm. It will be the object of this paper to examine how far such a view is really a necessary inference from the data. It will be shown that the inference is not necessary. Indeed it leads to an immediate and serious difficulty.

2. *A difficulty in the usual model of the spiral arm magnetic field.*—If the magnetic lines of force are parallel to the spiral arm and if they are directed toward $l \simeq 12^\circ$, then the spiral arm must itself be directed toward $l \simeq 12^\circ$. This differs by some forty degrees from the direction indicated by 21 cm hydrogen line-data, which suggests that the arm must be directed toward $l \simeq 54^\circ$.

In an attempt to evade this difficulty it has been argued that the directivity toward $l \simeq 12^\circ$ represents simply a local deflection of the arm, and that the 21 cm data refers to a larger scale directivity. The polarization data itself allows this

suggestion to be put to test. The test does not support the notion of a local deflection.

Remembering that the solar system lies on the inside of the Orion arm, the idea of local deflection would require directions such as $l = 50^\circ$ to pass immediately through the arm. Polarization of somewhat more than half the amount at $l = 102^\circ$ would thus be expected at $l \approx 50^\circ$, the direction of polarization being still just as parallel to the plane of the Galaxy as it is at $l = 102^\circ$. But if, on the other hand, the arm is directed toward $l = 54^\circ$, a direction such as $l = 50^\circ$ would pass into an interarm region, in which case the regular behaviour of the polarizations might be expected to disappear. Reference to the data for regions of the sky within 5° of the galactic plane (1) shows that parallelism to the galactic plane disappears abruptly at longitudes less than about 54° , just as would be expected on the basis of the 21 cm evidence. It is difficult to see how the idea of a local deflection can be maintained in view of this apparently decisive test.

It seems then as if either the usual model of the magnetic field parallel to the spiral arm or the Davis-Greenstein theory must be abandoned. Of these, the first alternative is much to be preferred, especially since quite independent considerations cast doubt on the usual model. In a previous paper (2) it was suggested that the magnetic field of the spiral arm has a helically twisted structure. By adopting such a picture several difficulties were avoided, particularly the difficulty of preserving the arms as coherent structures. On the usual model of a simple cylindrical magnetic field the arms are easily disrupted by the tidal action of the gravitational field of the Galaxy. Disruption is effectively resisted by a sufficiently tightly wound helical structure.

The immediate question arises concerning a helical magnetic model, as to whether such a model is at all consistent with the polarization data, and in particular whether the difficulty discussed above can be resolved by a helical model. This question will be examined in the remaining sections of the paper.

3. *An extreme helical model.*—The case of lines of force wound in tight helices will be treated. Such a case is evidently the extreme opposite to the simple cylindrical picture. At first sight one would expect such a radical change of model to lead to grave discordance with the polarization data. That this does not turn out to be so demonstrates very clearly the incorrectness of the often quoted notion that the polarization data supports the cylindrical picture. Indeed the extreme helical model appears to fit the data better than the cylindrical model.

Before proceeding, it may be useful to remark that the field of the arms becomes twisted if there is a steady drift of material outwards from the nucleus of the Galaxy and if the field is highly twisted by rapid rotation in the nucleus. This was the picture arrived at in the earlier paper (2).

It is worth emphasizing that the degree of twisting of the spiral arm field could hardly be sufficient to lead to the extreme helical model treated here if the velocity curve given in a previous communication (3) was adopted. For this velocity curve, of the order of ~ 10 – 100 twists would be distributed over a spiral arm of length ~ 30 kpc and this would give rise to a loosely wound helical structure. An extreme helical model is suggested by the velocity curve of (4) where the number of twists is much larger. Preliminary results of the Dutch astronomers have confirmed the general shape of the velocity curve of (4); however the rotational velocity at the inner nuclear peak may be even higher than the value of 200 km sec^{-1} given in (4). The number of twists in this case would be closer

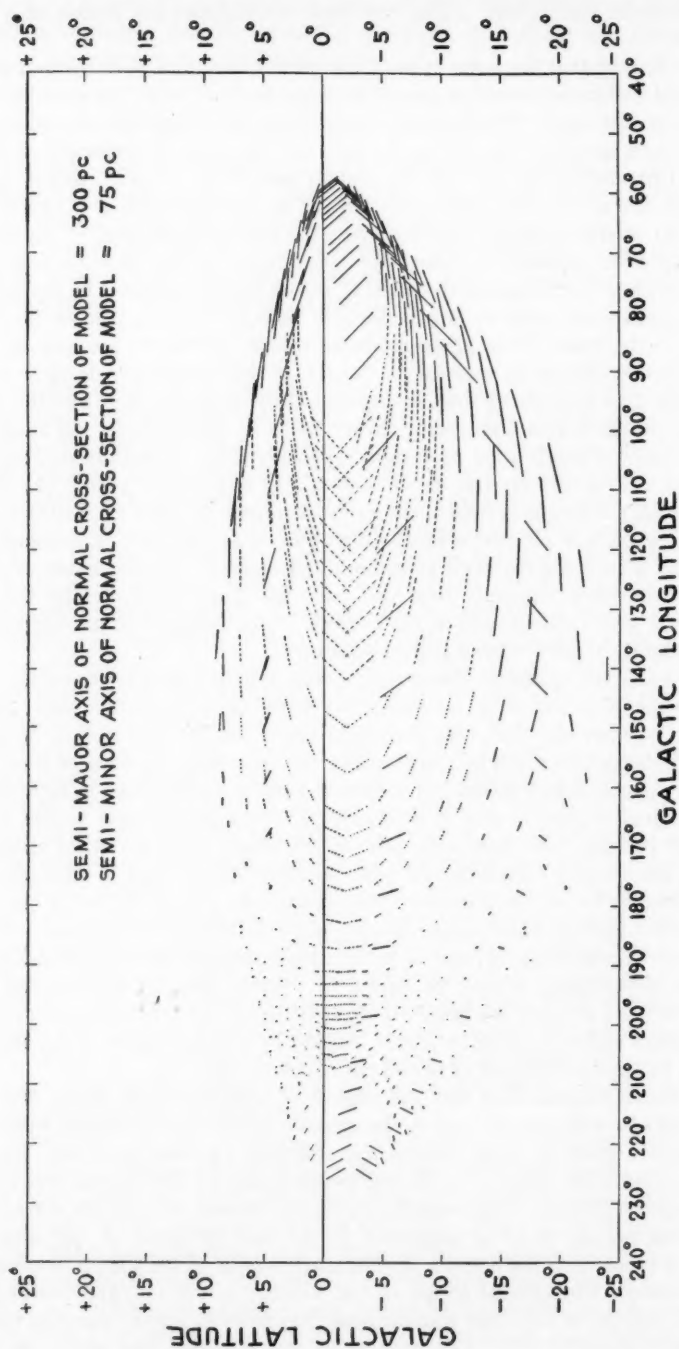


FIG. 1

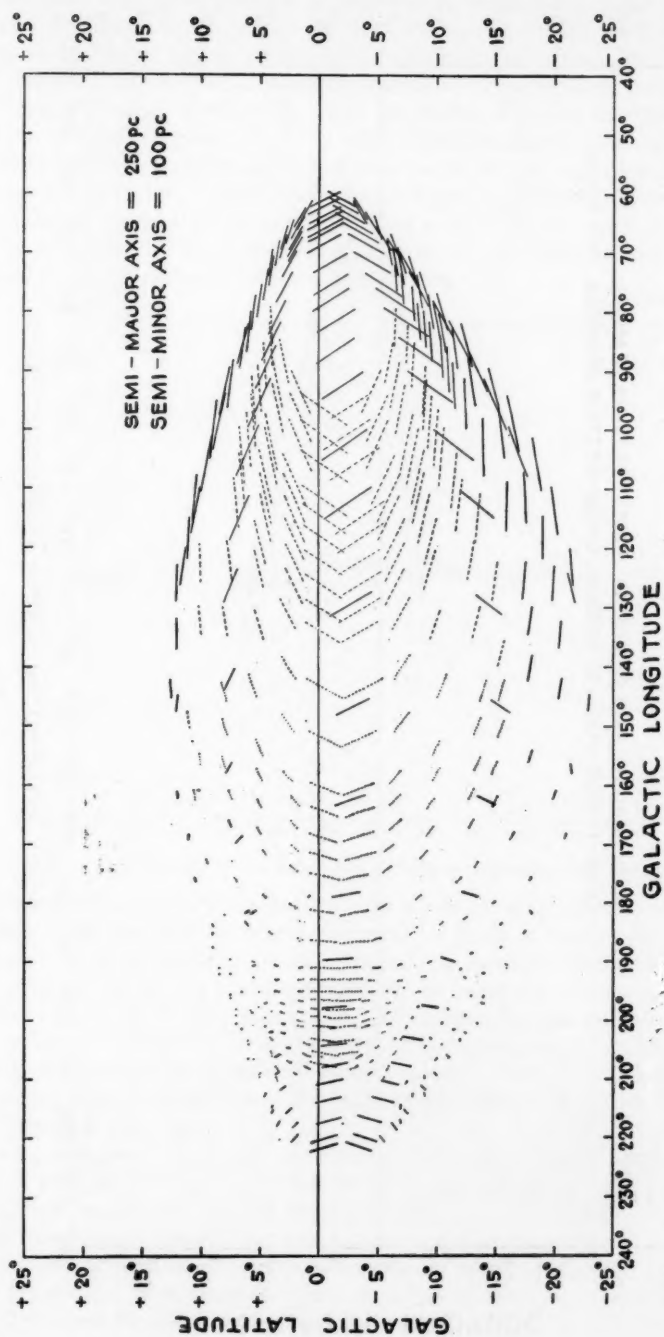


FIG. 2

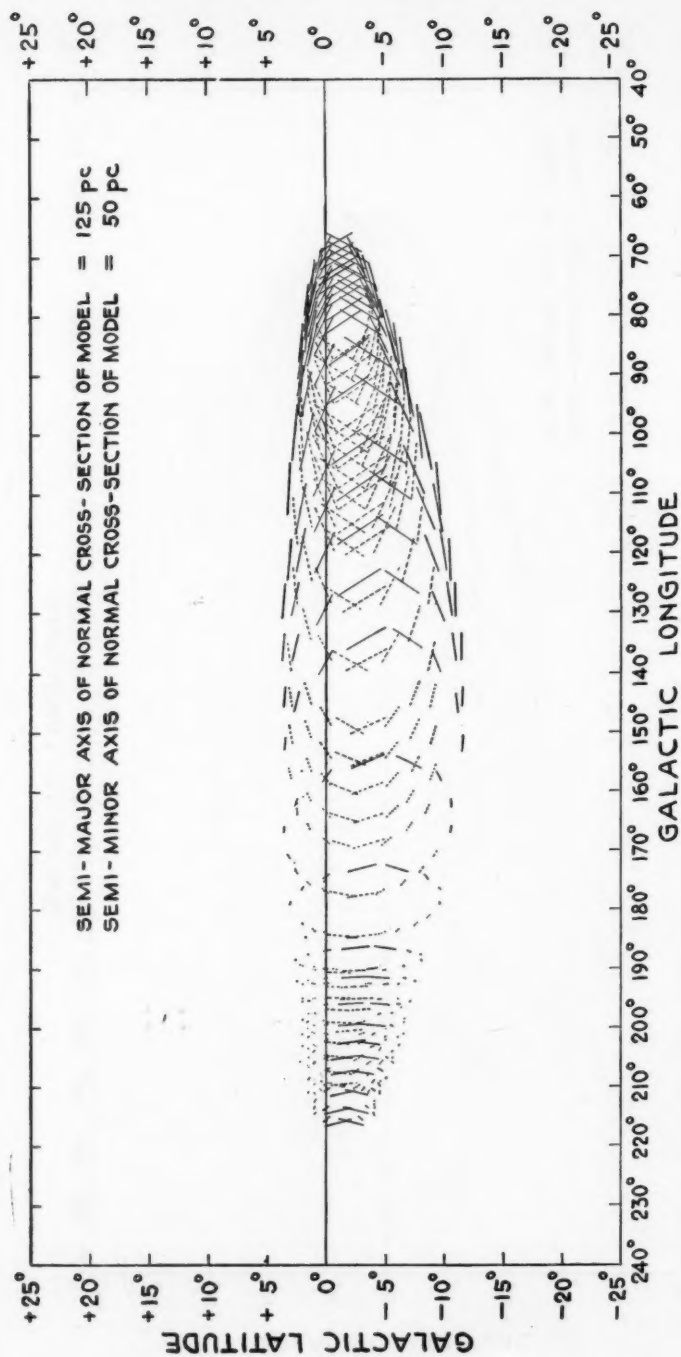


FIG. 3

to 1,000 than 100. This point is of importance, since it is evident that a pronounced difference in the pattern of the polarization would result between a loosely wound and a tightly wound helical model for the spiral arms.

If the arms had circular cross-section, the lines of force would be expected to have circular turns. Because the arms are flattened in the direction perpendicular to the galactic plane, the turns will be correspondingly flattened, however. The turns will here be taken as ellipses with major axes in the galactic plane, and with centres lying on a straight line directed toward galactic longitude $l = 54^\circ$. Since this line forms the axis of the arm, the present model agrees at the outset with the 21 cm data. No serious discrepancy of the sort described in the previous section for the cylindrical model therefore arises.

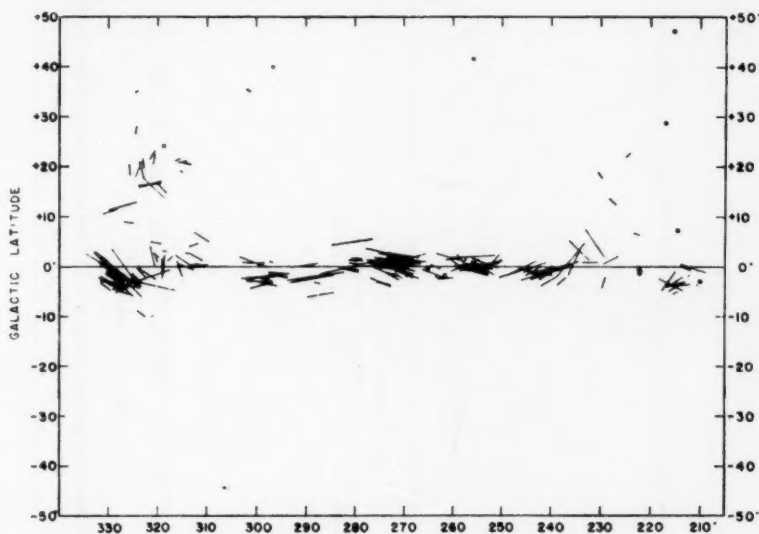


FIG. 4.—Polarization of all stars observed between longitudes 210° and 330° .

The crucial feature of the present model is that the elliptical turns of the field are taken to lie essentially in planes that make an angle of $\sim 40^\circ$ with the axis of the arm. Thus the direction $l = 12^\circ$ is essentially parallel to the turns. Such a feature makes good sense, because the gas on the inner side of an arm must tend to rotate around the Galaxy in a shorter period than the gas on the outer side. This tendency is resisted however by the helical magnetic structure *but only after the turns have become distorted in the present manner*. That such a distortion can prevent any relative streaming of the gas between inside and outside was shown in the previous paper (2).

The polarization produced by discrete interstellar clouds located on the elliptical turns have been worked out for three separate cases:

- (1) Semi-major axis 300 parsecs, semi-minor axis 75 parsecs.
- (2) Semi-major axis 250 parsecs, semi-minor axis 100 parsecs.
- (3) Semi-major axis 125 parsecs, semi-minor axis 50 parsecs.

Cases (1) and (2) were chosen to show the effect of changing ellipticity, and (2) and (3) to show the effect of varying scale within the arm. In each case the solar

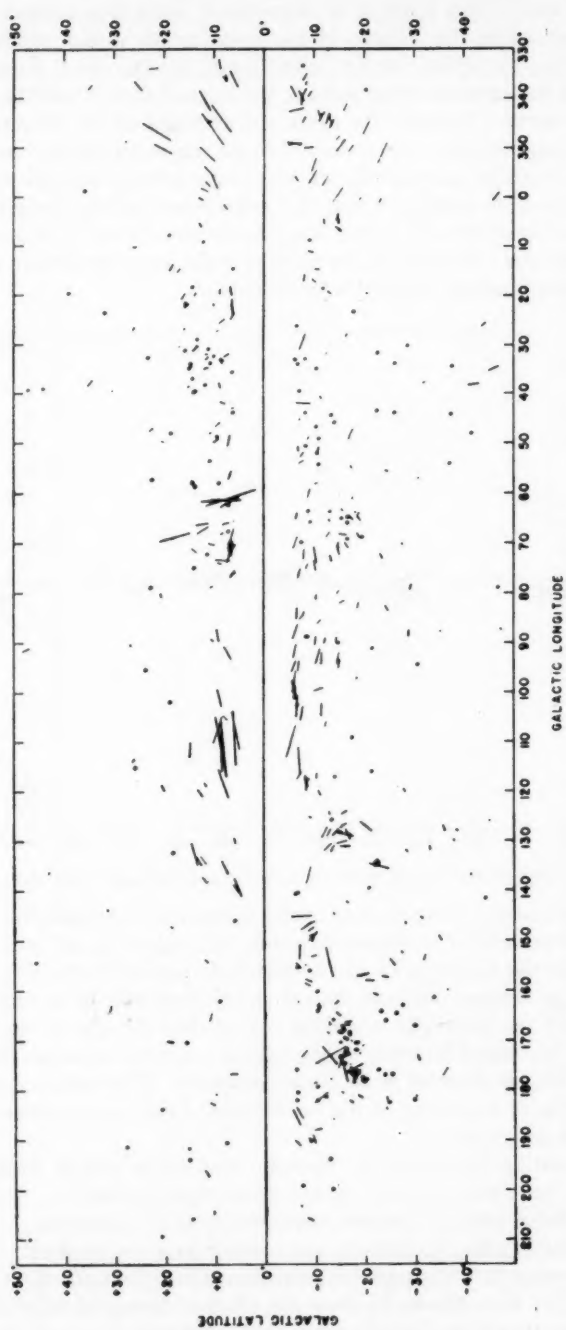


FIG. 5.—Polarization of stars within the longitude interval 330° – 210° and more than 6° from the galactic plane.

system was taken to lie at a distance of 400 parsecs from the axis of the arm, and at a height of 25 parsecs above the galactic plane (i.e. north of the plane). The latter value is believed to be correct to within about 5 parsecs, a circumstance of importance since the results are somewhat sensitive to height above the plane. The results are much less sensitive to distance from the axis.

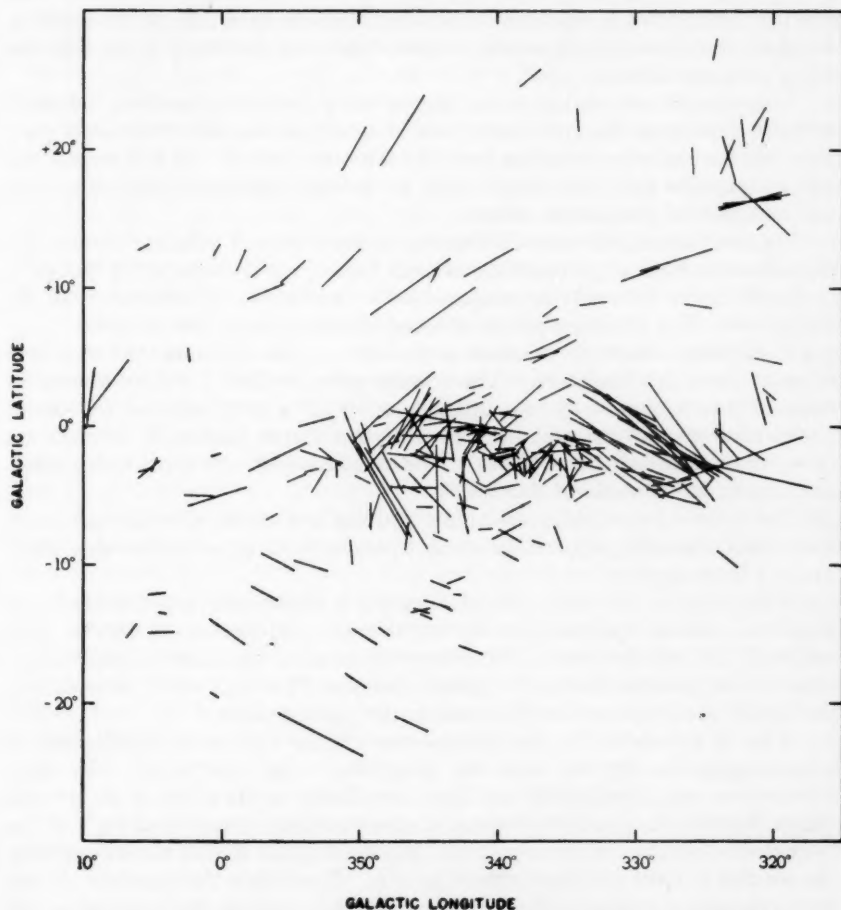


FIG. 6.—Polarization of all stars observed between longitudes 320° and 10° .

Calculations have been made for a wide variety of points on ellipses in different directions. Selecting a particular ellipse the points chosen were spaced at angular intervals of $\sim 20^\circ$ around it. In each case about ~ 30 ellipses were taken, whose centres were spaced at equal intervals of distance 50 parsecs measured from the plane containing the Sun and perpendicular to the arm. These were taken out to a distance of $\sim 1,000$ parsecs in both directions along the arm—i.e. toward $l = 54^\circ$ and $l = 234^\circ$. The important assumption was made that the field within the clouds always possessed the local directivity of the helical field—that

is to say, was directed essentially along the tangent to the particular ellipse under consideration. The effect of this assumption will be discussed in the following section.

The calculations determine the direction of projection of the magnetic field on a plane perpendicular to the line of sight—i.e. on the sky—and also of the value of $1 - \cos \theta$. Results are plotted in Figs. 1, 2, 3 for the respective cases. The effect of each cloud is represented as a segment, the direction of the segment being the direction of the projected magnetic field and the length of the segment being proportional to $1 - \cos \theta$.

Distances are not marked in the figures, but a distinction has been indicated between a cloud on the inner (near) side of an ellipse and one on the outer (far) side—the former are continuous lines, the latter are dotted. In this respect the figures resemble the observational data, no precise distances being determined for the observed polarization effects.

For comparison, the essential features of the observed polarization data are reproduced in Figs. 4, 5, 6 (corresponding to Figs. 1, 2, 3 of the paper by Hall (1)).

4. *Discussion of results as compared with observations of polarization in the Orion arm.*—The following points of broad agreement may first be noted:

(1) Polarization effects are confined to $l > \sim 60^\circ$. The effects of the Orion arm cease at about this longitude. The mosaics given by Hall (1) show almost no cases of polarization at $l \cong 60^\circ$, although at $l \cong 70^\circ$ a large number are found. Longitudes $< \sim 60^\circ$ correspond to the interarm region (assuming no distances $> \sim 1$ kpc), as already noted above. The calculations do not apply to the interarm region (see remarks of Section 6).

(2) For $\sim 70^\circ < l < \sim 130^\circ$, polarization is strong, and statistically there are many more cases where the polarization is nearly parallel to the galactic plane than there are at a large angle.

(3) For $\sim 170^\circ < l < \sim 220^\circ$, the polarization is statistically much weaker, and there is a marked tendency for the few stronger polarizations to turn at right angles to the galactic plane. The observations show few cases of polarization close to the galactic plane. At galactic latitudes $|b| > \sim 5^\circ$, some polarizations are found, many indeed nearly normal to the galactic plane.

What is not shown by the observations are the criss-cross polarizations at steep angles for $b \cong -2^\circ$ and for longitudes $\sim 90^\circ < l < \sim 140^\circ$. In part, obscuration may have limited the data immediately to the south of the galactic plane, for there is a notable absence of observed cases precisely at $b \cong -2^\circ$ for $\sim 105^\circ < l < \sim 140^\circ$. A perhaps more important point is that clouds probably do not stay at fixed positions within the arm. Very likely they oscillate up and down through the galactic plane. It is plausible to suppose that the field within a cloud stays more or less fixed within it as the oscillation proceeds, the direction of the field not agreeing with the local field at any particular moment *but with the field at the place where the cloud happened to be first formed*. Thus the calculations refer more to the initial situations at the moment of formation of clouds than to the ensuing state of affairs. It is easy to see that the general effect of the ensuing oscillation is simply to produce a mixing of polarizations with respect to galactic latitude, but not significantly with respect to galactic longitude. The mixing has the effect that clouds forming appreciably above and below the plane will sometimes be found near the plane. These clouds produce polarizations essentially parallel to the plane for $\sim 70^\circ < l < \sim 140^\circ$. Indeed a general mixing

of polarizations from high latitudes with those at $b = \sim -2^\circ$ immediately destroys the dominance of the criss-cross effect at steep angles referred to above.

It can be argued, however, that essentially no criss-cross effect at all is found in the observed polarizations for $\sim 90^\circ < l < \sim 105^\circ$, and that according to the present model *some* should be found, even though their comparative frequency is weakened by the cloud motions. This criticism is certainly valid on the present picture unless all the polarizations observed in this special region owe their origin to clouds formed appreciably away from the galactic plane. Perhaps over this particular longitude range and over the time interval of relevance, no clouds happen to have formed near the plane.

Another possibility is that the polarization is not so much produced in discrete clouds as in a general medium distributed along the line of sight. This would yield an averaging effect, diminishing steep angles to the galactic plane. The disadvantage of any such averaging is that it makes it more difficult to understand the marked variations in the direction of polarization often found for stars that are very close together on the sky. An attractive feature of the present model is that it yields variations of the sort that are actually found in many directions.

5. *Polarizations toward the galactic centre.*—The effect of the solar system being on the outside of an arm would be to turn the figures through 180° for an inner arm, if the position of the solar system with respect to the arm were the same, and if the arms were not curved. The latter effect in particular must tend to squeeze the whole polarization pattern into a somewhat smaller range of longitude for an inner arm than for an outer arm. Nevertheless it is to be expected that the arm immediately interior to the solar system should produce a generally similar polarization effect but turned through an angle of the general order of 180° . Strong polarization directed predominantly toward the galactic plane should thus be found near $l \cong 280^\circ$, and this in fact appears to be the case.

A new effect arises toward the galactic centre, however. In directions near 327° several arms may produce polarization of distant stars. The pattern of polarization from $\sim 320^\circ$ to $\sim 350^\circ$ is especially interesting (see Fig. 6) in that it does show a strong criss-cross effect at steep angles to the galactic plane. This effect, worryingly absent in the Orion arm, is indeed most strikingly displayed toward the galactic centre. Without some form of twisted field it seems impossible to explain such an effect. This is a further feature in marked contradiction to the simple cylindrical model of the magnetic field.

6. *Polarizations in interarm regions.*—The sudden change in the polarization pattern at $l < \sim 60^\circ$ has already been remarked on. Polarizations become small and fairly randomly distributed. With the axis of the arm directed in $l = 54^\circ$, this is precisely to be expected—the interarm region is encountered for stars at distances $< \sim 1$ kpc at a slightly greater angle than $l = 54^\circ$, simply because the solar system is offset some 400 parsecs from the axis of the arm.

For the same reason in the opposite direction we pass into the interarm region at an angle somewhat less than 234° , say $l < \sim 230^\circ$. Hence we expect the polarizations to change markedly also at about $l = 230^\circ$, and this in fact is exactly the case. Once again the polarizations become smaller and randomly distributed (cf. Fig. 4).

A further highly interesting point is that both at $l \cong 60^\circ$ and at $l \cong 230^\circ$ polarizations are found in high galactic latitudes up to $|b| \cong 30^\circ$. This would be entirely consistent with the idea developed in the previous paper (2) that the lines

of force of the halo field cross through the galactic plane in the interarm regions. It seems that the effect of the halo field looping down around the arm can be decisively seen at $l \simeq 65^\circ$ and again at $l \simeq 235^\circ$. A field at high galactic latitudes can also be seen toward the galactic centre, as would be expected if the halo field also loops around the inner arms.

7. *General conclusions.*—The assumption of a highly twisted spiral arm field is generally consistent with the polarization data, although over a limited range of longitude from about 90° to 110° the almost complete absence of any cases where the direction of polarization is inclined at a steep angle to the galactic plane raises an important difficulty. This could be due to the simple and rather extreme nature of the model, or it could be due to the particular circumstance that all nearby clouds in these directions happened to have condensed at appreciable distances from the galactic plane.

The polarization picture would be essentially different for a spiral arm field with a low number of twists—such as would result from the velocity curve of (3). Such a picture would clearly display the very loose helical structure of the model, and conflict with the optical data.

There is strong evidence that at $l < \sim 60^\circ$ and $l > \sim 230^\circ$ the line of sight passes into interarm regions.

The strong criss-crossing of the polarizations toward the galactic centre supports a twisted model for the spiral arm field, and contradicts the cylindrical model, as does the interarm situation.

There is evidence that a field descends from high galactic latitudes through the interarm regions. This could well be the halo field crossing the galactic plane. There is similar evidence in directions toward the galactic centre.

Acknowledgments.—I wish to express my gratitude to Professor F. Hoyle for his encouragement of the present work, and also to the staff of the Cambridge Mathematical Laboratory for providing computing facilities on EDSAC 2.

Emmanuel College,
Cambridge:
1960 December.

References

- (1) Hall, J. S., *Publ. U.S. Naval Obs.*, **17**, 275, 1958.
- (2) Hoyle, F. and Ireland, J. G., *M.N.*, **122**, 35, 1961.
- (3) Hoyle, F. and Ireland, J. G., *M.N.*, **120**, 173, 1960.
- (4) Hoyle, F. and Ireland, J. G., *M.N.*, **121**, 253, 1960.

A NOTE ON EQUATORIAL ACCELERATION IN A MAGNETIC STAR

L. Mestel

(Received 1961 February 8)

Summary

A rotating star has initially a purely poloidal magnetic field. Meridional circulation of matter causes non-uniform rotation, which in turn generates a toroidal component of field and so a toroidal magnetic force. The possible steady states are studied; it is shown that if the circulation speed is less than the local Alfvén speed (defined by the poloidal field), then flow along a field line parallel to the surface will cause a steady increase of angular velocity towards the equator.

Consider a rotating star, with a poloidal magnetic field symmetrical about the axis of rotation. In a steady state, without meridional circulation of matter, the angular velocity is very nearly uniform along a line of force (\mathbf{r}). Now let there be a maintained meridional circulation of matter. The convection of angular momentum causes a strong variation of angular velocity along a line of force, and so generates a toroidal field. The resulting toroidal force changes the angular momentum of circulating elements. Further, the change in the toroidal field at any point depends not only on the non-uniform rotation along the poloidal field, but also on the convection of the toroidal field by the circulation. We now suppose that a steady state has been reached, and look for the distribution of angular velocity and toroidal field strength.

We write the magnetic and velocity fields

$$\mathbf{H} = \mathbf{H}_p + \mathbf{H}_t, \quad (1)$$

$$\mathbf{v} = \mathbf{v}_p + \mathbf{v}_t = \mathbf{v}_p + \bar{\omega} \Omega \mathbf{t}, \quad (2)$$

where the suffices p and t refer respectively to poloidal and toroidal components, the unit vector \mathbf{t} is in the positive toroidal direction, Ω is the angular velocity, and $\bar{\omega}$ is the perpendicular distance from the axis. In the present note we assume the gas to be a simple perfect conductor, so that in a steady state

$$\nabla_{\Lambda}(\mathbf{v}_{\Lambda} \mathbf{H}) = \nabla_{\Lambda}[(\mathbf{v}_p + \mathbf{v}_t)_{\Lambda}(\mathbf{H}_p + \mathbf{H}_t)] = 0. \quad (3)$$

Thus

$$\nabla_{\Lambda}(\mathbf{v}_{p\Lambda} \mathbf{H}_p) = 0, \quad (4)$$

$$\nabla_{\Lambda}(\mathbf{v}_{t\Lambda} \mathbf{H}_p + \mathbf{v}_{p\Lambda} \mathbf{H}_t) = 0, \quad (5)$$

separating out poloidal and toroidal components respectively. As the system is axially symmetric, the toroidal vector $\mathbf{v}_{p\Lambda} \mathbf{H}_p$ cannot be the gradient of the (single-valued) electrostatic potential; hence from (4)

$$\mathbf{v}_p = \kappa \mathbf{H}_p, \quad (6)$$

where κ is a scalar. Introducing cylindrical polar coordinates $(\bar{\omega}, \phi, z)$, with origin at the centre of the star, and the rotation axis as z -axis, we have from (2),

(5) and (6)

$$\begin{aligned} & \frac{\partial}{\partial \bar{\omega}} (\bar{\omega} \Omega H_{\omega} - \kappa H_{\omega} H_{\phi}) - \frac{\partial}{\partial z} (\kappa H_z H_{\phi} - \bar{\omega} \Omega H_z) \\ &= \left(\Omega - \frac{\kappa H_{\phi}}{\bar{\omega}} \right) \left[\frac{\partial}{\partial \bar{\omega}} (\bar{\omega} H_{\omega}) + \frac{\partial}{\partial z} (\bar{\omega} H_z) \right] \\ & \quad + \bar{\omega} \left(H_{\omega} \frac{\partial}{\partial \bar{\omega}} + H_z \frac{\partial}{\partial z} \right) \left(\Omega - \frac{\kappa H_{\phi}}{\bar{\omega}} \right) = 0. \end{aligned} \quad (7)$$

As

$$\nabla \cdot \mathbf{H} = \frac{1}{\bar{\omega}} \left[\frac{\partial}{\partial \bar{\omega}} (\bar{\omega} H_{\omega}) + \frac{\partial}{\partial z} (\bar{\omega} H_z) \right] = 0, \quad (8)$$

(7) reduces to

$$\mathbf{H} \cdot \nabla \left(\Omega - \frac{\kappa H_{\phi}}{\bar{\omega}} \right) = 0,$$

so that

$$\Omega - \frac{\kappa H_{\phi}}{\bar{\omega}} = \alpha, \quad (9)$$

where α is constant on a particular field line. When $\kappa = 0$ (no motion), (9) reduces to Ferraro's law $\Omega = \alpha$.

From the equation of continuity

$$\nabla \cdot (\rho \mathbf{v}) = \nabla \cdot (\rho \kappa \mathbf{H}) = \mathbf{H} \cdot \nabla (\rho \kappa) = 0, \quad (10)$$

or

$$\rho \kappa = \eta, \quad (11)$$

η being constant on a field line. The toroidal equation of motion can be written

$$\bar{\omega} \left[\frac{(\nabla_{\perp} \mathbf{H})_{\phi} \mathbf{H}}{4\pi} \right]_t = \rho \mathbf{v} \cdot \nabla (\Omega \bar{\omega}^2); \quad (12)$$

the couple exerted by the magnetic force on unit volume is balanced by the rate at which angular momentum is transported out of this volume by the circulation. H_{ϕ} could be zero only if $\Omega \bar{\omega}^2$ were constant on a field line, and then (9) would be violated. With

$$(\nabla_{\perp} \mathbf{H})_{\omega} = -\frac{1}{\bar{\omega}} \frac{\partial}{\partial z} (\bar{\omega} H_{\phi}), \quad (13)$$

$$(\nabla_{\perp} \mathbf{H})_z = \frac{1}{\bar{\omega}} \frac{\partial}{\partial \bar{\omega}} (\bar{\omega} H_{\phi}), \quad (14)$$

(12) becomes, with the help of (11)

$$\frac{1}{4\pi} \left[H_{\omega} \frac{\partial}{\partial \bar{\omega}} + H_z \frac{\partial}{\partial z} \right] (\bar{\omega} H_{\phi}) - \rho \kappa \mathbf{H} \cdot \nabla (\Omega \bar{\omega}^2) = \mathbf{H} \cdot \nabla \left[\frac{\bar{\omega} H_{\phi}}{4\pi} - \rho \kappa \Omega \bar{\omega}^2 \right] = 0; \quad (15)$$

or

$$-\frac{\bar{\omega} H_{\phi}}{4\pi} + \rho \kappa \Omega \bar{\omega}^2 = -\frac{\beta}{4\pi}, \quad (16)$$

where again β is constant on a field line.

Equation (16) is easily interpreted. The flow of matter parallel to the poloidal field transports angular momentum

$$\rho v_p \Omega \bar{\omega}^2 A = (\rho \kappa \Omega \bar{\omega}^2) H_p A \quad (17)$$

per second along a poloidal flux tube of infinitesimal area A . This quantity

is not constant along the flux tube, but a steady distribution of angular momentum is maintained through the transport by the magnetic stresses of angular momentum

$$\left(-\frac{\bar{\omega}H_\phi}{4\pi}\right)H_pA, \quad (18)$$

as shown by Lüst and Schlüter (2). As (H_pA) is constant along a flux-tube, we arrive at (16).

Combining (9), (11) and (16), we find

$$\Omega\left(1 - \frac{4\pi\eta^2}{\rho}\right) = \left(\alpha + \frac{\eta}{\rho\bar{\omega}^2}\beta\right), \quad (19)$$

$$\bar{\omega}H_\phi\left(1 - \frac{4\pi\eta^2}{\rho}\right) = (\beta + 4\pi\eta\alpha\bar{\omega}^2). \quad (20)$$

Equations equivalent to (9), (11) and (16) have been given by Chandrasekhar (3).

To determine the variation of Ω along a field line, we need a relation between α and β . This is given by the condition that the closed loops of the initial poloidal field remain closed loops under the toroidal distortion that generates H_ϕ . The field lines are given by

$$\frac{d\bar{\omega}}{H_\phi} = \frac{\bar{\omega}d\phi}{H_\phi} = \frac{dz}{H_z}. \quad (21)$$

Integrating round a loop, we have by (20)

$$0 = \oint d\phi = \oint \frac{dz}{H_z} \left(\frac{H_\phi}{\bar{\omega}}\right) = \oint \frac{dz}{\bar{\omega}^2 H_z} \frac{(\beta + 4\pi\eta\alpha\bar{\omega}^2)}{(1 - 4\pi\eta^2/\rho)}. \quad (22)$$

This fixes β/α in terms of η , ρ and H_p . If $\eta = 0$, $\beta = 0$ —no motion, no toroidal field.

Suppose first that $4\pi\eta^2/\rho = v_p^2/(H_p^2/4\pi\rho) < 1$ over the whole of a loop—i.e. the flow speed is everywhere less than the local speed of hydromagnetic waves along the poloidal field. Then as $dz/H_z > 0$, (22) implies that

$$\beta + 4\pi\eta\alpha\bar{\omega}_c^2 = 0, \quad (23)$$

where $\bar{\omega}_c$ is the axial distance of at least two points on the loop (there may be more than two if the equation $z = z(\bar{\omega})$ to the loop is more than doubly-valued). By (20), H_ϕ changes sign at $\bar{\omega} = \bar{\omega}_c$; as it has arisen by toroidal distortion of H_p , clearly H_ϕ cannot have the same sign all the way round a loop. Because of the factor $\bar{\omega}^2$ in the denominator of (23), the points $\bar{\omega}_c$ will be near the axis if the loop considered comes close to the axis.

Substituting (23) into (19), we have

$$\frac{\Omega}{\alpha} = \frac{\left[1 - \frac{4\pi\eta^2}{\rho} \left(\frac{\bar{\omega}_c}{\bar{\omega}}\right)^2\right]}{\left(1 - \frac{4\pi\eta^2}{\rho}\right)}. \quad (24)$$

Consider now a field line which has a segment nearly parallel to the stellar surface, so that ρ is constant along this segment. Then as long as $(4\pi\eta^2/\rho)(\bar{\omega}_c/\bar{\omega})^2 < 1$, (24) predicts that Ω/α is positive, and that it *increases with* $\bar{\omega}$. As $4\pi\eta^2/\rho < 1$, Ω/α is certainly positive for $\bar{\omega} \geq \bar{\omega}_c$; and if $4\pi\eta^2/\rho \ll 1$, we may expect Ω/α positive along the whole of the horizontal segment, as $\bar{\omega}_c$ is likely to be a point near the axis.

If $4\pi\eta^2/\rho > 1$ along a whole loop, we can still define $\bar{\omega}_c$ by (23), but (24) is best written

$$\frac{\Omega}{\alpha} = \frac{\left[\frac{4\pi\eta^2}{\rho} \left(\frac{\bar{\omega}_c}{\bar{\omega}} \right)^2 - 1 \right]}{\left(\frac{4\pi\eta^2}{\rho} - 1 \right)}. \quad (25)$$

This predicts a decrease in Ω/α along a horizontal segment. $|\Omega|$ decreases along the whole length if $4\pi\eta^2/\rho > (\bar{\omega}_{\max}/\bar{\omega}_c)^2$; otherwise there is a point of zero rotation on this segment, with $|\Omega|$ increasing on either side. When $4\pi\eta^2/\rho \gg 1$, (25) predicts $\Omega\bar{\omega}^2 = \text{constant}$ on a streamline, as expected.

Finally, suppose that $(1 - 4\pi\eta^2/\rho)$ changes sign at two points P_1 and P_2 of a loop (the discussion is unaffected by the restriction to two such points). Then if our steady state is to be meaningful, we must have simultaneously:

$$\beta + 4\pi\eta\alpha\bar{\omega}_c^2 = 0; \quad 4\pi\eta^2/\rho_c = 1; \quad (26)$$

and so also

$$\alpha + \frac{\eta\beta}{\rho_c\bar{\omega}_c^2} = 0, \quad (27)$$

ρ_c being the density at $\bar{\omega}_c$. For if (26) and (27) do not hold, both H_ϕ and Ω have singularities, yielding infinite rotational and magnetic energy densities at $\bar{\omega}_c$. (It is true that an infinite rotational shear is inconsistent with the implicit neglect of viscous forces in (12); but stellar viscosity is so small (4) that a steady state that included viscous forces would still result in local centrifugal and poloidal magnetic forces far larger than the equilibrium of the star could tolerate.)

Equations (26) and (27) imply a density field distorted from the approximately spherical, for at P_1 and P_2 both $\bar{\omega}_c$ and ρ_c would have to be the same. However, we can rule out this case by substituting (26) into (22):

$$\frac{\alpha}{\eta} \oint \frac{dz}{\bar{\omega}^2 H_z} \frac{(\bar{\omega}^2 - \bar{\omega}_c^2)}{\left(\frac{1}{\rho_c} - \frac{1}{\rho} \right)} = 0. \quad (28)$$

Thus as numerator and denominator of the integrand have the same sign, $\alpha = \beta = 0$: a steady state is possible only if the angular momentum in this particular flux-tube is zero. We conclude that in general a steady state is possible only if the circulation is either "sub-Alfvén" or "super-Alfvén" everywhere along a field line.

If l is the perpendicular distance between neighbouring poloidal loops, the angular momentum within the flux-tube defined by these lines is

$$\oint \rho \Omega \bar{\omega}^2 (2\pi \bar{\omega} l ds) = 2\pi\eta (H_p \bar{\omega} l) \alpha \oint \frac{\bar{\omega}^2}{v} \frac{\left[1 - \frac{4\pi\eta^2}{\rho} \left(\frac{\bar{\omega}_c}{\bar{\omega}} \right)^2 \right]}{\left(1 - \frac{4\pi\eta^2}{\rho} \right)} ds, \quad (29)$$

where ds is the scalar element of length. The transition to our steady state from the "initial" state, with no circulation and no toroidal field, involves merely a redistribution of angular momentum along flux-tubes; hence given \mathbf{v} (satisfying (11)) we can by (22) and (29) express α and β in terms of η , \mathbf{H}_p , and the prescribed angular momentum within the flux-tube.

As a rough numerical example, suppose $4\pi\eta^2/\rho \ll 1$; then $|\Delta\Omega/\Omega|$ along a horizontal segment from $\bar{\omega}_1$ to $\bar{\omega}_2$ is, by (24), approximately

$$(4\pi\eta^2/\rho)[(\bar{\omega}_c/\bar{\omega}_1)^2 - (\bar{\omega}_c/\bar{\omega}_2)^2],$$

which is $\approx 4\pi\eta^2/\rho$ if $\bar{\omega}_2 \gg \bar{\omega}_1 \approx \bar{\omega}_c$.

Taking for \mathbf{v} the velocity of migration of the sunspot zone ($\approx 2 \times 10^2$ cm/sec) and for ρ a sub-photospheric value (10^{-7} g/cm³), $|\Delta\Omega/\Omega| \approx 5 \times 10^{-2}/H_p^2$. An equatorial acceleration of 15 per cent requires H_p to be ≈ 0.6 gauss.

Discussion

The prediction of equatorial acceleration is sufficiently remarkable to justify this preliminary note. However, it is clear that many problems remain. We have taken as given a velocity field \mathbf{v}_p that satisfies (6) and (11); in fact, the circulation in non-convective regions is determined by the non-spherical distortion of the thermal field by the centrifugal and magnetic forces (5). Over the bulk of the star the circulation is slow, and will generate only very slight departures from isorotation, and very weak toroidal fields; but near the surface where the density is low the circulation is in general much more rapid (6), and should have important hydromagnetic effects.

If we regard the field \mathbf{H}_p as at our disposal, and exerting negligible poloidal forces, we may compute \mathbf{v}_p in terms of Ω and H_p , and then choose \mathbf{H}_p so as to satisfy (6) and (11), so that steady state conditions are fulfilled. Even so, as by (19) and (20) Ω and H_p depend partly on \mathbf{H}_p , there may still result a difficult self-consistent problem. In a more realistic problem, the initial field \mathbf{H}_p would be arbitrary. It should be noted that the thermally driven circulation is "inexorable", being fixed by the Ω and H_p fields: even with the energy density of the circulation less than that of \mathbf{H}_p , the circulation must cause progressive distortion of \mathbf{H}_p , as long as the reaction back of \mathbf{H}_p on the thermal field can be ignored. For the steady state theory to be relevant, the coinciding streamlines and poloidal field lines must be closed loops within the body of the star. If, for example, the initial field is of roughly dipole type, with field lines entering and leaving the surface, a steady state of circulation will not be reached until the field has been greatly distorted, and the internal and external parts of the field separated by Ohmic diffusion. It is not clear that this will occur before the distorted field \mathbf{H}_p exerts forces strong enough to react back on the thermal field, and so on the circulation, which might even be reduced to zero.

The treatment has been based on a simplified form of "Ohm's law" for a plasma, which neglects the Ohmic, Hall and thermoelectric fields (4). As is well known, by Cowling's theorem an axially symmetric system of finite conductivity cannot be strictly steady; near the O-type neutral points that the field \mathbf{H}_p must possess, the Ohmic term always dominates over the induction term, so that the field must decay. However, for large-scale fields, the decay is slow and we may expect the Ω and H_p fields steadily to adjust themselves to \mathbf{H}_p as it changes. [In a convective region, a Bullard-type dynamo may operate: the inevitable fluctuations about strict axial symmetry may allow the poloidal field to be regenerated from the toroidal (7). Our axially symmetric treatment could then be regarded as a smoothed-out version of the actual non-symmetric processes.]

On taking the curl of Ohm's law, it is found that the neglected terms have very little effect on (9). However, they do affect the flow of current parallel

to H_p , so that (22) is replaced by a new (β, α, η) relation, in a time-scale of the same order as the decay time of H_p . Thus the initial closed loops of field will not remain so. In fact, the condition (22) is a rather special one; the hydro-magnetic and dynamical conditions (9) and (16) can be satisfied, given the velocity field and the angular momentum per flux-tube, by any (β, α, η) relation (provided the star is not given more disruptive energy than it can bear). Thus we could imagine our initial field (before circulation starts) as having both poloidal and toroidal components, but exerting no torque; when the circulation starts, an extra toroidal field is generated, exerting torque. But again the field so built will not satisfy the poloidal component of Ohm's law, and so it will gradually change its structure. Further treatment will be given in a later paper, with special reference to the equatorial acceleration problem, and the amount of energy stored in the rotational and the toroidal magnetic fields. For the moment we just wish to emphasize that equatorial acceleration is not tied to the existence of field lines closed in space. It is condition (23) that yields the acceleration for sub-Alfvén flow, and this by (20) merely requires that H_ϕ should change sign at points distant $\bar{\omega}_c$ from the axis; this will occur in infinitely many fields besides that determined by (22).

Finally, we should note that although in convective zones large-scale meridian circulation is superimposed on the small-scale turbulent motions (8, 9) the immediate application of the results on equatorial acceleration to the solar case is somewhat premature: the existence of the solar cycle clearly indicates that a periodic rather than a steady solution of the equations should be sought. We may conjecture that the strong sub-photospheric toroidal magnetic girdles, which are presumably responsible for sunspots, generate circulation through the disturbance they themselves exert on the thermal field, and are dragged by the circulation. A periodic rather than a steady solution would therefore seem more plausible, but it is not clear that such a solution would yield a constant equatorial acceleration.

Note.—In a private communication, Sir Edward Bullard has commented on the similarity between the work of this paper and that of himself and his collaborators on the westward drift of the Earth's magnetic field (10).

*Department of Applied Mathematics and Theoretical Physics,
Cambridge:
1961 February 7.*

References

- (1) V. C. A. Ferraro, *M.N.*, **97**, 458, 1937.
- (2) R. Lüst and A. Schlüter, *Z. f. Ap.*, **38**, 190, 1955.
- (3) S. Chandrasekhar, *Ap. J.*, **124**, 232, 1956.
- (4) T. G. Cowling, *Solar Electrodynamics in The Sun*, G. P. Kuiper (ed.), Chicago, 1953.
- (5) P. A. Sweet, *M.N.*, **110**, 548, 1950.
- (6) N. Baker and R. Kippenhahn, private communication.
- (7) E. N. Parker, *Ap. J.*, **122**, 293, 1955.
- (8) L. Biermann, I.A.U. Symposium No. 6, 248, 1958.
- (9) R. Kippenhahn, *Modèles d'Etoiles et Evolution Stellaire*, 249, Liège, 1960.
- (10) E. C. Bullard, Cynthia Freedman, H. Gellman and Jo Nixon, *Phil. Trans. A*, No. 859, 1950.

THE RADIO EMISSION FROM NORMAL GALAXIES

II. A STUDY OF 20 SPIRALS AT 158 Mc/s

R. Hanbury Brown and C. Hazard

(Received 1961 March 3)

Summary

A survey has been made of the radio emission at 158 Mc/s from twenty bright spiral galaxies. A radio index R has been defined by the equation $R = m_r - m_{pg}$, where m_r and m_{pg} are the radio and photographic magnitude respectively. The results indicate that R is a function of the inclination and galactic latitude of a galaxy and it is suggested that this effect is due to the absorption of light. The mean value of R for spirals of type Sb and Sc is $+1.3$ with an r.m.s. dispersion ± 0.7 . No significant difference was found between the mean values of R for the two types of galaxy.

1. *Introduction*

A survey of the radio emission from some bright normal* galaxies has been made at 158 Mc/s using the 250 ft steerable paraboloid at Jodrell Bank. The object of this survey was to establish the integrated radio magnitudes of these galaxies, and in particular to investigate how the ratio of the total light to the total radio flux varies among galaxies of the same type and also how it depends upon type. In Part I (1) we described the apparatus used in this survey and reported the results obtained on M31 and M33; the present paper (Part II) contains the results on twenty spiral galaxies of types Sb and Sc. The observations of other types of galaxy will be published in a further paper (Part III) together with a discussion of all the data.

2. *Method of observation*

A description of the apparatus was given in Part I together with the method of observation of M31 and M33. For the remainder of the galaxies the observations were carried out as follows. First, a preliminary survey was made in an effort to detect radio emission from a particular galaxy. In this survey two sets of scans were made through the expected position, one set of scans being made at constant right ascension and the other at constant declination; each scan was repeated several times as a check on its reliability. In some regions these scans sufficed to give the position and intensity of the radio source associated with the galaxy, and an example of such a region is illustrated in Fig. 1 which shows two scans made over NGC 253. In other more confused regions it was found necessary to survey a considerable area around the expected position as an aid to the interpretation of the observations.

* In this context a normal galaxy, following Baade and Minkowski (2), is taken to be a galaxy which appears to be normal when examined photographically.

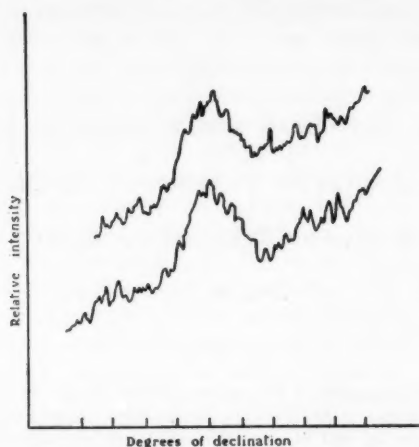


FIG. 1.—Two scans in declination across NGC 253. These scans were both made at a constant right ascension ($00^h 45^m.1$) with a beamwidth of 2° at 158 Mc/s (July, 1958).

Before each set of observations the equipment was calibrated on the source I.A.U. 14N5A and all the magnitudes in the present paper were measured relative to that source. The scale of radio magnitude (m_r) is defined by the equation

$$m_r = -53.45 - 2.5 \log S_{158} \quad (1)$$

where $S_{158} \text{ w. m}^{-2} (\text{c/s})^{-1}$ is the flux density of a source at 158 Mc/s. Following Part I we have taken the magnitude of 14N5A to be +6.86.

3. Results

Observations were made on the twenty galaxies listed in Table I. All these galaxies are brighter than $m_{pg} = 10.6$ on the scale of Holmberg (3) and were in convenient positions to be surveyed during the autumn of 1958 when this work was carried out.

The results are summarized in Table I, which gives the positions and apparent magnitudes of the radio sources; some detailed remarks on the individual galaxies are contained in the notes. In fifteen cases a radio source was found close to the position of the galaxy, and the measurements are sufficiently precise to allow an identification to be made. It is of course possible that some of the suggested identifications represent chance coincidences with discrete sources; but at 158 Mc/s there is about one source per 20 square degrees with an intensity above the limiting sensitivity of the present survey and it is therefore unlikely that more than two of the identifications suggested in Table I represent a chance coincidence. In the remaining five cases the isophotes of the region around the galaxies were too complicated to be interpreted unambiguously and a definite conclusion would require superior resolving power; in four of these cases there was evidence of a radio source close to the position of the galaxy but the position could not be established with satisfactory precision. When no radio source could be identified with a galaxy an upper limit to the radio emission was estimated from the records and this limit is given in Table I.

TABLE I

Radio data at 158 Mc/s

Galaxy	Position of visible nebula (1950)		Position of radio source (1950)		Observed radio magnitude $m_r(b)$	Angular size of visible nebula $a \times b$	Estimated angular size of radio source $a' \times b'$	Integration correction† $\Delta m(\theta, a', b')$	Integrated radio magnitude m_r
	R.A. h m	Dec. °	R.A. h m	Dec. °					
NGC 224(M31)	00 40	+41 00	00 40.3	$\pm 1^m$	+6.99	197' × 92'	246' × 156'	-1.29	+5.70
253*	00 45.1	-25 34	00 44.8	1	8.32	35 × 8	46 × 23	0.10	8.22
598(M33)	01 31.1	+30 24	01 31.8	1	8.43	83 × 53	126 × 84	0.67	7.76
IC 342*	03 41.9	+67 57	03 42	3	7.92	25 × 20	33 × 28	0.08	7.84
2403	07 32.0	+65 43	—	—	—	29 × 15	38 × 22	0.08	>9.0
2683	08 49.6	+33 38	—	—	—	12.1 × 3.9	16 × 9	0.01	>9.3
3031	09 51.5	+69 18	—	—	9.56	35 × 14.4	46 × 27	0.11	9.45
4236	12 14.3	+69 45	—	—	—	26 × 8.7	34 × 19	0.06	>8.6
4244	12 15.0	+38 05	12 16.5	5	9.34	18 × 2.9	23 × 12	0.03	9.31
4258	12 16.5	+47 35	12 16.8	2	9.34	24 × 9.6	31 × 18	0.05	9.29
4490	12 28.3	+41 55	12 29	2.5	9.49	8.9 × 4.7	12 × 7	0.01	9.48
4565	12 33.9	+26 16	12 34.5	1.5	9.80	20 × 3.6	26 × 13	0.04	9.76
4631	12 39.8	+32 49	12 40.5	1.3	9.49	19 × 4.4	25 × 13	0.03	9.46
4736	12 48.6	+41 23	12 45	4	9.49	15 × 13.3	20 × 18	0.03	9.46
4826	12 54.3	+21 47	12 53	2	9.34	12.3 × 8.3	16 × 12	0.02	9.32
5055	13 13.5	+42 17	—	—	—	16.0 × 10.1	21 × 15	0.03	>9.6
5194	13 27.8	+47 27	13 28.3	1.3	9.05	14.2 × 9.5	18 × 14	0.02	9.03
5236*	13 34.3	-29 37	13 35	1	7.86	18 × 18	23 × 23	0.04	7.82
5457	14 01.4	+54 35	14 03	2.5	9.51	28 × 28	36 × 36	0.11	9.40
6946	20 33.9	+59 58	20 32.8	3	9.50	14.4 × 12.6	19 × 17	0.03	9.47

† The estimated angular size of the radio source is the total width between points of half-intensity.

‡ The integration correction is defined by equation (3) in the text.

* Not included in Holmberg's list. † Data from the revision of the *Harvard Survey of Bright Galaxies* by de Vaucouleurs (4).

Notes on Table I

NGC 224. See Part I for a detailed discussion.

NGC 253. The radio source is clearly defined. It has also been reported by Mills (9).

NGC 598. See Part I.

IC 342. Although the radio source lies on a steep gradient in both right ascension and declination it is clearly defined.

NGC 2403. This galaxy lies in a difficult region to interpret. On right ascension scans it lies in a sharp minimum of the background radiation and the radio source cannot be observed distinctly. The records indicate the presence of a source in the correct position. The declination scans are confused by nearby sources.

NGC 2683. Region complicated by nearby sources.

NGC 3031. The source lies in a region of enhanced emission extending about fifteen degrees in both declination and right ascension which contains a number of weak sources. Observations are confused by a weak source about half a degree to the north of the galaxy. This confusing source has been shown by Palmer (6) to have a diameter of about 2 minutes of arc. The source in the position of NGC 3031 appears to have a diameter greater than 40 minutes of arc and it seems reasonable to assume that this source may be identified with NGC 3031. Its intensity has been estimated by subtracting the calculated contribution of the small diameter source from the flux density observed, an allowance being made for the different positions of the sources in the beam; the intensities in each case were measured relative to the source I.A.U. 14N5A in order to avoid errors in calibration.

NGC 4236. This region is complicated by nearby sources.

NGC 4244. Declination scans show a clearly defined radio source close to the position of the galaxy which is situated on the edge of a localized region of enhanced intensity. The right ascension scans were of poor quality and it was not possible to measure an accurate right ascension. The identification is therefore rather uncertain.

NGC 4258. The radio source was well resolved on right ascension scans but the declination scans are too confused to permit the determination of an accurate declination.

NGC 4490. The radio source is well resolved in declination but the measurement of its right ascension is complicated by the region of enhanced intensity in which it lies.

NGC 4565. A well defined source on a moderately steep gradient in right ascension.

NGC 4631. A well defined radio source.

NGC 4736. The radio source is well resolved in declination but in right ascension the records are confused and it was therefore not possible to make accurate measurements of this coordinate. A provisional identification.

NGC 4826. Although near a minimum in the background radiation this is a clearly defined radio source.

NGC 5055. This region is complicated by nearby sources and gradients in background radiation. There appears to be a radio source at the correct declination but it is to the west of the visible nebula. However, the interpretation of the records is subject to considerable uncertainty and there is some evidence that the observed source is a double source, the two components having approximately the same declination but differing in right ascension. One of these components may be due to the galaxy.

NGC 5194. Although the observations are complicated by the position being near the centre of a region of enhanced intensity the radio source is well defined.

NGC 5236. This region is confused by a nearby source and a steep gradient, but the radio source in the position of the visible nebula can be clearly observed.

NGC 5457. This region is complicated by the presence of the intense source 14N5A. In the present survey the radio source associated with the galaxy and 14N5A are well resolved.

NGC 6946. This galaxy lies in a pronounced minimum of the background radiation which accounts for the uncertainty in the measured intensity.

4. The integrated radio magnitude

The radio magnitude $m_r(\theta)$, tabulated in Table I, was calculated from the observed peak deflection. It is therefore a function of the aerial beamwidth θ and the angular size of the source. The integrated radio magnitude m_r , which is also shown in Table I, is a measure of the total flux received from a source and is independent of beamwidth. It is obtained by integrating the flux over the disk of the source, and therefore corresponds to the magnitude which would be observed with a beamwidth large compared with the angular size of the source.

In the case of M31 and M33 the values of m_r were found by integrating the detailed isophotes of the region around each source as discussed in Part I. For the remaining sources in the table, which have a smaller angular size than the beam, the differences between the observed magnitudes $m_r(\theta)$ and the integrated magnitudes m_r are small, and we have calculated these differences by estimating the angular size of the radio sources as follows.

It was shown in Part I that in both M31 and M33 the majority of the radio emission arises in an extensive corona which envelopes the visible nebula and we have assumed that other galaxies of types Sb and Sc possess similar coronae. This assumption is supported by an examination of some records made with an interferometer at 158 Mc/s (6). These records cover the regions around NGC 3031, 4736 and 5194 and were made with baselines of 60 λ and 330 λ . They show that the majority of the radio emission from both NGC 4736 and 5194 arises in a source with a diameter of about 25', while in NGC 3031 the corresponding diameter exceeds 40'. These diameters have been estimated on the assumption that the sources are circular disks with a gaussian radial variation of brightness. Although these results are approximate they indicate that for these three galaxies the ratios of optical to radio diameter are similar to those found for M31 and M33 and they support the assumption that all Sb and Sc galaxies have extensive coronae.

In order to estimate the angular sizes of the sources shown in Table I we have therefore assumed that every galaxy has a corona whose ellipticity and size relative to the visible nebula are similar to those found in M31 and M33. Following the results in Part I we have taken this corona to be ellipsoidal with an axial ratio of 0.5 and have assumed that the principal planes of the corona and the visible nebula coincide; the apparent angular size of the major axis of the corona between half intensity points has been taken as 1.3 times the maximum extent of the visible nebula as measured by Holmberg (3). On these assumptions the angular size of the radio source associated with any particular galaxy can be estimated from the angular size of the visible nebula. The major axis is simply proportional to the maximum extent of the nebula as stated in the previous paragraph, while the minor axis can be calculated from the inclination. The inclination may be calculated to a sufficient degree of accuracy on the assumption that the visible nebula is also spheroidal, from the equation

$$\sin^2 i = \frac{(b/a)^2 - p^2}{1 - p^2} \quad (2)$$

where i is the angle of inclination of the principal plane of the visible nebula to the line of sight, p is the axial ratio of the spheroid and b/a is the axial ratio of the nebula image. We have calculated the inclination of all the spirals in Table I assuming $p = 0.2$ (3); in cases where $(b/a) < 0.2$ we have taken the inclination to be zero. These values of inclination have been used to estimate the apparent

angular dimensions $a' \times b'$ of the radio sources, again by means of equation (2), taking $p = 0.5$ which is the value appropriate to the coronae.

The estimated angular dimensions of each radio source have been used to calculate the integration correction $\Delta m(\theta, b', a')$ which was applied to the observed magnitude $m_r(\theta)$ to find the integrated magnitude m_r . It was assumed in this calculation that the distribution of intensity across the elliptical disk of a radio source follows a gaussian variation along both axes, and that the aerial beam is circularly symmetrical with a gaussian profile. On these assumptions it is simple to show that

$$\Delta m(\theta, b', a') = m_r - m_r(\theta) = -2.5 \log [(1+s^2)(1+s^2r^2)]^{1/2} \quad (3)$$

where s is the ratio of the width of the major axis of the radio source to the width of the beam, and r is the apparent axial ratio (b'/a') of the radio source.

The calculated values of $\Delta m(\theta, a', b')$ are given in Table I together with the corresponding integrated magnitudes m_r ; for M31 and M33 the integrated magnitudes are those measured directly from the isophotes (see Part I). The table shows that, with the exception of these two galaxies, the integration corrections are small and in most cases less than the probable errors in measurement. It is therefore unlikely that the values of m_r are significantly in error due to the finite angular size of the radio sources, serious errors could only be introduced if the ratio of the size of the corona to the visible nebula is much greater in some of the galaxies than in M31 and M33.

5. Comparison of the radio and photographic magnitudes

5.1. *Introductory remarks.*—Since we are concerned in the present work to establish the ratio of the *total* light to the *total* radio flux emitted by a galaxy it is convenient to define a measure of this ratio. By analogy with the concept of colour index we propose to define the *radio index* R of a galaxy as the difference between the integrated radio and photographic magnitudes. Thus

$$R = m_r - m_{pg} \quad (4)$$

where m_r and m_{pg} are the radio and photographic magnitudes respectively.

It is clear that the value of R , as observed for any particular galaxy, will depend upon the absorption of light and also of radio waves. In an effort to arrive at values of R which can be usefully compared, we have therefore corrected the observed results for the effects of absorption. We have assumed, following an earlier analysis (7), that for all directions of observation the radio absorption both in our Galaxy and in external galaxies is negligibly small, and we have also assumed that the radio emission from a galaxy is isotropic in direction. On the other hand the absorption of light cannot be neglected and may take place both in our Galaxy and in the galaxy under observation; these two cases will be considered in turn.

5.2. The effect of the internal absorption of light in a galaxy on the radio index.—

The internal absorption of light in a spiral is mainly due to obscuring clouds concentrated in the plane of the galaxy and will therefore depend on its orientation with respect to the observer. This effect will cause the observed radio index to depend on the orientation of the galaxy, and hence there should be a correlation between the measured values of R and the apparent axial ratio b/a of the photographic image; if the radio absorption is negligible, as assumed above, then spirals seen edge-on should exhibit low values of R . We have analysed our results to test for this effect as follows.

First, we have restricted our analysis to galaxies in Holmberg's catalogue so that measurements of m_{pg} shall be homogeneous. Secondly, in order to avoid confusion with the effects of absorption in the Galaxy, we have further restricted the analysis to those galaxies which are more than 40° from the galactic plane; this excludes M31 and M33 and has the advantage that for all the galaxies included in the analysis the integration corrections are small and are therefore less likely to introduce error into the following discussion.

The ten galaxies which fulfil the necessary criteria are shown in Table II, and in Fig. 2 the radio index for these galaxies is plotted against the apparent axial ratio b/a of the associated visible nebulae. Although the scatter of the results in Fig. 2 is large, they indicate that the radio index decreases with b/a and hence depends upon the inclination of the visible nebula.

TABLE II

The effect of the internal absorption of light on the radio index of a spiral galaxy

Galaxy	Type (after Holmberg)	b/a	$R(i, \beta)$
NGC			
4244	Sc+	0.16	-1.2
4565	Sb+	0.18	-0.5
4631	Sc+	0.23	-0.3
4258	Sb+	0.40	+0.4
3031	Sb-	0.41	+1.6
4490	Sc+	0.53	-0.6
5194	Sc-	0.67	+0.2
4826	Sb-	0.67	+0.1
4736	Sb-	0.90	+0.6
5457	Sc-	1.00	+1.2

b/a is the apparent axial ratio of the visible nebula; $R(i, \beta)$ is the radio index ($m_r - m_{pg}$), where i and β represent the inclination and galactic latitude of the galaxy respectively.

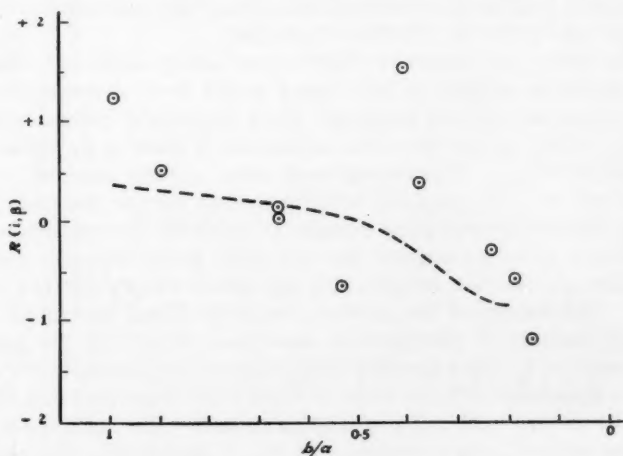


FIG. 2.—The relation between the inclination of a spiral and the radio index.

Ordinate: The radio index $R(i, \beta)$.

Abscissa: The apparent axial ratio b/a of the photographic image of the nebula.

These results may be compared with the measurements of the internal absorption in spirals made by Holmberg (3). He gives a plot of the total photographic absorption as a function of the apparent axial ratio for two groups of spirals, the first group comprises spirals of types Sc+ and Sc- and the second group comprises types Sb+, Sb- and Sa. His results for the two groups have been averaged and the variation of absorption with b/a is shown by the broken line in Fig. 2; the zero of this curve has been arbitrarily chosen to facilitate a comparison between the results. The radio observations are in reasonable agreement with the photographic measurements and this comparison therefore confirms the suggestion that the dependence of the radio index on b/a is due to the internal absorption of light. It is interesting to note that similar radio observations, if conducted on a sufficiently large number of galaxies, might provide a valuable technique for measuring the internal absorption of light.

In view of the agreement between the present observations and those of Holmberg, we have used his values to apply an *inclination correction* $\Delta m(i)$ to the observed values of the radio index in order to correct them all to a standard inclination of 90° . These values of $\Delta m(i)$ are shown in Table III and have been added to the observed radio index $R(i, \beta)$ to give the radio index $R(90, \beta)$ corrected to an inclination of 90° .

However, it should be pointed out that the observations of Holmberg show a considerable variation in the internal absorption between individual galaxies; the broken line in Fig. 2 being an average of measurements of a large number of objects. It is only for values of b/a less than about 0.4 that the mean value of the absorption becomes significantly greater than the dispersion between individual galaxies. The radio measurements show a similar effect, a significant change of radio index with b/a being apparent only for the three almost edge-on spirals. It follows that when dealing with individual galaxies it is only worthwhile to apply an inclination correction when the value is of b/a less than about 0.4. However, for less inclined galaxies the corrected values are of importance when considering the average radio index of a number of galaxies.

5.3. *The effect of the absorption of light in our Galaxy on the radio index.*—The effect of absorption of light in our Galaxy would be to decrease the observed radio indices at low galactic latitudes. Only two of the galaxies observed lie close to the galactic plane where this absorption is likely to be serious, namely IC 342 and NGC 6946. The average radio index of these galaxies, corrected to inclination 90° is -0.2 compared with the average for the remainder of $+0.9$, suggesting that the absorption at latitude 11° is about 1.1 magnitude.

The results therefore suggest that the radio index increases with galactic latitude although the data are obviously too scanty to establish the law of this variation. The correction for galactic absorption found by Hubble (8) gives the average increase of photographic absorption relative to the galactic pole as $0.25 (\csc \beta - 1)$. Thus the absorption at latitude 11° should be 1.1 magnitude which is in agreement with the value deduced above from the radio data.

5.4. *The average radio index of a spiral galaxy.*—The radio index $R(90, 90)$ for galaxies with $m'_{pg} < 9.1$ is plotted in Fig. 3 against m'_{pg} , the photographic magnitude corrected for the absorption of light, where

$$m'_{pg} = m_{pg} - \Delta m(i) - \Delta m(\beta). \quad (5)$$

TABLE III
The radio index at 158 Mc/s

Galaxy	Type	Photographic magnitude	Axial ratio of visible nebula	Galactic latitude	Integrated radio magnitude	Inclination correction	Galactic latitude correction	Radio index uncorrected	Radio index corrected for inclination	Radio index corrected for inclination and to galactic pole
		m_{pg}	b/a	β	m_r	$\Delta m(i)$	$\Delta m(\beta)$	$R(i, \beta)$	$R(90, \beta)$	$R(90, 90)$
NGC 224 (M31)	Sb-	4.33	0.47	-21	5.70	0.60	0.4	+1.37	+1.97	+2.4
253	Sc	7.6†	0.22	-88	8.22	1.95	0	+0.62	+1.67	+1.7
598 (M33)	Sc+	6.19	0.64	-30	7.76	0.20	0.25	+1.57	+1.77	+2.0
IC 342	Sc	8.2†	0.80	+11	7.84	0.10	1.05	-0.36	-0.26	+0.8
2403	Sc+	8.80	0.52	+30	> 9.0	0.30	0.25	> +0.2	> +0.5	> +0.8
2683	Sb-	10.53	0.32	+40	> 9.3	1.20	0.10	> -1.23	0	> +0.1
3031	Sb-	7.85	0.41	+41	9.45	0.70	0.10	+1.60	+2.30	+2.4
4236	Sc+	10.05	0.34	+47	> 8.6	0.70	0.10	> -1.45	> -0.70	> -0.6
4244	Sc+	10.48	0.16	+78	9.31	1.05	0	-1.17	-0.12	-0.1
4258	Sb+	8.9	0.40	+69	9.29	0.80	0	+0.39	+1.19	+1.2
4490	Sc+	10.09	0.53	+73	9.48	0.30	0	-0.61	-0.31	-0.3
4565	Sb+	10.30	0.18	+87	9.76	1.35	0	-0.54	+0.81	+0.8
4631	Sc+	9.71	0.23	+84	9.46	1.0	0	-0.25	+0.75	+0.8
4736	Sb-	8.91	0.90	+76	9.46	0.05	0	+0.55	+0.60	+0.6
4826	Sb-	9.27	0.67	+83	9.32	0.20	0	+0.05	+0.25	+0.3
5055	Sb+	9.26	0.63	+74	> 9.6	0.30	0	> +0.34	> +0.64	> +0.6
5194	Sc-	8.88	0.67	+68	9.03	0.15	0	+0.15	+0.30	+0.3
5236	Sc	7.4†	1.00	+32	7.82	0	0.20	+0.42	+0.42	+0.6
5457	Sc-	8.20	1.00	+59	9.40	0	0.05	+1.20	+1.20	+1.2
6046	Sc-	9.67	0.88	+11	9.47	0.05	1.05	-0.20	-0.15	+0.9

* The corrected photographic magnitude m'_{pg} is the observed photographic magnitude corrected for internal absorption and absorption in the Galaxy, thus: $m'_{pg} = m_{pg} - \Delta m(i) - \Delta m(\beta)$.

† Not included in Holmberg's list. Data from the revision of the *Harvard Survey of Bright Galaxies* by de Vaucouleurs (4).

The distribution of results in Fig. 3 suggests that the two bright galaxies M31 and M33 have unusually high values of R . Since both these galaxies have low photographic magnitudes and comparatively large angular diameters it seems possible that this result may have been produced by some systematic error which is correlated with photographic magnitude. However a re-examination of the original measurements and the associated corrections with this possibility in mind failed to explain these high values of R , and we have therefore reached the conclusion that both these galaxies emit less radio flux in relation to their light than an average spiral.

Fig. 3 also suggests that galaxies with $m_{pg} > +8$ have low values of R . However for these fainter objects the distribution is seriously affected by observational selection introduced by the limited sensitivity of the radio equipment. To illustrate this latter effect the limits of detection have been shown in Fig. 3 as a broken line; any galaxy with an uncorrected radio index lying above this line could not be detected.

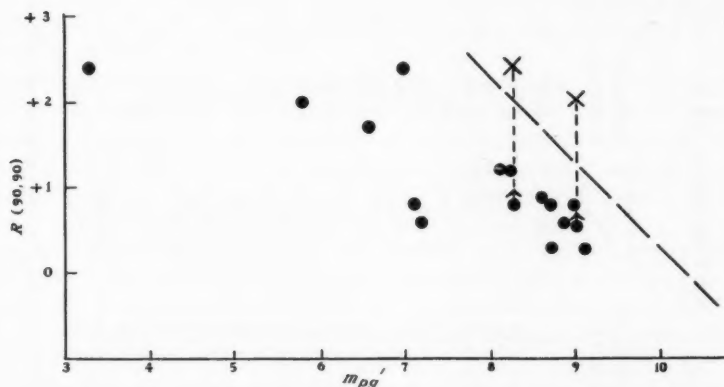


FIG. 3.—The relation between radio index and photographic magnitude for spirals.
Ordinate: The radio index $R(90, 90)$ corrected to inclination 90° and to the galactic pole.
Abscissa: The photographic magnitude m'_{pg} corrected for the internal absorption of light in the emitting galaxy and also in our Galaxy.

It follows from Fig. 3 that the average radio index for those galaxies which were detected is likely to be significantly lower than the true value for the whole group. In an attempt to overcome this difficulty we have made another survey of two of the galaxies (NGC 2403, 5055) with equipment of higher sensitivity and resolving power. In this survey, which was made at 240 Mc/s, the two galaxies were detected successfully and the resulting values of radio index are shown by the crosses in Fig. 3; it has been assumed in reducing these results to 158 Mc/s that the spectral index of both galaxies is equal to that of the reference source 14N5A. If the two measurements at 240 Mc/s are included, then the results are complete for all the sixteen galaxies with a corrected photographic magnitude ≤ 9.1 , and the following analysis of the average radio index refers only to this group.

The average radio index for all sixteen galaxies is $+1.3$ with an r.m.s. deviation of ± 0.8 . The probable error of measurement in the index for a single galaxy is about ± 0.2 ; this has been estimated from the errors in the radio magnitudes alone and the relatively small errors in the photographic magnitudes have been neglected. It is therefore likely that the observed r.m.s. deviation in the radio index is a true dispersion in the properties of spirals and is not due to errors of measurement.

As a check on the effect of the corrections which we have made for the absorption of light we have also calculated the average radio index for those galaxies in the group which have low inclinations ($b/a \geq 0.4$) and which are far from the galactic plane ($\beta \geq 30^\circ$). The mean value of the index for these galaxies is the same as that for the whole group. Thus we may conclude that at 158 Mc/s the radio index of type Sb and Sc spirals is $+1.3$ with an r.m.s. deviation of ± 0.8 .

If we now separate the spirals of type Sb and Sc the corresponding mean values of radio index are $+1.4$ and $+1.2$, and the associated r.m.s. deviations are ± 0.8 and ± 0.7 respectively. Since the probable error of measurement in each of these mean values is about ± 0.1 , it follows that the present survey shows no significant difference between the radio index of the two types; any difference which may exist must be considerably less than the dispersion in the index between individual galaxies of the same type.

It should be noted that, strictly speaking, this comparison refers only to the ratio of the radio to light flux *received* from the two types of galaxy, and does not take into account any difference in the internal absorption of light when received at an inclination of 90° . However, according to Holmberg (3), this difference is small (< 0.2 magnitude) and therefore the comparison may also be taken as valid for the ratio of radio to light flux *generated* in the two types of galaxy.

In an earlier analysis of the radiation from normal galaxies at 85 Mc/s, Mills (9) found values for Sb and Sc spirals of $+0.3(\pm 0.4)$ and $+1.6(\pm 0.2)$ respectively but concluded that "the difference between Sb and Sc galaxies is hardly significant". The results presented here are in agreement with his general conclusion, but do not show a difference of 1.3 magnitudes between the two types.

6. Conclusions

The results of the present survey indicate that at 158 Mc/s the observed radio index of a spiral galaxy of type Sb and Sc, which is a measure of the ratio of the received radio flux to light flux, is a function of the inclination of the visible nebula to the line of sight and of its galactic latitude; they also suggest that these effects are due to the internal absorption of light in spirals and in the Galaxy respectively. In any comparison of the total radio and light flux emitted by a galaxy, it is therefore necessary to take into account these absorption effects.

When corrected for the absorption of light the mean value of the radio index for spirals of type Sb and Sc is $+1.3$ with a dispersion of ± 0.8 magnitude. No significant difference was found between the two types and any difference which exists is less than the dispersion between individual galaxies of either type. It must be emphasized that these conclusions refer only to a frequency of 158 Mc/s and it is possible that the difference between the radio indices of the two types of galaxy may be a function of frequency.

7. Acknowledgments

We thank the Director of the Nuffield Radio Astronomy Laboratories for making available the facilities for this investigation and Dr H. P. Palmer for the use of his unpublished results.

Nuffield Radio Astronomy Laboratories,
Jodrell Bank,
Macclesfield,
Cheshire:

1961 March.

References

- (1) R. Hanbury Brown and C. Hazard, *M.N.*, **119**, 297, 1959.
- (2) W. Baade and R. Minkowski, *Ap. J.*, **119**, 215, 1954.
- (3) E. Holmberg, *Medd. Lund. Obs.*, Ser. 2, No. 136, 1957.
- (4) G. de Vaucouleurs, *A revision of the Harvard Survey of Bright Galaxies*, Australian National University Monograph, 1952.
- (5) D. O. Edge, P. A. G. Scheuer and J. R. Shakeshaft, *M.N.*, **118**, 183, 1958.
- (6) H. P. Palmer, private communication.
- (7) R. Hanbury Brown and C. Hazard, *Phil. Mag.*, **44**, 939, 1953.
- (8) E. Hubble, *Ap. J.*, **79**, 8, 1934.
- (9) B. Y. Mills, *Austr. J. Phys.*, **8**, 368, 1955.

FLARES ASSOCIATED WITH THE 1960 NOVEMBER EVENT AND THE FLARE NIMBUS PHENOMENON

M. A. Ellison, Susan M. P. McKenna and John H. Reid

(Received 1961 March 29)

Summary

Outstanding flares occurred on 1960 November 10, 12, 15 and 20 in association with an active region and complex spot group which had its central meridian passage on November 12.

The last three of these flares projected into space showers of cosmic-rays which were registered on the earth by neutron monitors at *ground level* within 30 minutes after the flare flash, bringing up to ten the number of these events so recorded since 1942 February 28. Geomagnetic storms of unusual intensity also occurred on November 12 and 13, and again on November 15.

The flares of November 10 and 12 were photographed under excellent conditions on films taken at 1-minute intervals with the Lyot $H\alpha$ heliograph at the Royal Observatory, Cape of Good Hope. These results are analysed and flare light-curves are plotted.

A new phenomenon—the flare nimbus—has been found in association with some Class 3 and 3+ flares recorded with the heliograph. This is a *dark* absorbing halo which begins to surround the flare some few minutes after the filaments have reached their maximum light intensity: its duration is > 1–2 hours and its diameter is about 300 000 km. The characteristic properties of the nimbus are described for the five observed cases—1959 July 16, 1960 April 1, June 1, November 10 and 12—and possible causes are discussed. There is a strong presumption that the phenomenon is the optical counterpart of the cloud of relativistic electrons whose occurrence in the flare region has been postulated by Boischoat and Denisse in order to account for the radio emission continuum of Type IV.

1. *Introduction.*—The spot group in latitude 27° N which crossed the Sun's central meridian on November 12.2 gave rise to a remarkable series of flares, the terrestrial effects of which are now being referred to as "the November 1960 event". The group was of Zürich type E and contained 18 spots when it was first seen on the east limb on November 6. By November 12 it had developed into a type F group, containing 60 spots, and on November 14 its area was 1775 millionths of the hemisphere.

The period of greatest flare activity occurred from two days before to three days after central meridian passage, a situation which was most favourable for the reception at the earth of the accelerated particle streams of different energies.

The following major flares were observed:

Date	Class	Co-ordinates	Times U.T.			Source of data
			B	M	E	
Nov. 10	3	29° N 29° E	10^h09^m	10^h21^m	$> 12^h30^m$	Cape film
12	3+	28° N 01° W	13^h15^m	13^h30^m	$> 14^h25^m$	Cape film
15	3+	26° N 35° W	02^h07^m	02^h21^m	04^h27^m	Tokyo, Nizamia

Three others may be noted: an important flare, detected by its radio emission but missed by the optical flare patrol, which occurred on November 11 at about 03^h15^m U.T., one of Class 2 or 2+ which was seen at Tokyo on November 14, beginning 02^h46^m , ending 05^h20^m and a third which occurred when the region was behind the west limb at about 20^h20^m on November 20 (see later).

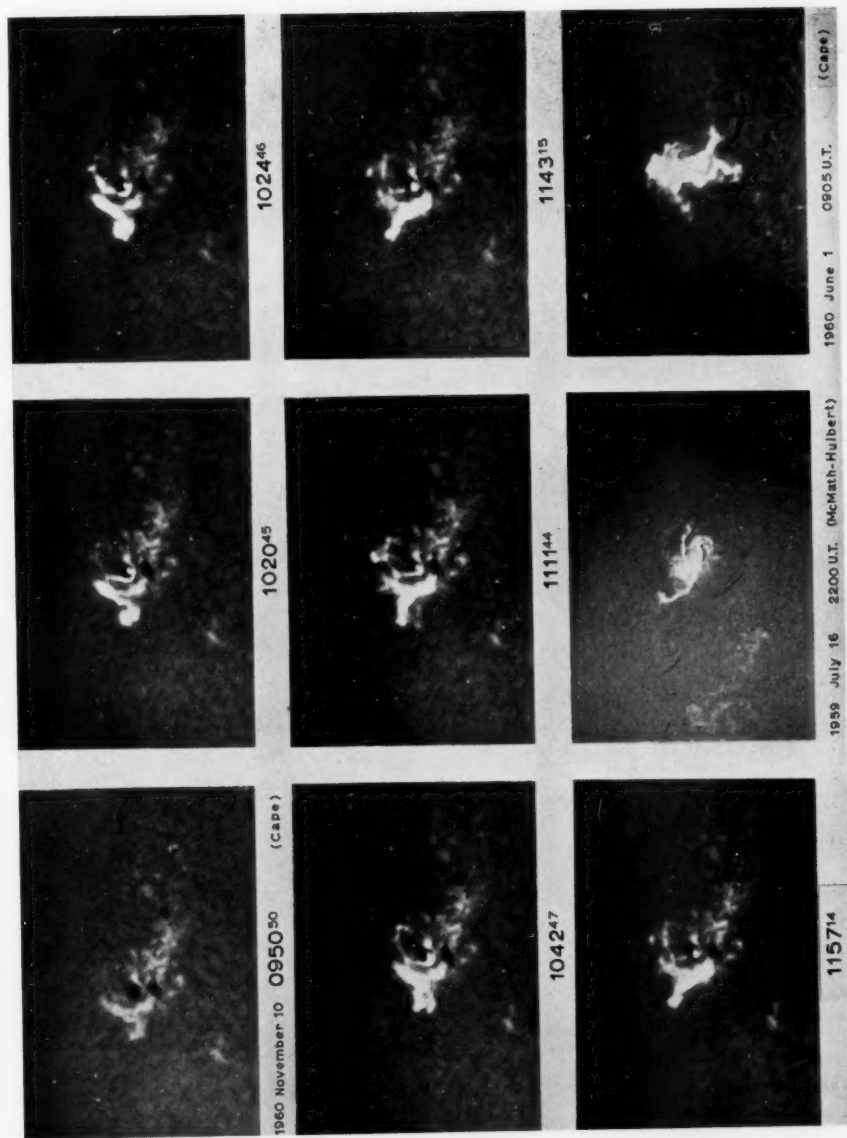
The flares of November 12 and 15 produced showers of primary cosmic-ray particles which were of sufficiently high energy for their secondary effects to be recorded at ground level. Thus, for example, the neutron monitor at Leeds gave an excess counting rate of ~ 100 per cent above pre-flare level following the 3+ flare on the 12th, and an increase of ~ 45 per cent following the 3+ flare of the 15th (privately communicated by Dr P. L. Marsden).

The particles responsible for the first of these cosmic-ray events began to arrive at the Earth at $13^{\text{h}} 28^{\text{m}}$, 13 minutes after the start of the flare and just before the time ($13^{\text{h}} 48^{\text{m}}$ on November 12) of the sudden commencement (S.C.) of a great magnetic storm. The subsequent violent fluctuations of the geomagnetic field, by temporarily lowering the Störmer cut-off rigidity, appear to have allowed unusually great and highly irregular penetration of the cosmic-ray protons into lower latitudes. Another interesting feature of this magnetic storm was the occurrence during the recovery phase of a second sudden commencement ($10^{\text{h}} 23^{\text{m}}$ on November 13) of great amplitude which prolonged the storm for a further 16 hours. It seems likely that the first S.C. may have been caused by storm particles which were accelerated from the flare (unobserved) on November 11 (delay time $34^{\text{h}} 5$) and the second by storm particles from the 3+ flare on November 12 (delay time $22^{\text{h}} 9$). There followed a magnetically quiet period on the 15th during which the second 3+ flare began at $02^{\text{h}} 07^{\text{m}}$, and the resulting cosmic-ray increase started at $02^{\text{h}} 36^{\text{m}}$ with its maximum about 1 hour afterwards. Later on the 15th, a third magnetic storm began with a sudden commencement at $13^{\text{h}} 04^{\text{m}}$.

This same active region was responsible for a third cosmic-ray event at ground level, which began on November 20 at $20^{\text{h}} 55^{\text{m}} \pm 10^{\text{m}}$ (1). The region was then in longitude 111° W and therefore behind the limb, but elevated portions of the flare and of its associated spray prominences were recorded on the Climax films (2).

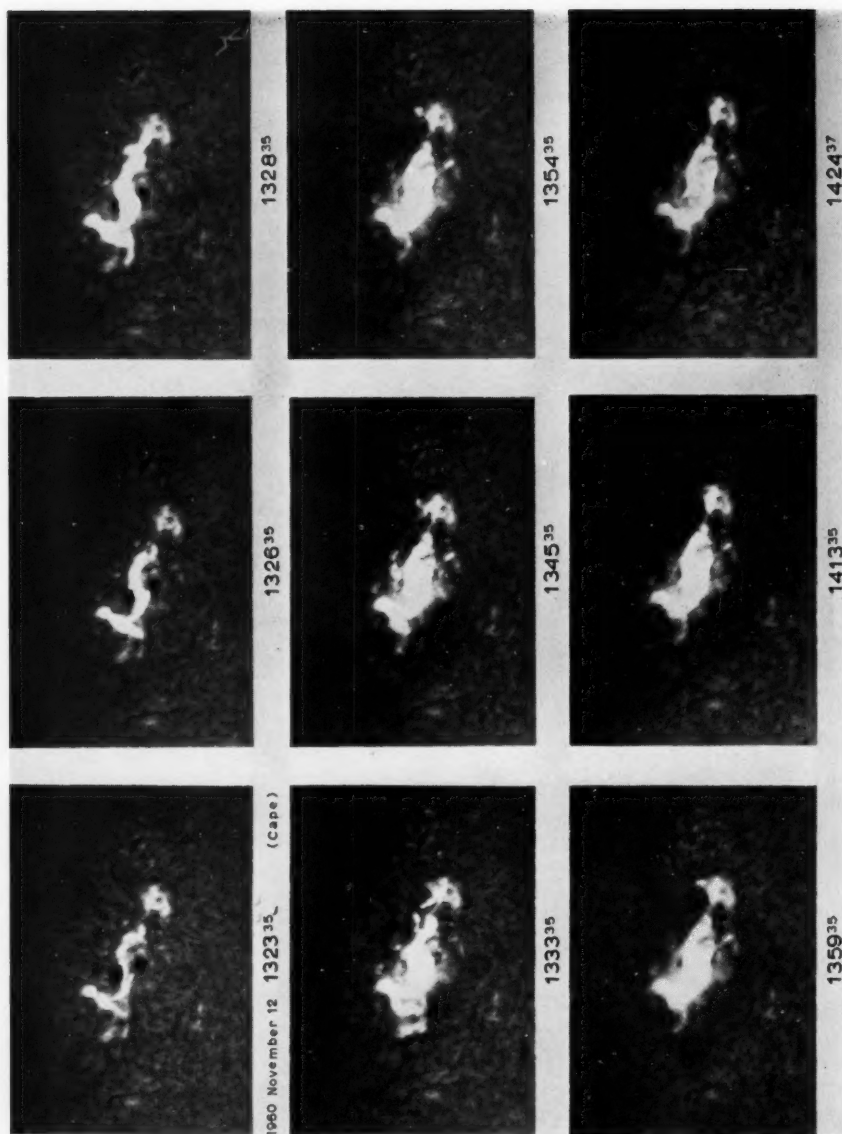
The magnetic storm particles, having energies of < 1 Mev, arrive at the Earth with a time delay of > 18 hours. Flare accelerated protons in the energy range 100–400 Mev are now known to reach the Earth following a few hours after flares of importance 2+ or greater, which are also accompanied by radio emission of Type IV (see Section 5) (3). Some forty examples of this phenomenon have been studied by means of satellites (4), balloons (5) and ionospheric measurements of *polar cap absorption* (P.C.A.) (6). The protons arriving after the flares of November 12, 15 and 20, however, extended into a still higher energy range (1–10 Bev). These produced secondary particles in the atmosphere which were registered by neutron monitors as *ground level effects* (G.L.E.), bringing up to ten the number of such events which have been so recorded since 1942 February 28. While the energies of flare accelerated protons are probably continuous over a wide range, it is useful to distinguish between the low-energy and high-energy events as P.C.A. protons and G.L.E. protons respectively. The flare accelerated particles are thus known to cover a wide range of energies (cf. Section 5).

2. *Class 3 flare of November 10.*—The first of the H α pictures of Plate 7, taken at $09^{\text{h}} 50^{\text{m}} 50^{\text{s}}$ U.T. with the Lyot heliograph at the Royal Observatory, Cape of Good Hope, shows the appearance of the spot group 25 minutes before the flare began. The shape of the bright hydrogen plage to the east (left) and to the north of the two main umbrae should be noted, since it was in this region that



The flares of 1960 November 10, 1959 July 16 and 1960 June 1 showing the nimbus (dark halo).

M. A. Ellison, Susan M. P. McKenna and John H. Reid, Flares associated with the 1960 November event and the flare nimbus phenomenon



The Class 3 + flare of 1960 November 12 showing the nimbus (dark halo), e.g. 14h 13m 35s.

M. A. Ellison, Susan M. P. McKenna and John H. Reid, Flares associated with the 1960 November event and the flare nimbus phenomenon

the principal flare activity occurred. At $10^h 15^m 46^s$ brightening began in five separate small points of this plage and these quickly expanded and linked up to form the bright filaments A, B and C (Fig. 1).

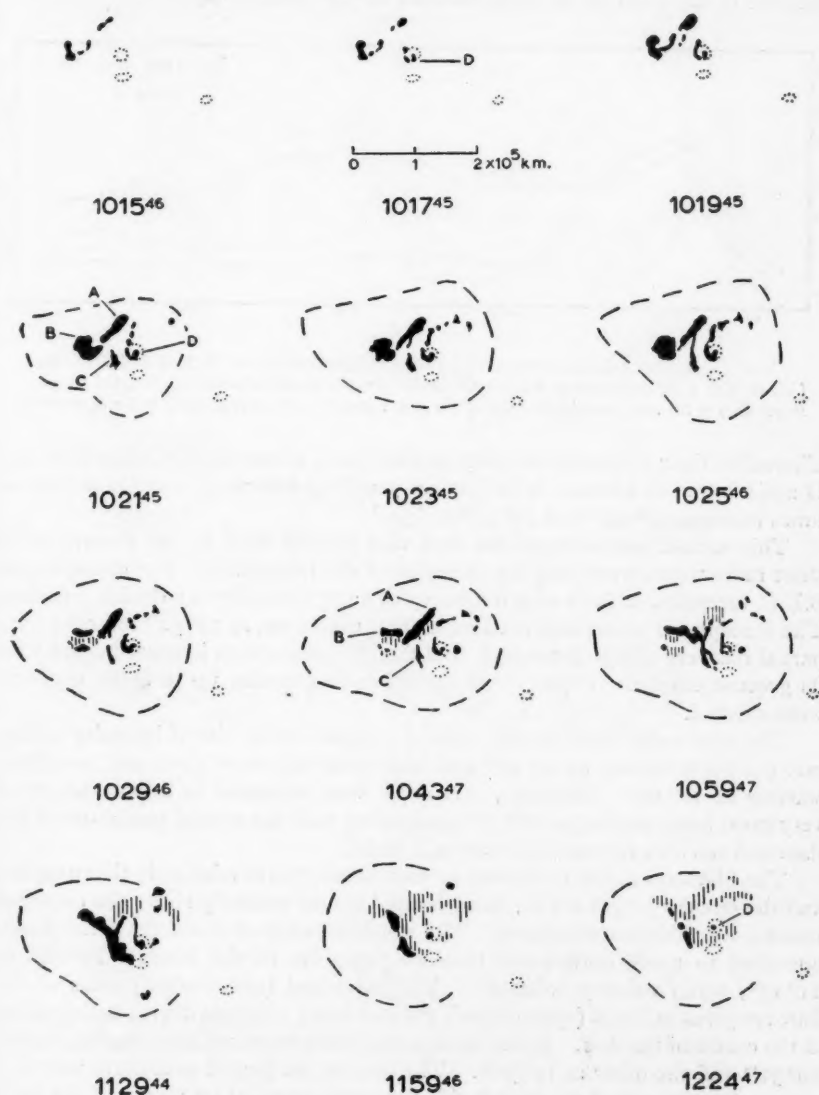


FIG. 1.—Development of Class 3 flare emission filaments, 1960 November 10.

As we can see from the light-curves given in Fig. 2 for the different regions, the increase in light intensity was most rapid between $10^h 15^m$ and $10^h 21^m$ which we regard as the flash phase of the flare. At $10^h 17^m 45^s$ the bright dot D made its

first appearance over the main spot umbra and remained stationary there, with some fluctuations in intensity, up to the last observation at 12^h 31^m. The four regions which were measured photometrically reached their first brightness maxima in the order B, A, D, C between 10^h 19^m and 10^h 24^m.

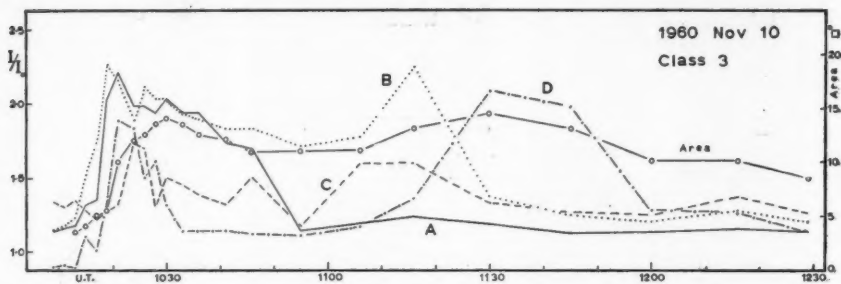


FIG. 2.—Photometric light-curves in $H\alpha$ for the four emission regions (A, B, C and D) of Fig. 1. (See Section 3 for definition of I/I_0 .) The circles give the measured areas (uncorrected for foreshortening) of the total emission in terms of the unit 1 square degree heliographic at the disk centre.

Thereafter their intensities steadily declined until about 10^h 55^m, when B, C and D again began to increase in brightness, reaching secondary maxima at various times between 11^h 05^m and 11^h 30^m.

This second maximum of the flare also showed itself in the absorption of short radio waves traversing the *D*-region of the ionosphere. For example, the B.B.C. reception of Paris on a frequency of 6.175 Mc/s shows a double fade-out. The ionospheric absorption reached its first maximum at 10^h 32^m followed by a partial recovery of signal strength, and then the absorption increased again with its greatest effect at 11^h 30^m. All signals on frequencies up to about 9.5 Mc/s were affected.

The solar radio noise records showed a notable steep rise of intensity on 200 and 545 Mc/s starting at 10^h 20^m and fairly great bursts on 9000 and 3000 Mc/s starting at 10^h 12^m. However, this event was surpassed in importance by a very great burst starting at 11^h 16^m, coinciding with the second maximum of the flare and the area increases of regions B and C.

The filaments A and C showed no movement or drift relative to the sunspots, and the circular bright dot D, being located almost centrally above the principal umbra, was likewise stationary. The northern edge of B on the other hand, appeared to move northwards through 30000 km in the interval 10^h 24^m to 11^h 15^m, mean velocity 10 km/sec. The measured (uncorrected) areas of the flare are given in Fig. 2 (open circles), the unit being 1 square degree heliographic at the centre of the disk. It can be seen that there were two area maxima, one at 10^h 30^m and the other at 11^h 30^m. The area at the second maximum was 14.5 square degrees, and if we correct this for foreshortening by means of the $\sec h$ relation*, h being 38° for the flare, we obtain a corrected area of 18.4 square degrees, or 890 millionths of the hemisphere.

* $A = A_m \sec h$, where A is the corrected area in square degrees, A_m is the measured (i.e. projected) area in terms of the unit 1 square degree at the disk centre, and h is the heliocentric angle. The areas plotted alongside the light-curves are measured areas (A_m). 1 square degree heliographic is equivalent to 48.5 millionths of the hemisphere.

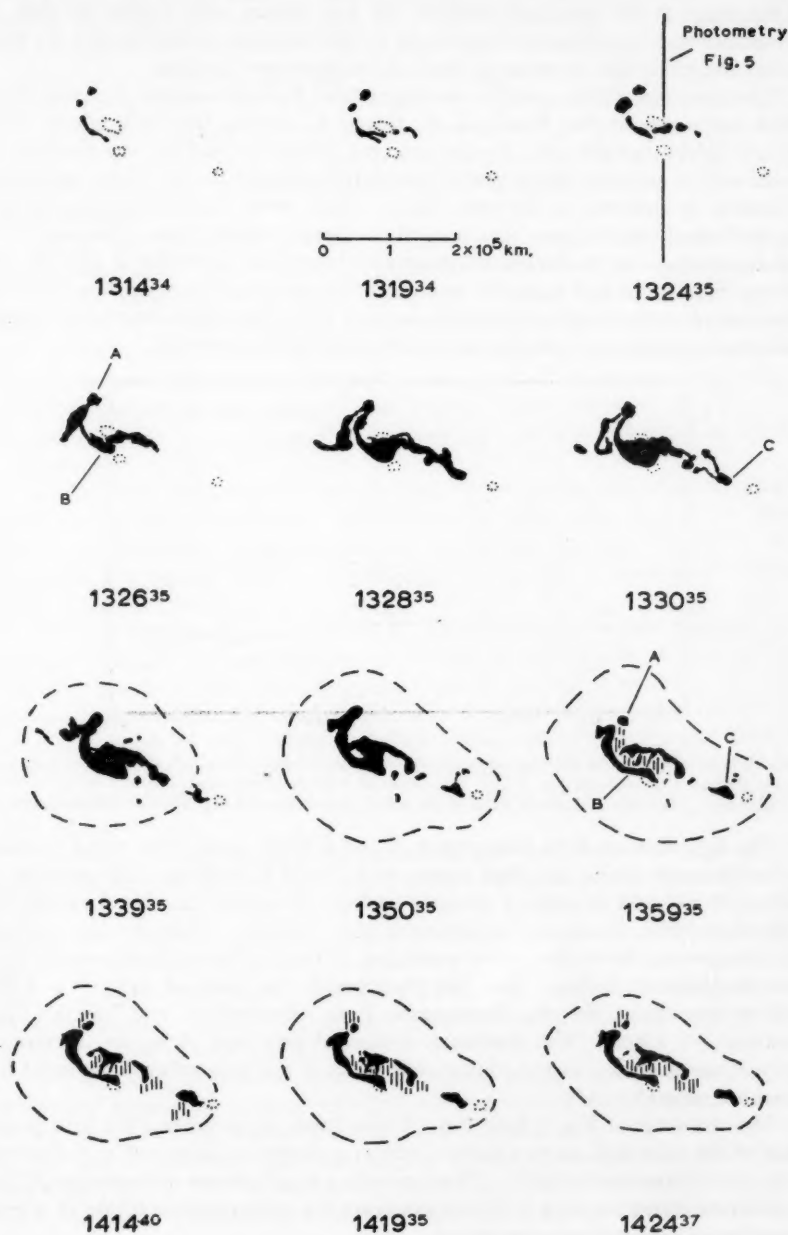


FIG. 3.—Development of the Class 3+ flare emission filaments, 1960 November 12.

3. *Class 3+ flare of November 12.*—This flare began with a development in the plage at the east end (left) of the spot group very similar to that of November 10 but, unlike the former, the bright filaments extended into the west end of the group and covered up both of the large spot umbrae.

The drawings of Fig. 3 and the photographs of Plate 8 illustrate the immensely rapid extension of the filaments A, B and C during the flash phase from 13^h 23^m 35^s to 13^h 28^m 35^s. In the interval 27^m 35^s to 32^m 35^s the filament B broadened to such an extent that it completely covered the two large spots and C flashed up suddenly at the same time. Much more frequent exposures than one per minute would have been needed to follow in detail these extremely rapid developments. In the 60-second interval between the exposures at 26^m 35^s and 27^m 35^s filament B had extended westwards 60 000 km and eastwards 40 000 km. If we interpret these extensions as movements of the luminous material we obtain minimum velocities of 1000 km/sec and 670 km/sec respectively.

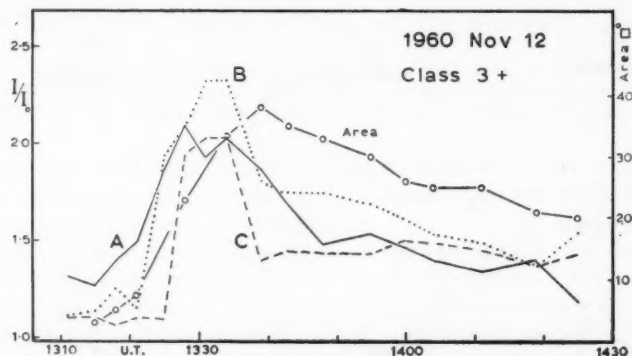


FIG. 4.—Photometric light-curves in $H\alpha$ for the three emission regions (A, B and C) of Fig. 3. (See Section 3 for definition of I/I_0). The circles give the measured areas (uncorrected for foreshortening) of the total emission in terms of the unit 1 square degree heliographic at the disk centre.

The light-curves of the filaments A, B and C (Fig. 4) show the rapid increase in $H\alpha$ intensity during the flash phase, with B and C reaching their maxima at about 32^m 35^s and A some 3 minutes earlier. B and C decreased rapidly in brightness with a slower decline setting in after 13^h 40^m. This time also marked the change-over from the earlier condition of rapid chaotic developments to a state of quiescent fading. Our last photograph was taken at 14^h 31^m and the ending time given by the Sacramento Peak Observatory was 19^h 22^m, i.e. duration ~6 hours. The maximum measured area was 38 square degrees at 13^h 39^m, or 42 square degrees (2040 millionths of the hemisphere) corrected for foreshortening ($h = 25^\circ$).

The drawings of Fig. 3 (and Fig. 1) were made by projecting the heliograph films of the solar disk on to a white circle 11.5 inches in diameter* and drawing in the flare filaments in black. They provide a much clearer appreciation of the filamentary structure than is obtainable from the photographic prints in which the range of contrast is so much less.

The light-curves given in Figs. 2 and 4 express the intensities in terms of the ratio I/I_0 , where I is the measured intensity of the filament and I_0 is the intensity

* This scale is such that 1 degree heliographic at the centre of the disk is equivalent to 0.1 inch.

of the local $H\alpha$ background, measured at a point well away from the flare and having the same heliocentric angle (h). The methods of photometry and the standardization of the films are fully described in an earlier publication (7).

While the measures of I/I_0 give a true indication of the light variations of the flare, as transmitted by the filter (band-pass 0.7\AA), it should be noted that they do not enable us to deduce the central intensities of the $H\alpha$ line for the flare in the absence of a line profile. Our previous spectrographic work indicates that the peak central intensity of the $H\alpha$ line in a 3+ flare is of the order of 300 per cent of the continuum.

The X-ray emission from this flare produced intense ionization in the D -region of the ionosphere. There was a short wave fade-out having a very sudden onset at $13^{\text{h}} 24^{\text{m}}$ (coinciding with the $H\alpha$ flash) with recovery to normal conditions at about 17^{h} . The B.B.C. Tatsfield Receiving Station reported that all short wave frequencies up to 28 Mc/s were affected by this absorption. At Dunsink a sudden enhancement of atmospherics (S.E.A.) was recorded on 24 kc/s, beginning at $13^{\text{h}} 25^{\text{m}}$, maximum at $13^{\text{h}} 33^{\text{m}}$ and ending approximately at 17^{h} . The H-magnetograph also registered a geomagnetic crochet with start at $13^{\text{h}} 24^{\text{m}}$ and maximum at $13^{\text{h}} 31^{\text{m}}$.

4. *The flare nimbus*.—In a recent note (8) we drew attention to what is apparently a new phenomenon associated with some Class 3 and 3+ flares. This is a *dark* halo, some 300 000 km in diameter, which begins to form round the flare region within a few minutes of the time of peak light intensity of the emission filaments.

We have studied five examples of the phenomenon—the flare *nimbus**, as we propose to call it. These occurred in association with the great flares of 1959 July 16, 1960 April 1 (8), June 1 (9) and those of November 10 and 12 described above. For the first case our data have been obtained from a film taken with the Lyot heliograph of the McMath-Hulbert Observatory through the kind co-operation of Dr Helen Dodson-Prince. For examination of the last four we have used our own films taken with a similar instrument at the Royal Observatory, Cape of Good Hope.

Although the appearance of the nimbus is less conspicuous on photographic prints than it is on the original 35 mm films, its general aspect can well be seen in the illustrations of Plates 7 and 8, e.g., Plate 7: 1960 November 10 ($11^{\text{h}} 43^{\text{m}} 15^{\text{s}}$ as compared with $09^{\text{h}} 50^{\text{m}} 50^{\text{s}}$), 1959 July 16 and 1960 June 1; Plate 8: 1960 November 12 ($14^{\text{h}} 13^{\text{m}} 35^{\text{s}}$ as compared with $13^{\text{h}} 23^{\text{m}} 35^{\text{s}}$). In the drawings of Figs. 1 and 3, for the flares of November 10 and 12, the approximate positions of the outer boundary of the nimbus have been marked in (dashed lines) from the times of its first certain appearance.

In Table I we summarize some characteristic properties of the nimbus, such as times of beginning, greatest visibility and maximum dimensions in relation to the flare times. The nimbus makes its first appearance at, or within a few minutes of, the time of maximum flare intensity, as shown by the light-curves. In one case only (June 1) was it seen before maximum. Its most conspicuous phase follows about 30 minutes *after* the flare maximum, and its dimensions then lie within the range $2-4 \times 10^5$ km or $4'.5-9'$. Estimates of the ending times are subject to much uncertainty, but we can say that the duration is $> 1-2$ hours.

* O.E.D.: A cloud, halo or atmosphere, investing a person or thing.

TABLE I

Date	Flare		Nimbus		Radio emission	Cosmic-ray effect
1959	Class	U.T.	U.T.	Greatest diameter 10^6 km	Type IV Mean of times for 545 and 200 Mc/s	
July 16	3+	B 2118	B 2134	~ 3.0	B 2117	G.L.E.
		M 2132	M 2211		M 2159	P.C.A.
		E > 2320	E > 2300		E 2517	B 2250
1960 April 1	3	B 0840	B 0903	2.5	B 0847	P.C.A.
		M 0859	M 0937	3.8	M 0908	B 0945
		E 1320	E 1100		E 1047	
June 1	3+	B 0823	B 0850	1.6	B 0837	P.C.A.
		M 0900	M 0910	2.4	M 0859	(?)
		E 1630	E 1030		E 0937	
Nov. 10	3	B 1013	B 1021	2.1	B 1020 (1116)*	P.C.A.
		M 1021	M 1100	2.9	M 1124	
		E > 1230	E > 1230		E 1350	
Nov. 12	3+	B 1315	B 1332	2.3	B 1327	G.L.E.
		M 1332	M 1400	3.5	M —	B 1328
		E > 1425	E > 1425		E 1757	P.C.A. B 1354

* Two distinct events corresponding to the double maximum of the flare (see Section 2).
Notation: For flares: B, M and E signify the times of beginning, maximum brightness and end.

For the nimbus: B, M and E signify the times of first certain appearance, maximum visibility and end of visibility.

P.C.A.: polar cap absorption in the D-layer, produced by solar protons (100–400 Mev range).

G.L.E.: ground level effect of solar protons (Bev range), recorded by neutron monitors.

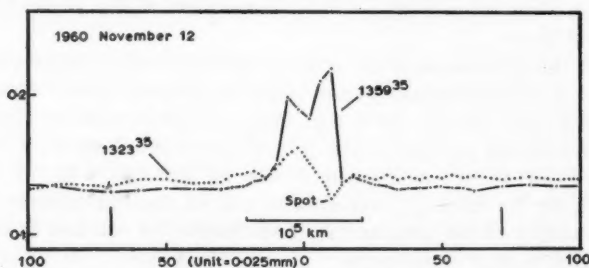


FIG. 5.—Photometric intensity plots across the sunspot group in a N-S direction (see Fig. 3) before the appearance of the nimbus (dotted line) and at the time of its greatest visibility (full line). Diameter of original solar image = 15 mm.

5. *Discussion.*—Fig. 5 presents a photometric examination of the nimbus. Intensity curves were plotted for two film frames on November 12, measures being taken along a N-S line intersecting one of the main sunspots (see Fig. 3). The first frame ($13^h 23^m 35^s$) records the conditions before the nimbus appeared and the second ($13^h 59^m 35^s$) relates to the time of its greatest visibility. The vertical separation between the two curves represents a darkening due to the nimbus of the order of 5 per cent of the continuum near $H\alpha$, and the diameter is

at least 300 000 km. We can rule out the possibility which we first considered that the nimbus might be caused by non-uniform development of the emulsion (Eberhard effect) at points in close proximity to the brilliant flare filaments; for the most conspicuous phase of the nimbus always occurs long after (~ 30 min) the filaments have passed their greatest brightness. The reality of the phenomenon is undoubted. We are also struck by the fact that all five cases we have examined have been associated with two other comparatively rare flare phenomena: (1) the acceleration into space by the flares of streams of protons having energies in the cosmic-ray range, and (2) the emission by the flares of radio noise radiation having Type IV continuum.

The continuum radiation of Type IV was discovered by Boischoat, who also investigated its properties (10). It usually begins near the time of flare maximum in $H\alpha$, has a duration of several hours and is characterised by a smoothness of intensity quite unlike the other types of flare radio outbursts, or the noise storms. The maximum intensity is reached some 20–30 minutes after the start of the emission. The size of this radio source on the Sun has been measured on a number of occasions with the Nançay interferometer on a frequency of 169 Mc/s and has dimensions of the order $7' - 12'$. There is evidence for an initial motion of ascent into the corona, but during the period of decay the source appears to be stationary and its dimensions practically constant. In order to account for such properties Boischoat and Denisse have put forward the view (11) that this radiation is of the synchrotron type and originates in a cloud of relativistic electrons moving in a magnetic field. The power radiated on frequency 169 Mc/s requires about 100 electrons per cm^3 having energies of the order of several Mev in a field of a few gauss. It is probable that these high-energy electrons and the cosmic-ray protons have a common origin in the flare discharge.

It is clear that the characteristics we have found for the flare nimbus, namely its time of commencement, time of maximum visibility and dimensions (Table I) are closely comparable with those of the Type IV continuum radiation. We are bound to conclude that there is a direct relation between the two phenomena. In other words, we regard the nimbus as the optical counterpart of the postulated cloud of relativistic electrons.

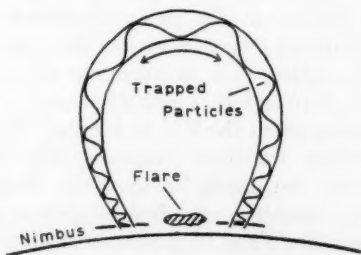


FIG. 6.—Trapping of high energy particles in the coronal region above a flare. The particles are assumed to oscillate between points of reflexion located in the chromosphere.

It is not obvious why these high-energy electrons should have any visible effects at the chromospheric level. However, the electrons are not stationary: each is moving in a helical trajectory along lines of force and will perform oscillatory movements between reflexion points in the magnetic field. A typical

magnetic loop in the coronal region above a flare is shown in Fig. 6. Magnetic fields of this type are a characteristic feature of the coronal (5303) films, such as those taken at the Sacramento Peak Observatory. They likewise show up in the great loop prominences ($H\alpha$) which frequently form over an active region on the limb following a major flare. These regions may well act as magnetic traps for high-energy particles during their lifetime, which may be of the order of a few hours. Energy decay through collisions will be most rapid at the reflexion points in the chromosphere. By analogy with the outer van Allen radiation belt the flare and sunspot group may thus be surrounded by an "auroral zone" in which these collisions are most numerous. We do not, of course, expect any emission of light, but rather the reverse, an absorption of light caused by the excitation of neutral hydrogen with a corresponding increase in the number of hydrogen atoms in the second quantum level.

For two of the flares we have been considering, 1960 April 1 and June 1, we have reported (8, 9) changes in the $H\alpha$ striation patterns surrounding the sunspot groups which took place near the times of maximum flare intensity. We attributed these changes to a rapid partial destruction of the *chromospheric* magnetic field brought about by the flash of the flare. Both these flares exhibited the dark halo. At present we are inclined to regard the two phenomena—the halo and the changes of striation pattern—as quite separate and distinct manifestations of the flare process. The changes in the striation patterns are the more difficult to observe, requiring for their investigation continuous seeing of the highest quality combined with film exposures of suitable density.

6. *Acknowledgments.*—Our grateful thanks are due to our collaborators at the Royal Observatory, Cape of Good Hope, under Professor R. H. Stoy; J. Churms in charge of the Lyot heliograph, assisted by Mrs E. Fiamingo, J. D. Laing, R. Lake and D. S. Malan. The checking of the electronic circuits has been in the care of C. J. Lombard.

We are greatly indebted to Dr A. D. Fokker, World Data Centre C for Solar Radio Emission at N.E.R.A. and to Mme M. Pick, Meudon, who have kindly supplied us with helpful advice and detailed information relating to the Type IV events; to H. V. Griffiths, Engineer-in-Charge of the Tatsfield Receiving Station of the British Broadcasting Corporation, for recordings of ionospheric absorption on 6.175 Mc/s; to Dr Helen Dodson-Price and Miss E. Ruth Hedeman, McMath-Hulbert Observatory, for allowing us to study the film of 1959 July 16 and for making their independent estimates of the times of the halo; and to Dr G. C. Reid and H. Leinbach, Geophysical Institute, University of Alaska, for information about the P.C.A. events. Our thanks are also due to many others with whom we have discussed the halo problem, including Dr Constance Warwick, Sun-Earth Relationships Section, National Bureau of Standards Laboratory, Boulder, who first suggested the possible connection between the nimbus and the Type IV continuum radiation.

One of us (S. M. P. McK.) is indebted to the Royal Society for the grant of an I.G.Y. Bursary.

*Dublin Institute for Advanced Studies,
School of Cosmic Physics,
Dunsink Observatory,
Co. Dublin:*

1961 March 17.

References

- (1) H. Carmichael, J. F. Steljes, D. C. Rose and B. G. Wilson, *Physical Review Letters*, **6**, 49, 1961.
- (2) Richard T. Hansen, *Physical Review Letters*, **6**, 260, 1961.
- (3) T. Obayashi and Y. Hakura, *J. Geophys. Res.*, **65**, 3131, 1960.
- (4) R. L. Arnoldy, R. A. Hoffman and J. R. Winckler, *J. Geophys. Res.*, **65**, 3004, 1960.
- (5) J. R. Winckler and P. D. Bhavsar, *J. Geophys. Res.*, **65**, 2637, 1960.
- (6) G. C. Reid and H. Leinbach, *J. Geophys. Res.*, **64**, 1801, 1959.
- (7) M. A. Ellison, Susan M. P. McKenna and J. H. Reid, *Dunsink Observatory Publications*, **1**, 1, 1960.
- (8) M. A. Ellison, Susan M. P. McKenna and J. H. Reid, *The Observatory*, **80**, 149, 1960.
- (9) M. A. Ellison, Susan M. P. McKenna and J. H. Reid, *Dunsink Observatory Publications*, **1**, 39, 1961.
- (10) A. Boischot, *Ann. d'Astrophys.*, **21**, 333, 1958.
- (11) A. Boischot and J. F. Denisse, *Comptes Rendus*, **245**, 2194, 1957.

THE DUST CONTENT OF THE SMALL MAGELLANIC CLOUD FROM COUNTS OF NEBULAE

A. J. Wesselink

(Communicated by the Radcliffe Observer)

(Received 1961 April 13)

Summary

Counts of nebulae in and near the Small Magellanic Cloud show a clear deficit when compared with outside fields. Contrary to current opinion it is shown that a normal dust content is in accord with these findings.

Introduction.—In 1951, H. Shapley discussed the question of transparency of both the Large and the Small Magellanic Cloud on the basis of counts of extragalactic nebulae. Though he finds very definite evidence of absorption in the Large Magellanic Cloud, the following statement summarizes his view on the Small Cloud absorption: "...an examination of the tabulated numbers and of Figure 2 shows that the Small Magellanic Cloud is essentially transparent" (1). Further we read (2): "An interstellar absorption in the inner section of the Cloud of two or three tenths of a magnitude is not out of the question". In a later paper (3) Shapley states: "My evidence for the transparency of the Small Cloud should not be overvalued because of the conspicuous irregularities in some parts of the sky in the areal population of faint galaxies". However, we read (4) in a radio astronomical study of the Magellanic Clouds: "An important result from this survey is that the amount of gas in the two Clouds is about the same whereas the Large Cloud is believed to contain much more dust than the Small Cloud. Thus the ratio of gas to dust, which has often been held to be constant everywhere is very different in the two systems". Further we find (5): "...although there is evidence that the Large Magellanic Cloud population is more extreme (i.e. younger) than the Small Magellanic Cloud. The latter view is supported by the greater quantities of ionised hydrogen and dust associated with the Large Magellanic Cloud". Again (6): "...On the other hand, dust is observed in the Large Cloud but not in the Small Cloud".

In spite of Shapley's own doubt with regard to the transparency of the Small Magellanic Cloud as found by him in 1951, these quotations show clearly that the absence of dust is generally considered to be a well-established fact by others.

In view of the importance of the question in relation to evolutionary problems of the Small Magellanic Cloud, we have tried to reassess the situation using new counts of nebulae.

Observations.—The plates were taken at the Newtonian focus of the Radcliffe 74-inch telescope. The scale is 1 mm = 22".45. The emulsion was Kodak 103aO

almost without exception though in a few instances 103aE, 103aD have been used. As the faint extragalactic nebulae are red they were expected to show up more easily on the latter emulsions; moreover the extinction should be smaller at the longer wave-length. However, not much difference was found in the usefulness of the three emulsions for our purpose. It was rare that nebulae visible on the one brand could not be seen as well on the other kind if exposure times and quality were similar. The 74-inch telescope was used at its full aperture. The plates were of quarter-plate size covering 0.27 of a square degree. The standard exposure time was half an hour but exposure times ranging from 15 minutes to one hour have been used.

In an investigation of this nature it is all-important to discriminate between faint nebulae and faint stars. Accordingly the observations of a particular field were continued until a plate of acceptable quality was obtained. Though the larger part of the material used was specially obtained for the present problem, several plates already existing at the Observatory could be used to advantage and were searched for nebulae. These were especially found among the long series of plates taken of NGC 121, NGC 1466, the Sculptor system and a field $00^h 47^m 3-73^\circ 46'$ (1875), of a region in the SMC chosen for the study of variable stars. Clearly it was not difficult to find plates of excellent quality of regions where there were many plates. Apart from the material just mentioned 45 plates with a total exposure time of about 35 hours were taken for the present study. The somewhat random choice of fields within the main body of the Cloud and close to it is indicated in Table I. Of these, 28 plates with an exposure time of 23 hours were considered of sufficient quality for the nebular search.

The search for nebulae was usually made on pairs of plates using the blink microscope kindly loaned to the Radcliffe Observatory by the Royal Observatory at the Cape.

In many cases only the best available plate of a region was examined but frequently two good plates were helpful for discrimination between plate defects and genuine nebulae. The plates were searched three times, whereafter a decision was taken on the number of genuine nebulae in the particular field together with an estimate of the quality of the result. The quality was given on a scale of 1-10, 1 being very poor and 10 being perfect. The figure was determined almost entirely by the seeing. In spite of the fact that every effort was made to secure at least one plate for every field in good seeing, results with qualities ranging from 4-9 have been discussed. Quality 10 was never assigned.

After completion of the counts, the results were rendered as homogeneous as possible by applying corrections dependent on quality, exposure time and atmospheric extinction. Variations in reflectivity of the mirrors, sensitivity of the emulsions, and the photographic processing were treated as accidental errors.

Unfortunately our material was not extensive enough to derive the relation between count and quality independently. I have therefore used the corresponding relation as derived by Hubble in his great survey of faint extragalactic nebulae (7). Accordingly I have equated, admittedly a rough procedure, his FP with my quality 3, his E with my class 9. I further interpolated linearly for his other classes. At Pretoria maximum transparency does not usually coincide with best seeing. If, therefore other conditions prevail at Mt Wilson there is some further reason to query the accuracy of our procedure. However, we should realize that the results of a study like the present one are subject to a

variety of errors and that rough methods of reduction are both unavoidable and warranted. The counts were all reduced to quality 8.

The reduction for exposure time was effected by means of the relation found empirically by Hubble (8):

$$\Delta \log n = 1.29 \Delta \log (\text{exposure time}).$$

The counts were reduced on an exposure time of 30 minutes using this formula.

The formula for the correction for atmospheric extinction derives from the extinction coefficient for photographic light and the formula describing the variation of n with apparent magnitude in a uniform universe. For this reduction I have used Table VI from Hubble (9). The counts were reduced to the zenith.

In Table I the results for the various fields have been collected. Columns 1 and 2 give the position of the centre of the field for 1875. Column 3 gives the distance of the centre of the field from the position $0^h 50^m 0^s$, $-73^\circ 15'$, which is somewhat arbitrarily taken as the centre of the Small Magellanic Cloud. Column 4 gives the actually counted number of extragalactic nebulae n_c . Column 5 gives the number derived from column 4 but reduced to the standard conditions of 74-inch telescope, Kodak 103aO emulsion, 30 minutes exposure time, quality 8 and zenith. Column 6 gives the galactic latitude.

It is seen that there are no fields with galactic latitudes smaller than 40° . As there seems to be very little, if any, galactic absorption in the direction of the Small Magellanic Cloud (10), we did not correct for it, though the difference between a field at the galactic pole and one at galactic latitude 45° , according to Oort's discussion of the Hubble counts (11), would amount to $0^m.50 - 0^m.31 = 0^m.19$. The corresponding $\Delta \log n$ is $0.6 \times 0.19 = 0.12$.

In Fig. 1 the numbers n_r have been plotted against the distances Δ . The dotted line indicates the mean n_r for the eight outlying fields with $\Delta > 4^\circ$, which is $n_r = 16.7$. On the right-hand side of the figure a scale is shown indicating various amounts of absorption on the assumption of no Magellanic Cloud absorption to correspond with the above figure of 16.7. The other scale divisions for various absorptions A were computed from the relation

$$A = \frac{1}{0.6} (\log 16.7 - \log n_r).$$

Accuracy of the results.—The accuracy of the directly counted numbers n_r is in the first instance controlled by statistical fluctuation which is measured by its standard error: $\pm \sqrt{n_c}$. The figure is further inaccurate as a consequence of misses which reduce the number. On the other hand the figure is erroneously increased by the counting of objects as nebulae which really are poorly resolved close stellar images. The inclusion of cloud nebosity increases the count erroneously. Hubble is of the opinion that the misses and the positive errors will compensate each other on the average.

The n_r or the reduced numbers were derived from the n_c by multiplying them with a factor depending on quality, exposure time and atmospheric extinction. The uncertainty of the n_r therefore involves both that of the n_c and that of the factor.

Discussion.—In spite of the uncertainties affecting the n_r , Fig. 1 shows a marked lack of nebulae in and near the Small Magellanic Cloud as compared with the numbers found outside it. If interpreted as due to absorption, our results seem

TABLE I

α		δ		Δ	n_c	n_r	b
1875							
h	m	°	'	°			°
21	58.6	-67	07	15.3	18	9.3	-44
23	16.9	-72	19	4.7	25	13.8	-45
00	01.5	-72	54	3.5	12	19.0	-45
00	19.4	-73	29	2.3	14	17.8	-44
00	21.1	-72	13	2.4	9	9.8	-46
00	33.8	-73	49	1.3	3	3.8	-44
00	39.8	-74	31	1.5	2	3.2	-44
00	40.0	-72	57	0.8	4	2.2	-45
00	47.2	-72	27	0.8	2	1.1	-45
00	47.3	-73	46	0.6	0	0.0	-45
00	52.5	-74	24	1.2	7	3.6	-44
00	54.0	-34	22	38.9	59	29.0	-83
00	54.9	-72	51	0.5	0	0.0	-45
00	58.0	-71	31	1.9	2	3.9	-46
00	59.4	-72	43	0.9	0	0.0	-45
01	00.4	-73	52	1.0	1	0.6	-44
01	04.5	-73	33	1.1	1	1.3	-45
01	06.3	-73	38	1.2	3	2.1	-44
01	06.6	-73	25	1.2	1	0.7	-45
01	10.0	-74	00	1.6	2	1.0	-44
01	40.9	-44	06	29.7	14	28.2	-70
02	03.6	-72	12	5.7	10	7.8	-45
02	34.0	-35	02	39.5	22	12.3	-65
03	45.2	-72	04	12.8	14	17.8	-40
03	50.0	-68	50	14.8	11	15.5	-41

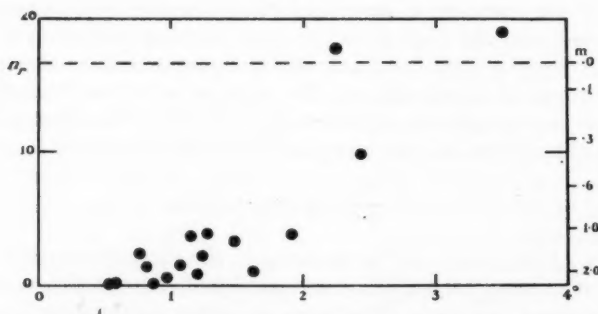


FIG. 1.—Numbers of extragalactic nebulae (ordinates) against angular distance of field from centre of Small Cloud (abscissae).

The dotted line corresponds to the mean of 8 fields each at more than 4° from the adopted centre.

to indicate an amount of rather more than a magnitude; an absorption of the order of $0^m.2$ or $0^m.3$ as advocated by Shapley (2) seems to be quite out of the question. Our results are therefore at variance with the belief that the Small Magellanic Cloud is transparent and there seems to be no reason to doubt that it might contain a normal amount of dust.

Unfortunately it is not possible to give an accurate estimate of the absorption from our data. This is a consequence of the fact that the number of nebulae is not only reduced by absorption but also by the star density. In a transparent

but crowded field the number of extra galactic nebulae counted will be smaller than in regions with low star density.

The examiner of the plates is less certain of the true character of a nebulous image in a crowded field, since he knows that poor resolution of close stellar images is frequently occurring there. The writer has carried out an experiment to prove this effect by superposing two negatives, film to film, and so counting the nebulae present on both plates. The one plate contained relatively few stars but several genuine nebulae. The other was a negative of a dense field in the Small Magellanic Cloud. While the combination contained hardly more stars than the crowded negative, only about half the number of nebulae present on the other could be found.

Our results depend on the ratio of the number of nebulae found in and outside the Small Magellanic Cloud. It is therefore differential and does not depend on the actual number of nebulae brighter than a certain limiting magnitude. It is for this reason that we did not find it necessary to correct for coma as was done by Hubble in his great survey of nebulae. But Hubble was interested in the actual number of nebulae down to a certain limiting magnitude. It is nevertheless of some interest to compare our results, uncorrected for coma, with those of Hubble (uncorrected).

Hubble (12) finds 92 nebulae per square degree with the Mt Wilson 100-inch telescope, 1 hour exposure, Eastman 40 emulsion, at the pole of the Milky Way, and at the zenith.

In my experience Kodak 103aO is about 1 magnitude more sensitive than Eastman 40. Reducing my result of 17 nebulae per 0.27 square degree, 30 minutes' exposure and Kodak 103aO emulsion and Radcliffe 74-inch telescope to Hubble's conditions, I find 102 nebulae. Considering the many uncertainties involved in such a comparison the agreement between Hubble's and my results is surprisingly good.

I am greatly indebted to Dr A. D. Thackeray who encouraged me to publish my results and who gave me the benefit of many discussions. Dr Thackeray, very generously, allowed me the use of many plates taken by him.

Radcliffe Observatory,
P.O. Box 373,
Pretoria,
South Africa:
1961 April.

References

- (1) Harlow Shapley, *P.N.A.S.*, **37**, 136, 1951 (Harv. Repr. 345).
- (2) Harlow Shapley, *Ibid.*, p. 137.
- (3) H. Shapley, *P.N.A.S.*, **39**, 1166, 1953.
- (4) F. J. Kerr, J. F. Hindman and B. J. Robinson, *Austr. J. of Physics*, **7**, No. 2, 297-314.
- (5) B. Y. Mills, *Hdb. d. Phys. Bd. LIII*, Aph. IV, 249, 1960. 1954.
- (6) G. R. Burbidge, *Die Entstehung von Sternen*, 87, 1960.
- (7) E. Hubble, *Ap. J.*, **79**, 33, 1934.
- (8) E. Hubble, *Ibid.*, p. 37.
- (9) E. Hubble, *Ibid.*, p. 32.
- (10) M. W. Feast, A. D. Thackeray and A. J. Wesselink, *M.N.*, **121**, 382, 1960.
- (11) J. H. Oort, *B.A.N.*, **VIII**, 237, 1938.
- (12) E. Hubble, *Ap. J.*, **79**, 59, 1934.

ABSORPTION AND REDDENING IN THE MAGELLANIC CLOUDS

A. J. Wesselink

(Communicated by the Radcliffe Observer)

(Received 1961 April 13)

Summary

The frequency distribution of colour excesses of stars brighter than a given apparent magnitude in distant stellar systems is studied. The frequency distribution (Fig. 1) depends on the luminosity function and the ratio of total absorption to colour excess. It is shown that most stars observed are only slightly reddened even in systems that are optically thick. There is no contradiction with the results of the preceding paper in which nebular counts near the SMC have proved considerable quantities of dust.

1. *Introduction.*—In the preceding paper (1) we discussed the absorption in the Small Magellanic Cloud as shown by the reduction of the numbers of extragalactic nebulae. It was concluded there that total absorptions of over one magnitude may occur, at least in the more central regions, and that in these parts the system may be optically quite thick.

In the present paper we discuss the information on absorption in a distant stellar system as obtainable from colour excesses. In this connection the frequency distribution of colour excesses of stars brighter than some apparent magnitude is of interest.

2. *Frequency distribution of colour excesses of stars brighter than a certain limit of apparent magnitude.*—Consider a certain area in a distant stellar system in which the optical thickness is more or less constant. Let the system be so distant that percentage differences in distance of the member stars from the observer can be neglected.

It is then easily seen that provided we make a suitable adjustment of the zero point of apparent magnitude m we have:

$$m = M + A \quad (1)$$

where M is the absolute magnitude and A is the absorption.

Let the number of stars in the area having absorptions between A and $A + dA$ be $q(A)dA$; and suppose $\phi(M)dM$ represents the number of stars having absolute magnitudes between M and $M + dM$. $\phi(M)$ is therefore proportional to the luminosity function. The number of stars in the area having M between M and $M + dM$, and A between A and $A + dA$, provided there is no correlation between absorption and absolute magnitude, is then:

$$\phi(M)q(A)dM dA. \quad (2)$$

The number of stars having m between m , $m + dm$ and A between A , $A + dA$ is then proportional to

$$\phi(m - A) \cdot q(A) dm dA. \quad (3)$$

The brighter part of the luminosity function can generally be represented with fair accuracy by a form:

$$\phi(M) \sim e^{\alpha M}. \quad (4)$$

Hence, adopting (4) we may write (3)

$$e^{\alpha m} \cdot e^{-\alpha A} q(A) \cdot dm dA \quad (5)$$

and the number of all stars having m between m and $m + dm$ is proportional to

$$e^{\alpha m} \cdot dm \quad (6)$$

which follows from (5) after integration over A .

The same exponential form as (6) holds for the number of stars brighter than some apparent magnitude and clearly is valid not only for a particular area but holds for the entire system.

We now turn to the distribution function of absorptions A . At a given apparent magnitude the number of stars with absorptions between A , $A + dA$ is proportional to

$$e^{-\alpha A} \cdot q(A) dA \quad (7)$$

and since this expression is independent of m it is valid not only at a particular m but for all stars in the area that are brighter than m .

The luminosity function differs from one stellar system to another mainly as a consequence of differences in population. Even in one system variations occur from one region to another. It is therefore not possible to give a definite value for α which is valid generally. However, we are only concerned with the order of magnitude of α and shall accordingly adopt a plausible value.

Schilt, Epstein and Hill (2) derive a value of $\Delta \log N / \Delta m = 0.60$ where N is the number of stars between $m - \frac{1}{2}$, $m + \frac{1}{2}$ for a certain region of the Small Magellanic Cloud. This value 0.60 is close to van Rhijn's result for the bright end of the luminosity function (3). de Vaucouleurs (4) finds $\Delta \log N / \Delta m = 0.76$ for the Small Cloud and only 0.43 for the Large Magellanic Cloud. We shall use $\Delta \log N / \Delta m = 0.60$ as a rough average value. The corresponding value for α is $0.60 \times \log_e 10 = 1.38$.

If A_{\max} is the maximum absorption in the area, in which the maximum amount of absorption is assumed not to vary much, $q(A)$ is not likely to vary much in the interval $0 < A < A_{\max}$. This is exactly true for a system homogeneous in stars and dust. However, the actual absorption is more likely to be patchy. It is possible to calculate $q(A)$ for such a system on the assumption that it is filled with randomly distributed clouds, each of which is capable of absorbing a small but definite amount. Again, the variation of $q(A)$ with A is only slight. Since, then, there is no doubt that the exponential in (7) is the more varying and therefore more important factor we may take $q(A)$ constant with sufficient accuracy and represent the distribution function of the A as being proportional to

$$e^{-1.38 A} dA \quad (8)$$

in the interval $0 < A < A_{\max}$ with a frequency zero for values A larger than A_{\max} . The function is shown graphically in Fig. 1.

We might consider the average absorption for stars brighter than a given apparent magnitude using (8). Because the distribution function is so skew

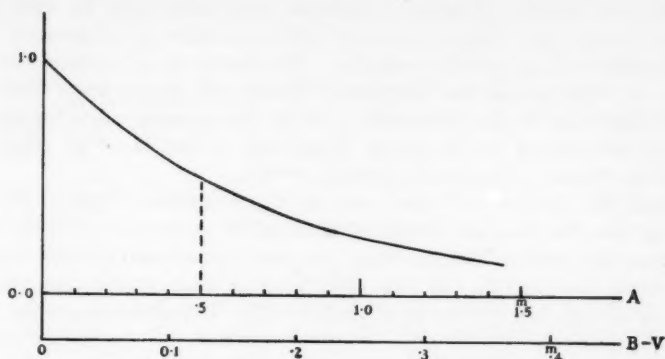


FIG. 1.—Relative frequency of absorptions and colour excesses in distant stellar systems of stars selected according to apparent magnitude.

it is actually simpler to consider the median absorption. Denoting median values with a \sim above the quantity we easily find in case of large A_{\max}

$$\tilde{A} = \frac{\log_e 2}{\alpha} \quad (9)$$

which, with $\alpha = 1.38$, becomes

$$\tilde{A} = 0^m.50. \quad (10)$$

It is of interest that this result is independent of the amount of absorption per parsec. It depends on the luminosity function and the assumption of A_{\max} being large. It follows that two systems which are both optically thick, which have the same luminosity function will have equal \tilde{A} even if their absorptions per parsec are different. However, the observer will see further in the system with the smaller absorption per parsec.

If the luminosity function used corresponds to photographic light and if the selection of stars is according to photographic apparent magnitude, we derive a median colour excess on the $B-V$ scale, $\tilde{E}_{B-V} = \tilde{A}/4.0 = 0^m.12$ if we adopt $A_{pg}/E_{B-V} = 4.0$. When the stellar system is not optically thick we shall find smaller values for the median colour excesses than the values just given. It follows from the analysis that small amounts of reddening do not justify the conclusions that the systems *must* be transparent.

In a study of the brightest stars in the Magellanic Clouds, Feast, Thackeray and Wesselink (5) have discussed the colour excesses of highly luminous B stars in both Magellanic Clouds. They find an average reddening of about $0^m.10$ in either Cloud but it is not quite certain by how much this has to be reduced because of galactic reddening. It is, however, certain that some reddening occurs among our stars in the Clouds themselves. This agrees well with our theoretical prediction for stars selected according to apparent magnitude even if the Magellanic Clouds were both optically thick.

We therefore do not agree with Arp's statement "that some SMC stars are unreddened and that the remainder are no more than slightly reddened" (6).

Down to a certain apparent magnitude most stars may be only slightly reddened, but the few which have large colour excesses are of greatest interest for the problem of the optical thickness. The discovery of a single star highly reddened by dust within the Magellanic Cloud will give a lower limit to the maximal absorption in that direction. So far the greatest value for the visual absorption established in the Large Magellanic Cloud is $0^m.96$ whereas the largest value found in the Small Cloud is $0^m.60$.

Though the discovery of more stars in the Magellanic Clouds with larger reddening than the two just mentioned would be extremely valuable we may yet say that the present data on colour excesses are consistent with my results from nebular counts (1). It was concluded in that article that the Small Magellanic Cloud, like the Large Magellanic Cloud, contains a normal amount of dust.

Radcliffe Observatory,
P.O. Box 373,
Pretoria,
South Africa:

1961 April.

References

- (1) A. J. Wesselink, *M.N.*, **122**, 503, 1961.
- (2) Schilt, Epstein and Hill, *A.J.*, **60**, 349, 1955.
- (3) P. J. van Rhijn, *Gron. Publ.* **47**, 1936.
- (4) G. de Vaucouleurs, *A.J.*, **60**, 226, 1954.
- (5) M. W. Feast, A. D. Thackeray, and A. J. Wesselink, *M.N.*, **121**, 337, 1960.
- (6) H. C. Arp, *A.J.*, **65**, 433, 1960.

THERMAL RADIATION FROM THE MOON AND THE HEAT FLOW THROUGH THE LUNAR SURFACE

J. E. Baldwin

(Received 1961 April 15)

Summary

Observations of thermal radiation from the Moon at a frequency of 178 Mc/s are described, giving a value for the mean disk temperature of $233 \pm 8^\circ\text{K}$, which is the same to within 25°K as various estimates of the mean disk temperature at the surface. The absence of any detectable steady temperature gradient through the surface leads to upper limits on the steady heat flow from the Moon for a range of possible properties of the surface materials. The observations at shorter radio wavelengths favour a model in which a gravelly material extends to depths of at least several metres. For this model the upper limit to the heat flow is very close to that expected from radioactive decay in a Moon of chondritic composition.

1. *Introduction.*—Observations of the thermal radiation from the Moon in the infra-red and at radio wave-lengths have now been made by a large number of workers. The radio measurements show a variation of the apparent temperature with the lunar cycle which is much smaller than that observed in the infra-red and which lags in phase behind the cycle of illumination. A material having a very low thermal conductivity and a small absorption coefficient for radio waves has been proposed to account for these results since, for such a substance, most of the thermal radio emission originates at depths of several cm where the variation of temperature is much smaller than at the surface. The absorption coefficient must decrease with frequency since at lower frequencies no variation of temperature with the lunar cycle has been detected.

A measurement of the apparent lunar temperature at a low frequency can therefore provide a value of the mean temperature far below the surface. If this differs from the mean surface temperature, then a knowledge of the probable value of the thermal conductivity of the materials forming the surface layers leads to an estimate of the steady heat flow through the lunar surface.

In the present paper a measurement of the lunar temperature at a frequency of 178 Mc/s is described first of all. The results of previous observations at higher frequencies are then analysed to determine the probable values of the thermal conductivity and penetration depth for radio waves of the material forming the lunar surface. Upper limits to the heat flow through the surface are derived for a number of models and are compared with the expected heat flow due to radioactivity in the Moon.

2. *Observations at 178 Mc/s.*—The observations were made with the larger section of the interferometric radio telescope at Cambridge (1), which has beam widths to half-power points of 13.6 in right ascension and 4.6 in declination, used with a total power receiver. Sources are observed at meridian transit with this instrument and the procedure in the observations was to record a drift

curve across a region of sky containing the Moon on one day and a comparison record when the Moon was absent on the following day. Portions of two recordings of this kind are shown in Fig. 1.

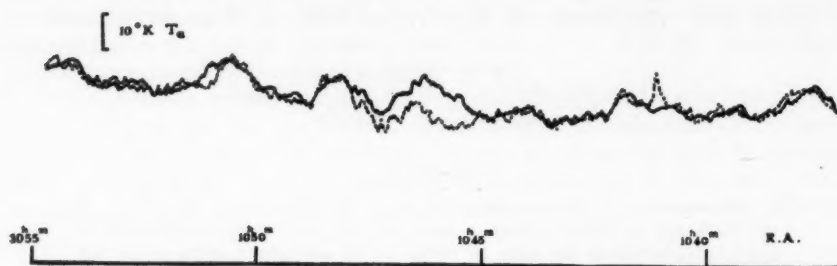


FIG. 1.—Recordings of total power at $\delta = +07^\circ$. Full line: 13.11.60; dotted line: 14.11.60.

At this frequency the sky temperature is comparable with that of the lunar surface. A determination of the lunar temperature, T_m , therefore depends upon an accurate knowledge of the sky temperature, T_s , in the position of the Moon but is relatively insensitive to the properties of the particular aerial system being used to measure the difference ($T_m - T_s$). This feature of the observations contrasts with the microwave measurements where the chief uncertainty is in the forward gain of the aerial system.

The results of several determinations of the lunar temperature at 178 Mc/s are assembled in Table I.

TABLE I

Date	U.T. of transit	α	δ	ΔT_a °K	$(T_m - T_s)$	T_s	T_m
		h m s	° '				
15.9.59	2304	22 40 44	-06 00	5.0 ± 1.0	81 ± 16	157	238 ± 16
16.9.59	2351	23 32 09	-01 54	5.0 ± 1.0	150 ± 30	170	320 ± 30
17.8.60	0812	05 54 46	+18 20	0.0 ± 1.5	0 ± 27	347	347 ± 27
19.8.60	0947	07 37 34	+17 20	6.0 ± 3.0	98 ± 49	180	278 ± 49
20.8.60	1034	08 28 29	+15 36	8 ± 3	174 ± 65	107	281 ± 65
13.11.60	0717	10 46 11	+07 31	8.4 ± 0.8	118 ± 10	117	235 ± 10
27.11.60	1946	00 12 53	-00 34	11.0 ± 1.5	203 ± 27	161	364 ± 27
28.11.60	2034	01 03 43	+03 46	6.1 ± 1.5	173 ± 42	186	359 ± 42

To convert the observed difference in aerial temperature with and without the Moon, ΔT_a , to the true temperature difference, $(T_m - T_s)$, account has been taken of three factors:

- (i) The fraction of the aerial beam occupied by the Moon.
- (ii) The position of the Moon in declination relative to the centre of the beam.
- (iii) The aerial efficiency or the fraction of the total power in the main beam of the aerial. Accurate measurements of the side-lobe pattern have given a value of 0.68.

The quoted values of sky temperature, T_s , were obtained from two series of observations made recently at Cambridge.

(a) A survey of the region of sky $-05^\circ < \delta < +60^\circ$ made by Turtle and Baldwin (in preparation) with the large 178 Mc/s aerial.

(b) Observations by Turtle (in preparation) at 178 Mc/s using an aerial of low gain similar to that used by Costain (2) in which particular attention was paid to obtaining an accurate zero level and sensitivity scale calibrated against thermal loads.

The sky temperatures obtained in (a) were measured relative to the North Pole whose absolute temperature was not determined. Turtle has smoothed the results of (a) to the beam width used in (b) at several different positions on the sky, thus both providing the detailed survey, (a), with an accurate zero level and also a check on the sensitivity scale.

Some of the daytime records were affected by reception of solar emission in weak side-lobes of the main beam, in particular those of 1960 August 17, 19 and 20. The remaining results show a scatter which is much larger than the probable error of each determination. Several effects might lead to such a variation.

(i) Variation with the lunar cycle similar to that observed at wave-lengths near 1 cm. Observations at 22 cm by Davies and Jennison (3) have shown the variation to be < 0.7 per cent and it should be negligible at a wave-length of 168 cm ($\nu = 178$ Mc/s).

(ii) The galactic radiation reflected from the Moon's surface will vary with the position of the Moon in the ecliptic. The results of radar observations have been interpreted by Evans (4) as indicating a reflection coefficient at normal incidence of 0.06. For most positions of the Moon in the ecliptic the reflected radiation will contribute $\sim 30^\circ\text{K}$ to the mean disk temperature but the variation in this quantity will be less than 4°K except at times when the Moon crosses the galactic plane.

(iii) Gradients of sky brightness across the aerial beam may lead to incorrect estimates of T_s , but in all regions of sky used the general gradients are very small. Occasionally, however, the Moon will occult sources of small angular size. There is a probability of 1 in 16 that a source of flux density $1.0 \times 10^{-26} \text{ W. m}^{-2} (\text{c/s})^{-1}$ is obscured by the Moon and in such an event the estimate of T_m is about 15°K lower than the true value.

(iv) Reflected radiation from the Sun and from terrestrial transmitters may be very important. The reflected radiation from the quiet Sun contributes $< 1^\circ\text{K}$ to T_m but even comparatively weak activity on the Sun can produce measurable reflected radiation.

A transmitter on the Earth radiating 100 kw isotropically over a hemisphere at a frequency in the 4 Mc/s bandwidth of the receiver would give an increase in the apparent lunar temperature of 60°K . Interference of this kind could originate from any place where the Moon is above the horizon. Since the frequency of 178 Mc/s lies in a band allocated to television transmission in the United States and in Europe, such transmitted powers may well occur at certain times of day. The most favourable time for lunar observations on the meridian at Cambridge is at about $08^{\text{h}} 00^{\text{m}}$ U.T. All American stations visible from the Moon have local times later than $02^{\text{h}} 00^{\text{m}}$ when the majority will have closed down. Most European stations will not yet have begun transmissions. The low value of T_m obtained on 13.11.60 at $07^{\text{h}} 17^{\text{m}}$ U.T. bears out this expectation.

Fortunately it is possible to distinguish recordings affected by reflected radiation from those on which only thermal radiation is present. In the latter case the Moon behaves as an effectively black disk showing only slight limb

darkening, whereas for reflection it behaves as a comparatively well-polished sphere, the greater part of the reflected radiation coming from an area only about $3'$ arc in diameter at the centre of the Moon. The patterns drawn out in these two cases can be distinguished with the $13'$ beam of the aerial, as illustrated by the recordings of 28.11.60 and 13.11.60 shown in Fig. 2.

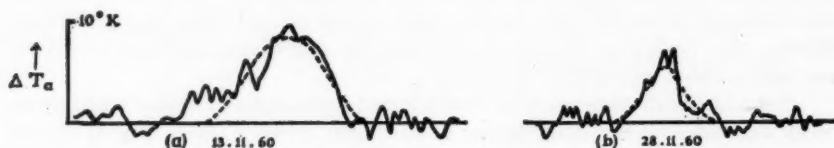


FIG. 2.—Plots of the difference of aerial temperature, ΔT_a , on successive days showing (a) thermal radiation from the Moon and (b) reflected radiation. The dotted curves are the theoretical ones for these two cases.

Only two of the measurements (15.9.59 and 13.11.60) fit the pattern expected for pure thermal radiation. The two values are reasonably in agreement giving a weighted mean value for T_m of $236 \pm 8^\circ\text{K}$. To correct this to the true value of the mean disk temperature requires a knowledge of the dielectric properties of the Moon which are at present uncertain, but the reflection coefficient at normal incidence is probably close to 0.06. The mean sky temperature at 178 Mc/s is $260\text{--}270^\circ\text{K}$, only a little higher than the apparent disk temperature, T_m . It can be shown that, in this case, T_m is approximately 3°K higher than the true disk temperature. We shall therefore adopt 233°K as the mean disk temperature in the following discussion.

3. *Theory of the radio-frequency temperature.*—Analyses by Wesselink (5) and Jaeger (6) of Pettit's observations in the infra-red during a total eclipse of the Moon (7) led to the conclusion that the outermost layer of the surface consists of a material such as finely divided dust having a value of $(k\rho s)^{-1/2} = 1000$ (k = thermal conductivity, ρ = density and s = specific heat). The rate of fall of temperature during the umbral phase of the eclipse indicated that the underlying layers probably have a lower value of $(k\rho s)^{-1/2}$ of about 125, similar to that of dry gravel. The eclipse observations provide information concerning the uppermost few mm of the surface from which most of the heat radiated during the eclipse originates. The nature of the material at greater depths can at present be derived only from observations of the apparent microwave temperature through the lunar cycle.

The problem of the apparent microwave temperature of a homogeneous solid whose surface experiences a sinusoidal variation of temperature has been treated in some detail by Piddington and Minnett (8). If the time variation of the surface temperature is $T_1 \cos \omega t$ then the temperature variation falls off with depth x as $\exp(-\beta x)$, where $\beta = (\omega \rho s / 2k)^{1/2}$. The intensity of radio waves passing through the material falls off as $\exp(-\alpha x)$ where $\alpha = 4\pi\sigma / \epsilon \epsilon^{1/2}$ (σ = electrical conductivity and ϵ = dielectric constant). Then for such a substance the apparent microwave temperature is

$$\frac{T_1}{(1 + 2\delta + 2\delta^2)^{1/2}} \cos(\omega t - \phi)$$

where $\delta = \beta/\alpha$ and $\tan \phi = \delta/(1 + \delta)$.

To calculate the expected variation of microwave temperature at the lunar equator Piddington and Minnett assumed that the surface temperature was determined during the lunar day by equilibrium between thermal radiation and the incident solar flux (i.e. $T_0 \cos^{1/4} \lambda$ where λ is the longitude from the sub-solar point) and was constant throughout the lunar night. More recently Jaeger (6) has made calculations of the variation of surface temperature on the lunar equator assuming only a constant flux of solar heat and radiation from the surface proportional to T^4 . These more accurate calculations provide, in principle, a much more detailed test of various models of the lunar surface. At present, however, most observations have been made with beam widths comparable with or greater than the angular diameter of the Moon. The only two components of the temperature variation which are detected with any efficiency are the steady component T_0 and that having the fundamental period of a lunar month, $T_1 \cos(\omega t - \phi)/(1 + 2\delta + 2\delta^2)^{1/2}$, since higher harmonics are approximately averaged to zero over the lunar disk and are also more rapidly attenuated with depth than the fundamental.

Thus for most of the observations it is sufficient to Fourier analyse Jaeger's curves of equatorial surface temperature to give T_0 and T_1 . The values corresponding to three of his models are given below together with those corresponding to Piddington and Minnett's assumptions. We shall now compare these theoretical values with the observations of the variation through the lunar cycle, from which δ may be derived, and with the observed values of T_0 .

TABLE II

Model	T_0 °K	T_1 °K	T_1/T_0
Piddington and Minnett	249	134	0.54
Jaeger $(kps)^{-1/2} = 1000$	210	160	0.76
$(kps)^{-1/2} = 1000$ layer 0.45 cm thick on top			
of $(kps)^{-1/2} = 125$	222	141	0.63
$(kps)^{-1/2} = 125$	238	124	0.52

4. *Radio observations of the lunar temperature.*—The measurements of the lunar temperature made so far are assembled in Table III.

The numerical values of T_0 and $T_1/T_0(1 + 2\delta + 2\delta^2)^{1/2}$ in columns 3 and 4 are those quoted by the observers. Some of the observations were made with beam widths slightly smaller than the lunar disk and give essentially the temperature of the central point of the disk. These are marked with a letter c in column 5. The remainder are thought to be mean disk temperatures. For the steady component T_0 the theoretical difference between these quantities is small; $T_{\text{mean disk}} = 0.96 T_{\text{mean central}}$ since the temperature falls off with latitude θ only as $\cos^{1/4} \theta$.

The effect on the fundamental variation of period $2\pi/\omega$ of averaging over all latitudes is also small and may be neglected, but the averaging in longitude reduces the apparent variation by a factor of approximately $\pi/4$ relative to that of a point on the surface.

If the Moon is assumed to be composed of materials having a dielectric constant of 2.8 (corresponding to a reflection coefficient at normal incidence of 0.06), then, at wave-lengths where the sky temperature is effectively zero, the apparent central temperature is 0.94 of the true central temperature and the apparent disk temperature is approximately 0.88 of the true disk temperature.

TABLE III

Observer	λ cm	T_0 °K	Observed	Corrected	Corrected
			$T_1/T_0(1+2\delta+2\delta^2)^{1/2}$	T_0 °K	$T_1/T_0(1+2\delta+2\delta^2)^{1/2}$
Tyler <i>et al.</i> (9)	0.75	160	0.10	188	0.13
Salomonovich (10)	0.8	197	0.16	c 209	0.16
Gibson (11)	0.86	185	0.19	c 196	0.19
Piddington (8)	1.25	215	0.17	252	0.21
Zelinskaya <i>et al.</i> (12)	1.63	224	0.16	c 237	0.16
Grebenkemper (13)	2.2	200	0.05	235	0.065
Troitskii <i>et al.</i> (14)	3.2	170	≤ 0.07	200	≤ 0.09
Castelli <i>et al.</i> (15)	10	256	≤ 0.025	c 271	≤ 0.025
Akabane (16)	10	315	0	370	—
Mezger <i>et al.</i> (17)	21	250	≤ 0.02	294	≤ 0.025
Waak (18)	21	230	—	270	—
Westerhout (19)	22	270	—	317	—
Davies <i>et al.</i> (3)	22	270	≤ 0.0035	c 286	≤ 0.0035
Castelli <i>et al.</i> (15)	23	254	—	298	—
Denisse <i>et al.</i> quoted in (20)	33	208	—	244	—
Seeger <i>et al.</i> (20)	75	185	≤ 0.10	209	≤ 0.13
Baldwin	168	236	—	242	—

These correction factors have been applied to the observations to reduce them all to central temperatures on the Moon corrected for emissivity. A crude division of the observations into those in which the central temperature is measured and those in which the mean disk temperature is the measured quantity has seemed adequate for the present discussion. The corrected values of T_0 and the ratio of the fundamental component of the variation to T_0 are given in columns 6 and 7. The ratio of the varying component to the steady component has been chosen for comparison with theory rather than the absolute value of the variation in an attempt to avoid errors due to uncertainties in the calibrations of many of the radio observations.

5. *Derivation of the penetration depth, $1/\alpha$, for different models.*—We shall consider first of all two models in which the surface layers are homogeneous and have the following properties:

Model I: $\rho = 2 \text{ g cm}^{-3}$, $s = 0.2 \text{ cal g}^{-1} \text{ }^\circ\text{K}^{-1}$, $k = 2.5 \times 10^{-6} \text{ cal cm}^{-1} \text{ sec}^{-1} \text{ }^\circ\text{K}^{-1}$.

Model II: $\rho = 2 \text{ g cm}^{-3}$, $s = 0.2 \text{ cal g}^{-1} \text{ }^\circ\text{K}^{-1}$, $k = 1.6 \times 10^{-4} \text{ cal cm}^{-1} \text{ sec}^{-1} \text{ }^\circ\text{K}^{-1}$.

These correspond to Jaeger's models with $(kps)^{-1/2} = 1000$ and 125. The values of T_1/T_0 for these models are given in Table II and using the relations in Section 3 it is possible to calculate δ and α as functions of wave-length, λ ; α is further related to the loss angle of the dielectric, Δ , by $\tan \Delta = \lambda \epsilon^{1/2} \alpha / 2\pi$. The computed values of δ , α and $\tan \Delta$ are presented for Models I and II in Tables IV and V respectively. The dielectric constant has been taken to be 2.8 (Evans (4)). The values of α and $\tan \Delta$ for 0.15 cm wave-length were derived from Sinton's (26) eclipse measurements.

Values of $\tan \Delta$ quoted by von Hippel (21) are given for a number of substances in Table VI. Unfortunately there seem to be no published figures for iron-magnesium silicates of which chondritic meteorites are largely composed

(Urey and Craig (22)) and which are supposed by several authors to form the Moon's surface. It is of interest to compare von Hippel's figures with those deduced from the observations.

TABLE IV

Model I (kps)^{-1/2} = 1000

λ cm	δ	α	$\tan \Delta$
0.15	—	46	$190 \cdot 10^{-2}$
0.75	3.6	0.13	$4.4 \cdot 10^{-2}$
0.8	2.8	0.16	$5.8 \cdot 10^{-2}$
0.86	2.3	0.20	$7.7 \cdot 10^{-2}$
1.25	2.0	0.23	$13.0 \cdot 10^{-2}$
1.63	2.8	0.16	$11.7 \cdot 10^{-2}$
2.2	7.8	0.059	$5.8 \cdot 10^{-2}$
3.2	≥ 5.5	≤ 0.084	$\leq 12 \cdot 10^{-2}$
10	≥ 21	≤ 0.022	$\leq 9.9 \cdot 10^{-2}$
21	≥ 21	≤ 0.022	$\leq 20 \cdot 10^{-2}$
22	≥ 160	≤ 0.0029	$\leq 2.8 \cdot 10^{-2}$

TABLE V

Model II (kps)^{-1/2} = 125

λ cm	δ	α	$\tan \Delta$
0.15	—	5.8	$240 \cdot 10^{-3}$
0.75	2.9	$2.0 \cdot 10^{-2}$	$6.7 \cdot 10^{-3}$
0.8	2.2	$2.6 \cdot 10^{-2}$	$9.4 \cdot 10^{-3}$
0.86	1.7	$3.4 \cdot 10^{-2}$	$13 \cdot 10^{-3}$
1.25	1.6	$3.6 \cdot 10^{-2}$	$20 \cdot 10^{-3}$
1.63	2.2	$2.6 \cdot 10^{-2}$	$19 \cdot 10^{-3}$
2.2	6.3	$9.2 \cdot 10^{-2}$	$9.1 \cdot 10^{-3}$
3.2	≥ 4.3	$\leq 1.3 \cdot 10^{-2}$	$\leq 19 \cdot 10^{-3}$
10	≥ 17	$\leq 3.4 \cdot 10^{-3}$	$\leq 15 \cdot 10^{-3}$
21	≥ 17	$\leq 3.4 \cdot 10^{-3}$	$\leq 31 \cdot 10^{-3}$
22	≥ 130	$\leq 4.5 \cdot 10^{-4}$	$\leq 4.5 \cdot 10^{-3}$

TABLE VI

Substance	Wavelength in cm				
	300	100	10	3	1.2
Fused quartz	10^{-4}		$0.6 \cdot 10^{-4}$	10^{-4}	$2.5 \cdot 10^{-4}$
Muscovite	$2 \cdot 10^{-4}$		$3 \cdot 10^{-4}$		
Sandy soil dry		10^{-2}	$6 \cdot 10^{-3}$	$4 \cdot 10^{-3}$	
Clay soil dry		$2.0 \cdot 10^{-2}$	$1.5 \cdot 10^{-2}$	$1.3 \cdot 10^{-2}$	
Soda-silica glasses		10^{-2}		$2.3 \cdot 10^{-2}$	
Al-Mg silicates	$3-30 \cdot 10^{-4}$		$6-50 \cdot 10^{-4}$		

The values of $\tan \Delta$ for Model II in Table V are similar to those of common substances while those for Model I in Table IV are several times larger than the highest values of $\tan \Delta$ in Table VI. Any model assuming lower values of the thermal conductivity than $2.5 \times 10^{-6} \text{ cal cm}^{-1} \text{ sec}^{-1} \text{ } ^\circ\text{K}^{-1}$ would require even larger values of $\tan \Delta$ which would be scarcely acceptable.

Unlike the values of $\tan \Delta$ in Table VI, which show only a slow variation with wave-length, the computed values for Models I and II vary very rapidly with wave-length at wave-lengths in the neighbourhood of 1 cm. If this feature is regarded as real, then the electrical conductivity actually increases with

wave-length in the range $\lambda < 1.25$ cm. At wave-lengths greater than 1.25 cm, $\tan \Delta$ shows a steady decrease with increasing wave-length.

The calculation of the penetration depth, $1/\alpha$, at 168 cm wave-length depends on the behaviour of $\tan \Delta$ at longer wave-lengths than are included in Tables IV and V, but a safe lower limit to $1/\alpha$ is obtained by assuming $\tan \Delta$ to remain constant in the range $22 \text{ cm} < \lambda < 168 \text{ cm}$. The penetration depths for the two models are then:

$$\text{Model I} \quad (1/\alpha)_{168 \text{ cm}} > 26 \text{ metres,}$$

$$\text{Model II} \quad (1/\alpha)_{168 \text{ cm}} > 168 \text{ metres.}$$

Models in which both the thermal and electrical conductivities vary with depth present a very large number of possibilities and we shall consider only one type of model which seems physically the most probable.

Model III: the composition of the surface is supposed constant with depth but the packing of the material increases downwards due to the pressure of the overlying material. Thus k may increase from about $2.5 \times 10^{-6} \text{ cal cm}^{-1} \text{ sec}^{-1} \text{ }^\circ\text{K}^{-1}$ at the surface to as much as $4 \times 10^{-3} \text{ cal cm}^{-1} \text{ sec}^{-1} \text{ }^\circ\text{K}^{-1}$ when solid rock is reached. The electrical conductivity on the other hand would be expected to increase by a factor only of the order of 2, depending on the relative density of the loose surface material and the solid rock. Using the relations for a homogeneous model from Section 3,

$$\delta = \beta/\alpha = \frac{1}{2\pi} (\omega s/2)^{1/2} \frac{(\rho\epsilon)^{1/2}}{\tan \Delta} k^{-1/2} \lambda.$$

For a homogeneous model, $\delta \propto \lambda$ if $\tan \Delta$ is constant. For the type of model considered here, the factor $\rho^{1/2}\epsilon^{1/2}/\tan \Delta$ will vary but little with depth. At the shorter wave-lengths the low value of k at the surface is the relevant one, whilst at the longer wave-lengths which penetrate more deeply the effective value of k is much larger. Thus the apparent value of δ should increase with wave-length more slowly than $\lambda^{1.0}$. In fact, for $\lambda > 1.25$ cm, the observations show an increase of δ faster than $\lambda^{1.0}$. To account for the observations satisfactorily, $\tan \Delta$ must decrease with increasing wave-length and there cannot be any significant increase of k with depth in the range $(1/\alpha)_{1.25 \text{ cm}}$ to $(1/\alpha)_{22 \text{ cm}}$. Below this latter depth we have no information regarding the value of k .

6. *The steady temperature T_0 .*—Piddington and Minnett's and Jaeger's treatments of the lunar temperature considered the solar flux as the only source of heat and thus the mean temperature, T_0 , should be the same at all depths in the lunar surface. A steady outward flow of heat, Q , due to radioactivity in the Moon, or a possible initial high temperature at the time of the Moon's formation would give rise to a temperature gradient $Q/k \text{ }^\circ\text{K cm}^{-1}$ at the surface and the apparent lunar temperature at a wave-length where the penetration depth is $1/\alpha$ would be

$$T_{x=0} + \int_0^\infty \frac{Qx \exp(-\alpha x) dx}{k}.$$

If α and k are independent of depth this becomes

$$T_{x=0} + Q/k\alpha.$$

We may now examine the observations to find any possible variation of T_0 with wave-length and to check the values against the theoretical ones of Jaeger.

The spread of results in Table III reflects the poor accuracy of the calibrations of many of the observations. The value of T_0 at 168 cm lies about 10°K below the mean of all the other observations, and thus there is at present no observational evidence to suggest that the mean temperature at 168 cm is systematically higher than at short wave-lengths.

The values of T_0 in Jaeger's models quoted in Table II range from 210 – 238°K . Lower values of T_0 could be expected only by assuming the surface layers to have a thermal conductivity $< 2.5 \times 10^{-6} \text{ cal cm}^{-1} \text{ sec}^{-1} \text{ }^\circ\text{K}^{-1}$. This is lower than that measured for dust *in vacuo* and would also lead to improbably large values of $\tan \Delta$ to explain the centrimetric observations. Values of T_0 higher than 238°K would require a comparatively large value of k immediately below the surface layer which Jaeger showed to be incompatible with the eclipse observations in the infra-red (Pettit (7)). He found that the model fitting Pettit's results best was one in which a thin layer of dust lay on top of a gravelly base (corresponding to the third model in Table II). The mean temperature of this model is 222°K . We may therefore conclude that the observed value of T_0 at 168 cm does not differ from the mean surface temperature by more than 25°K . Then

$$Q/k\alpha \leq 25^\circ\text{K}.$$

For Model I

$$Q \leq 2.5 \times 10^{-8} \text{ cal cm}^{-2} \text{ sec}^{-1},$$

and for Model II

$$Q \leq 2.5 \times 10^{-7} \text{ cal cm}^{-2} \text{ sec}^{-1}.$$

Most models of type III, in which a layer of dust overlies a gravelly base, give intermediate values for the upper limit to Q . If, however, the thermal conductivity increases suddenly at depths just below $(1/\alpha)_{22} \text{ cm}$ to a large value (such as would be the case if solid rock were reached at this depth) the value of T_0 at 168 cm would be approximately $T_{x=0} + Q/k\alpha_{22} \text{ cm}$ and the upper limits to Q would be relaxed to give $Q \leq 1.7 \times 10^{-7} \text{ cal cm}^{-2} \text{ sec}^{-1}$ for fine dust lying on top of the rock, and $Q \leq 17 \times 10^{-7} \text{ cal cm}^{-2} \text{ sec}^{-1}$ for gravel lying on top of the solid rock.

The steady heat flow through the surface for a Moon of chondritic composition has been estimated by Jaeger (23) as $2.3 \times 10^{-7} \text{ cal cm}^{-2} \text{ sec}^{-1}$ and more detailed calculations by MacDonald (24) gave values of $2.4 \times 10^{-7} \text{ cal cm}^{-2} \text{ sec}^{-1}$ for an initially cold Moon formed 4.5×10^9 years ago and $2.9 \times 10^{-7} \text{ cal cm}^{-2} \text{ sec}^{-1}$ for a Moon having an initial temperature of 600°C .

The upper limit on Q for Model I is only a tenth of the expected heat flow. This fact, together with the very large derived values of $\tan \Delta$, make this model unacceptable. A model of the lunar surface of the type proposed by Gold (25) in which large areas are deeply covered in dust can only be made to fit the observations if the pressure some distance below the surface increases the thermal conductivity by at least one order of magnitude. It seems doubtful if such a picture would then be consistent with the apparent variation of temperature through the lunar cycle discussed in Section 5.

7. *Conclusions.*—(i) An accurate measurement of the mean disk temperature of the Moon of $233^\circ \pm 8^\circ\text{K}$ has been obtained at the lowest frequency which has so far been used in such measurements.

(ii) A model of the surface consisting of fine dust of very low thermal conductivity extending to great depths seems unsatisfactory.

(iii) The absence, at 22 cm wave-length, of any detectable variation of temperature through the lunar cycle indicates that gravely material extends to depths of at least $(1/\alpha)_{22\text{ cm}} = 20$ metres.

(iv) For models which fit the centimetric observations best the observation at 168 cm provides an upper limit to the heat flow through the surface which is very close to that expected for a Moon of chondritic composition.

To extend this investigation three types of observation are now needed.

(i) Eclipse observations at the shorter wave-lengths to determine more precisely the appropriate model of the outermost layers which largely determine the mean surface temperature.

(ii) Observations in the range 3–21 cm designed to detect any variation with the lunar cycle, preferably by comparison of the brightness temperatures of the two halves of the lunar disk.

(iii) An investigation of the dielectric properties of stony meteorites in the radio-frequency range.

Acknowledgments.—I should like to thank Professor M. Ryle for a very useful discussion of the observations, and A. J. Turtle who has computed the accurate values of sky temperature used in the derivation of the lunar temperature.

Mullard Radio Astronomy Observatory,
Cavendish Laboratory,
Cambridge:

1961 April.

References

- (1) M. Ryle, *J.I.E.E.*, **6**, 14, 1960.
- (2) C. H. Costain, *M.N.*, **120**, 248, 1960.
- (3) R. D. Davies and R. C. Jennison, *Observatory*, **80**, 73, 1960.
- (4) J. D. Evans, *The scattering properties of the lunar surface at radio wavelengths*, M.I.T. Lincoln Laboratory Report, 1961.
- (5) A. J. Wesselink, *B.A.N.*, **10**, 351, 1948.
- (6) J. C. Jaeger, *Aust. J. Phys.*, **6**, 10, 1953.
- (7) E. Pettit, *Ap. J.*, **91**, 408, 1940.
- (8) J. H. Piddington and H. C. Minnett, *Aust. J. Phys.*, **2**, 63, 1949.
- (9) W. C. Tyler, R. N. Whitehurst and F. H. Mitchell, *Bull. Am. Phys. Soc.*, **II**, **3**, 301, 1958.
- (10) A. E. Salomonovich, *Ast. J.U.S.S.R.*, **35**, 129, 1958.
- (11) J. E. Gibson, *Proc. I.R.E.*, **46**, 280, 1958.
- (12) M. R. Zelinskaya, V. S. Troitskii and L. I. Fedoseev, *Ast. J.U.S.S.R.*, **36**, 643, 1959.
- (13) C. J. Grebenkemper, U.S. National Committee Report to U.R.S.I., XIII General Assembly, 1960, p. 215.
- (14) V. S. Troitskii and M. R. Zelinskaya, *Ast. J.U.S.S.R.*, **32**, 550, 1955.
- (15) J. P. Castelli, C. P. Ferioli and J. Aarons, *A.J.*, **65**, 485, 1960.
- (16) K. Akabane, *Proc. Jap. Acad.*, **31**, 161, 1955.
- (17) P. G. Mezger and H. Strassl, *Plan. Spa. Sci.*, **1**, 213, 1959.
- (18) J. A. Waak, *A.J.*, **65**, 565, 1960.
- (19) G. Westerhout, *B.A.N.*, **14**, 215, 1958.
- (20) C. L. Seeger, G. Westerhout and R. G. Conway, *Ap. J.*, **126**, 585, 1957.
- (21) A. R. von Hippel (Ed.), *Dielectric Materials and Applications*, Wiley, New York, 1954.
- (22) H. C. Urey and H. Craig, *Geochim. et Cosmochim. Acta*, **4**, 36, 1953.
- (23) J. C. Jaeger, *Nature*, **183**, 1316, 1959.
- (24) G. J. F. MacDonald, *J. Geophys. Res.*, **64**, 1967, 1959.
- (25) T. Gold, *M.N.*, **115**, 585, 1955.
- (26) W. M. Sinton, *Ap. J.*, **123**, 325, 1956.

ON THE CENTRE-LIMB VARIATION OF GRANULE CONTRAST

R. G. Giovanelli

(Received 1961 April 17)

Summary

It is shown that the observed centre-limb changes in granule contrast, and particularly the disappearance of granulation near the limb, are due mainly to foreshortening and finite telescope resolution. Without greatly improved resolution, it is invalid to use such observations for inferring the optical depth of the top of the granulation zone, as has sometimes been done.

1. *Introduction.*—A number of recent papers (Rösch 1957, Edmonds 1960, Loughhead and Bray 1960) have discussed the appearance of granulation near the Sun's limb. The significance of the results has been in their implication as to the structure of the convection zone, at the top of which the granules apparently lie. Using a model in which the granules are supposed covered by a thin layer of optical depth τ , which reduces the granule contrast progressively from centre to limb, Plaskett (1955) related τ to θ , the angle from the centre of the Sun at which granulation disappears (i.e. the contrast falls below some arbitrary level). Waldmeier (1939) and ten Bruggencate (1939) observed θ to be 70° and 72° respectively, corresponding to which Plaskett inferred $\tau = 1.2$. Edmonds (1960) also found a rather similar result, about 75° , though he points out that a larger-scale lower-contrast pattern of brightness fluctuations seems to extend to $\theta = 86^\circ$ or more. On the other hand, Rösch (1957) considered the granules to be visible to about 82° – 85° , a result with which Loughhead and Bray (1960) are in agreement; de Jager (1959) puts the corresponding optical depth $\tau = 0.1$.

In the various discussions of these observations, no account has been taken of the contrast transfer functions (frequency responses) of the telescopes used. While the contrasts of very coarse structures are faithfully reproduced, they are reduced for finer structures, reaching zero at the resolution limit. Hence foreshortening must cause substantial reduction in the observed contrast towards the limb. The question arises as to whether this is a significant factor in the observations. As will be shown, instrumental effects have almost entirely dictated the results in all observations made to date.

2. *The contrast transfer function.*—For simplicity I shall use the contrast transfer function for a one-dimensional structure; this describes the contrast with which the optical system reproduces each of the various Fourier components in the object. Though granulation has a variation in two dimensions across the surface, it is sufficient for the present discussion to consider radial variations alone and to represent the granulation by a sinusoidal structure whose period corresponds to the granule diameter.

The contrast transfer function of an aberration-free objective may be written (e.g. Steel 1953a)

$$T(m) = \begin{cases} \frac{2}{\pi} [\cos^{-1} m - m(1-m^2)^{1/2}], & (m < 1) \\ 0 & (m > 1) \end{cases} \quad (2.1)$$

where $m = \lambda/D\phi$, λ being the wave-length of light, D the diameter of the objective and ϕ the angular size corresponding to the spatial period. The function $T(m)$ has been tabulated by Steel (1953b). A one-dimensional sinusoidal structure (parallel to the limb) which would have angular size ϕ_0 at the centre of the disk is foreshortened at θ to

$$\phi = \phi_0 \cos \theta.$$

Fig. 1 shows the relative contrast of this structure (the relevant value of $T(m)$) as a function of θ and of $m_0^{-1} = \phi_0 D/\lambda$. As guide, the values of ϕ_0 corresponding to those of m_0^{-1} in Fig. 1 are given in Table I for $\lambda = 5.5 \times 10^{-5}$ cm and for diameters of the telescopes used by some of the authors.

TABLE I
Relationship between m_0 (Fig. 1) and ϕ_0

	m_0^{-1}							
	1.5	2	3	5	10	15	20	30
D (cm)	Corresponding ϕ_0 (sec of arc)							
12.5	1.36	1.8	2.7	4.5	9.1	13.6	18.2	27.3
23	0.74	1.0	1.5	2.5	5.0	7.4	9.9	14.8
30	0.57	0.76	1.14	1.9	3.7	5.7	7.6	11.4

Real telescopes are never aberration-free, while the solar image is also affected by atmospheric seeing. Aberrations do not influence the values of $T(m)$ near $m=0$ (very coarse patterns) or very near the limit of resolution, but cause a general lowering of $T(m)$ for intermediate frequencies, or even a reversal of contrast for some frequencies in extreme cases; Blackwell, Dewhurst and Dollfus (1959) give the measured contrast transfer function of one telescope. The biggest reduction in $T(m)$ is usually at about half the resolution limit. The effect of aberrations would be to lower all the curves in the central range of contrasts in Fig. 1.

3. *Discussion.*—Lacking knowledge of the actual frequency responses of the various telescopes, I shall use Fig. 1 for discussion purposes.

The diameters of photospheric granules generally lie in the range $1''$ – $2''$. For the largest of these ($\phi_0 = 2''$), observed with a 12.5 cm aperture telescope such as that of Loughhead and Bray, $m_0^{-1} = 2.2$. From Fig. 1, the contrast has dropped almost to zero by $\theta = 60^\circ$, beyond which such granules are below the limit of resolution. For Rösche's and Edmonds' telescopes (apertures 23 cm and 30 cm) the corresponding values of θ are about 72° and 75° respectively. These conclusions are very little influenced by the use of a one-dimensional rather than a two-dimensional analysis. Edmonds' observed values agree remarkably well with expectation, but the structures observed by Rösche and by Loughhead and Bray extend far too close to the limb to be ordinary granules.

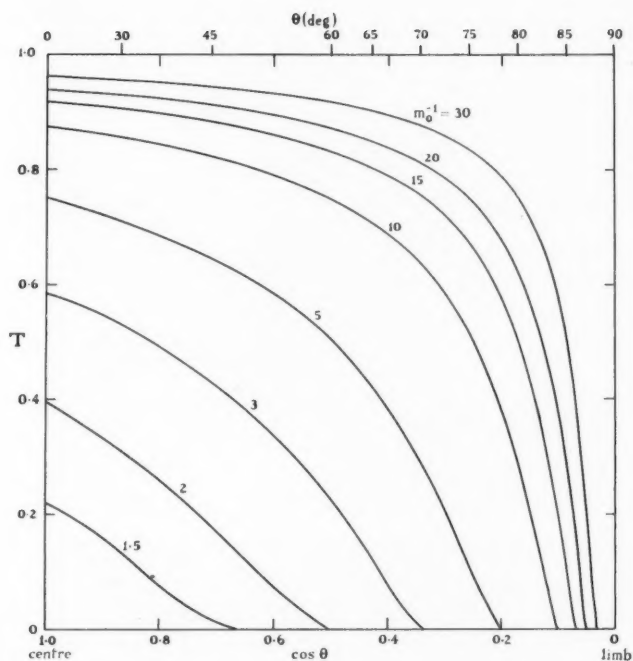
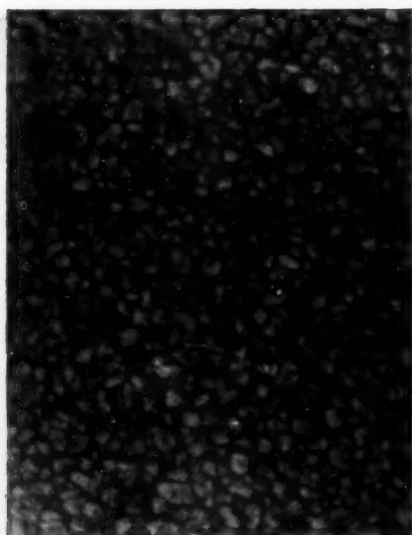
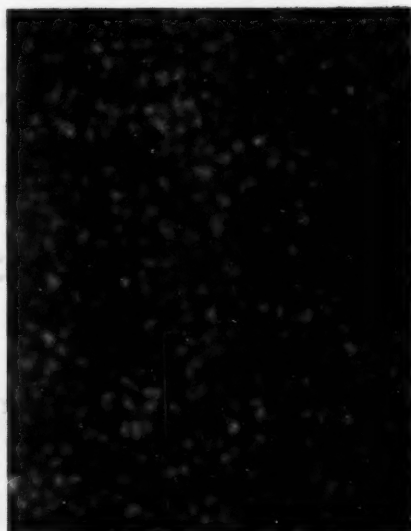


FIG. 1.—Variation in contrast transfer factor T due to foreshortening of a sinusoidal object at angular distance θ from the centre of the disk, a single element subtending angle ϕ_0 when at the centre of the disk. The curves are for various values of $m_0^{-1} = \phi_0 D / \lambda$, D being the telescope diameter.

(a)

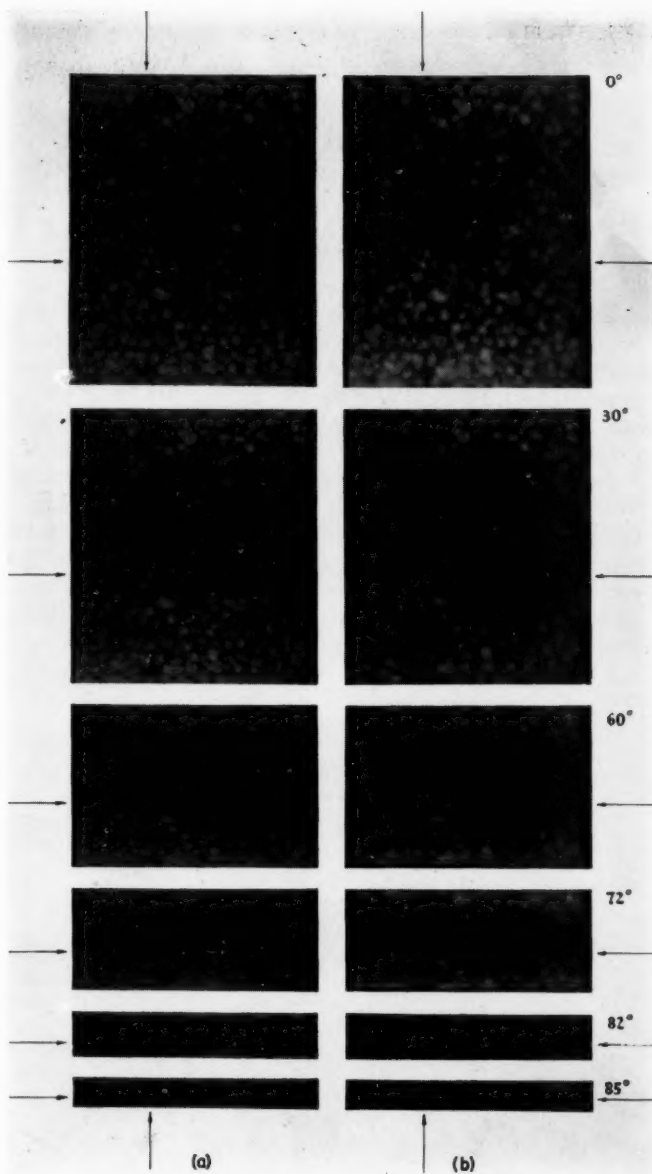


(b)



- (a) Photospheric granulation photographed by Schwarzschild: telescope aperture 30 cm.
(b) Photospheric granulation photographed by Loughhead and Bray: telescope aperture 12.5 cm.

R. G. Giovanelli, On the centre-limb variation of granule contrast



Photographs of Plate 9 (a) simulating observations of granulation through telescopes of apertures 23 cm (a) and 12.5 cm (b). The direction of view varies from the normal as marked, showing the variation in appearance of granulation from centre (top) to near the limb (bottom) due solely to finite telescope resolution. The photographic processing of all the prints within either set (a) or set (b) is identical, but set (b) has been printed on paper more contrast than set (a).

R. G. Giovanelli, On the centre-limb variation of granule contrast

It is possible to understand the various observations better by making use of a very simple demonstration. Plate 9(a) is a photograph of the photosphere obtained at a high altitude by Schwarzschild with a 30 cm telescope. This has been rephotographed at various angles to the normal, at such distances and apertures as to simulate the centre-limb variation in granulation as viewed through a 23 cm aperture telescope (Plate 10(a)) and one of 12.5 cm aperture (Plate 10(b)). The contrasts of the finer structures must be somewhat lowered in the course of this processing. However, the upper photograph of Plate 10(b) closely resembles the direct photograph of the centre of the disk, Plate 9(b) obtained by Loughhead and Bray with a 12.5 cm aperture telescope.

The general superiority of the larger over the smaller aperture is at once apparent, as is the rapid decrease in contrast towards the "limb" in both cases. The numbers of granules visible also decrease rapidly towards the "limb", groups of granules well defined at the centre of the disk merging into one apparent granule when foreshortened. A good example can be seen by noting the bright granules at the intersection of the arrows in Plate 10. Just where granulation "disappears" will obviously depend greatly on the criterion used by the individual observer; as pointed out by Edmonds, larger-scale brightness fluctuations, or rather groups of brighter granules, can still be detected when the individual granules are no longer resolved.

It is clearly inadmissible to use the disappearance of granulation towards the limb for an analysis of the optical thickness of any layer above the convection zone, without much higher resolving powers than have been available hitherto; or alternatively without a very much more sophisticated analysis of the variation in contrast with θ . An adequate analysis seems in any case impracticable without much higher resolution. The most that can be said at present is that any such layer cannot have an optical thickness exceeding about 1.2; it may very well be negligible.

Division of Physics,
Commonwealth Scientific and Industrial Research Organization,
Sydney:
1961 April.

References

- D. E. Blackwell, D. W. Dewhurst and A. Dollfus, 1959, *M.N.*, **119**, 98.
C. de Jager, 1959, *Handbuch der Physik*, Vol. 52, p. 83 (Springer: Berlin).
F. N. Edmonds, 1960, *Ap. J.*, **131**, 57.
R. E. Loughhead and R. J. Bray, 1960, *Aust. J. Phys.*, **13**, 738.
H. H. Plaskett, 1955, "Vistas in Astronomy", Vol. 1, p. 646 (Pergamon: London).
J. Rösch, 1957, *Astronomie*, **71**, 138.
W. H. Steel, 1953a, *Rev. d'Optique*, **32**, 4 (see p. 20).
W. H. Steel, 1953b, *Rev. d'Optique*, **32**, 143 (see Table XI).
P. ten Bruggencate, 1939, *Zeits. f. Astrophys.*, **19**, 59.
M. Waldmeier, 1939, *Helv. Phys. Acta*, **13**, 14.

a
7
C
V
2
S
a
e
ic
s
it
V
p
a

p
i
w
of

THE POSSIBILITY OF OBSERVING FEATURES OF GALACTIC RADIO EMISSION FROM A SATELLITE-BORNE RADIO TELESCOPE

F. G. Smith

(Received 1961 April 26)

Summary

It has already been proposed to extend measurements of the spectrum of radio emission from the galaxy to frequencies of about 1 Mc/s by means of a satellite-borne receiver. If the satellite is in the upper ionosphere, where the refractive index is increasing with height, a focusing effect will occur which may allow individual features of emission to be observed. It is shown that a beamwidth of the order of 20° may be achieved under favourable circumstances; the most important limitation is the frequency bandwidth necessary in a sufficiently sensitive receiver, which inevitably means that dispersion in the refractive index effectively blurs out any narrower beam or any interference effects inside the beam.

The experimental conditions needed for the realization of this degree of focusing in a satellite or a rocket flight are discussed. It appears that the frequency of a satellite-borne receiver should sweep over a range of about 3 to 5 Mc/s, with a bandwidth of 10 kc/s. The satellite orbit should be nearly circular, at a height of about 400–500 km.

1. *Introduction.*—Although theories of the galactic radio emission which attribute it to synchrotron radiation from relativistic electrons (Shklovsky 1952, Tunmer 1959, Hoyle 1960) show that the radio spectrum is not far from that derived from the cosmic-ray energy spectrum, there remains a discrepancy which is hard to explain. Briefly, it is expected that in the frequency range 20–400 Mc/s over which accurate measurements have been made the radio spectral index should be near -1.0 , whereas the best radio measurements give an index of -0.37 ± 0.04 (Costain 1960). A low index would only in fact be expected at lower frequencies, where the electrons lose energy primarily by ionization rather than by the synchrotron emission itself. Observations do not so far give any evidence of a change in spectral index with frequency, although it seems likely that an extension of the frequency range will show such a change. With observations available over an extended range of frequency it may become possible to revise the theory, and learn more about the processes of energy gain and loss in the cosmic-ray electrons.

It is already proposed to extend observations below the frequency limit at present set by the ionosphere, by mounting a receiver for frequencies around 1 Mc/s in a Scout satellite. A dipole aerial of about 150 ft overall will be used, with a receiver of about 20 kc/s bandwidth sweeping over a frequency range of about $\frac{1}{2}$ to 3 Mc/s. No angular resolution is required for the purposes of this

experiment, which is intended only to provide a measure of the average brightness of one hemisphere of sky at any one time. However, there are several individual features of the galactic emission which deserve study with a finer angular resolution, and a beamwidth of the order of 10° – 30° would be very valuable for this. With such a beam it would be possible for example to delineate the extent of absorption by H II near the galactic plane, or to obtain a rough comparison of the spectra of such features as the spur of emission at $l^\text{II} = 0$.

Such a beamwidth is impossible to obtain by ordinary means when the wave-length is of the order of 300 metres, but it will be shown that the focusing effect found in the upper ionosphere may provide such a beamwidth. It is likely, in fact, that this focusing effect will be observed to some extent in the Scout experiment, since the technique of frequency-sweeping is the most likely way of demonstrating it.

This paper analyses the conditions under which focusing may be observed from satellites and from rockets. Observations of focusing are restricted by the complications of magneto-ionic splitting, ionospheric irregularities, and the extremely dispersive nature of the refractive index, but the practical examples show that a beamwidth of about 20° may be obtained.

2. *The focusing effect.*—Ignoring for the moment the effects of the terrestrial magnetic field, we consider the upper ionosphere as a smooth horizontally stratified medium in which the refractive index increases smoothly from zero to unity in a height of some hundreds of kilometres. Rays to a receiver at a height

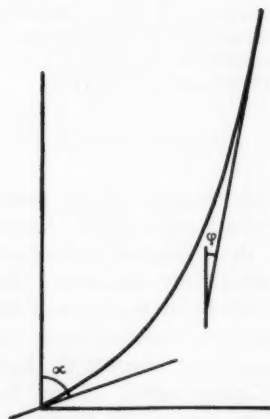


FIG. 1.—Ray path from satellite in the ionosphere.

where $\mu = \mu_0$, received with an intensity $I(\alpha)$ in a direction α , may be traced back through the ionosphere until they emerge at an angle ϕ to the vertical (Fig. 1), where:

$$\sin \phi = \mu_0 \sin \alpha.$$

The maximum value of ϕ is given by $\sin \phi_0 = \mu_0$. All rays are contained in a cone of semi-angle ϕ_0 , so that a restricted aerial beam is obtained like that from mounting a dipole over a reflecting surface. The intensity $I(\phi)$ in direction ϕ is related to $I(\alpha)$ by:

$$I(\phi) \sin \phi d\phi = I(\alpha) \sin \alpha d\alpha$$

so that we may obtain the gain over an isotropic receiving aerial in direction ϕ :

$$I(\phi) = \frac{1}{\mu_0^2} \frac{\cos \phi}{\left(1 - \frac{\sin^2 \phi}{\mu_0^2}\right)^{1/2}}.$$

Here we have put $I(\alpha) = 1$, although practical aerials will depart somewhat from an isotropic sensitivity. The forward gain, at $\phi = 0$, is seen to be $1/\mu_0^2$ and the gain increases towards infinity at $\phi = \phi_0$, where there is a cusp of rays corresponding to values of α near 90° . Fig. 2 shows a plot of the polar diagram $I(\phi)$ for $\mu_0 = 0.2$.

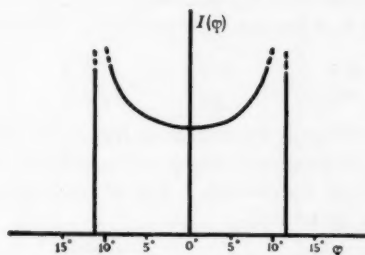


FIG. 2.—Polar diagram $I(\phi)$ deduced from geometrical refraction.

This simple picture of refraction suggests that narrow beamwidths can be obtained with a loop aerial system no more elaborate than a single dipole or loop. Subsequent analysis must take account of interference effects in this refraction, and of the effects of the Earth's magnetic field. The ionosphere may be irregular, as is suggested by observations of the scintillation of radio stars; this may set a limit on the useful gain to be obtained. The choice of frequency must be considered carefully, since the refractive index changes very rapidly with frequency when it approaches zero. Finally, it may be difficult to attain the necessary sensitivity in the receiver, so that the choice of aerial system must be considered.

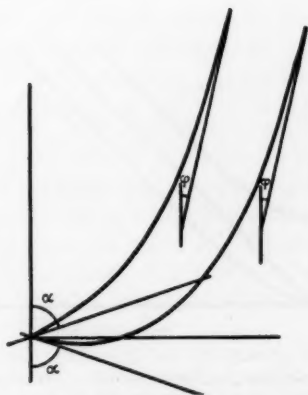


FIG. 3.—The two ray paths from the satellite.

3. *Interference effects.*—Using the simple model of the ionosphere it appears that for each angle of emergence ϕ there are two rays of equal intensity at the satellite, symmetrically disposed about the horizontal (Fig. 3).

The path difference evidently depends on the form of variation of μ with height, but the general effect is to provide a system of Airy fringes across the polar diagram. At the centre the order of the fringes may be quite low. For an ionosphere whose electron density varies as e^{-h/h_0} , it may be shown that the order n_0 at the centre is

$$n_0 = \frac{4h_0\mu_0^3}{\lambda_0} \left[\frac{1}{3} + \frac{\mu_0^2}{5} + \dots \right]$$

where μ_0 is the refractive index at the satellite, and λ_0 is the free space wave-length.

For example, taking $h_0 = 100$ km, $\lambda_0 = 300$ m we find values for n_0 as follows:

μ_0	0.1	0.2	0.3	0.4
n_0	0.45	3.5	12	120.

However, since μ_0 is critically dependent on frequency, the order of interference will change so rapidly with frequency that it will be difficult to observe interference with a reasonable receiver bandwidth. For a small change in frequency Δf we have a change in n_0 given by:

$$\frac{\Delta n_0}{n_0} = \frac{3\Delta\mu_0}{\mu_0} = 3 \frac{1 - \mu_0^2}{\mu_0^2} \frac{\Delta f}{f}$$

and, for example, if $\mu_0 = 0.2$ a $\frac{1}{2}$ per cent in frequency gives a change $\Delta n_0 \approx 1$.

Interference effects of this nature will not be considered further in this paper. A more detailed analysis of similar effects has been made by Haselgrove, Haselgrove and Jennison (1961), and by Budden (1961).

4. *The effect of the Earth's magnetic field.*—In the upper *F*-region the collisional frequency is low, and absorption effects may be neglected. The main complication in comparing the simple model with the actual ionosphere is therefore the Earth's magnetic field. The refractive index is now different for the two characteristic modes of propagation, and for different directions of propagation. Fig. 4 shows the conditions under which refractive index is zero for propagation in directions

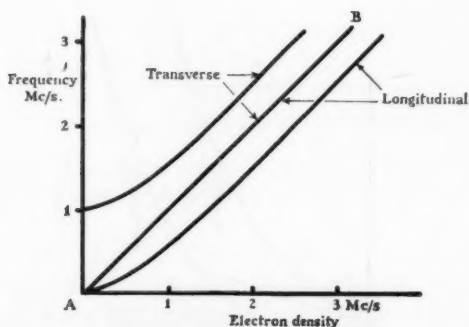


FIG. 4.—Magneto-ionic splitting of refractive index. The graph shows the frequency where $\mu = 0$ at various electron densities (expressed as plasma frequencies f_p) for longitudinal and transverse propagation.

longitudinal and transverse to the magnetic field, for a gyrofrequency of 1 Mc/s ($H=0.36$ gauss).

It will be seen that, at a fixed electron density, for all frequencies above a value f_1 on the line AB the refractive index is greater than zero, while at this frequency f_1 it is zero for all directions of propagation. This refers to the extraordinary mode of propagation; the refractive index for the ordinary mode remains positive at the frequency f_1 . The change in the refractive index for the extraordinary mode for frequencies slightly above f_1 is illustrated in Fig. 5 for the conditions $f_H=1$ Mc/s, $f_p=1$ Mc/s (Fig. 5(a)) and for $f_H=1$ Mc/s, $f_p=3$ Mc/s (Fig. 5(b)).

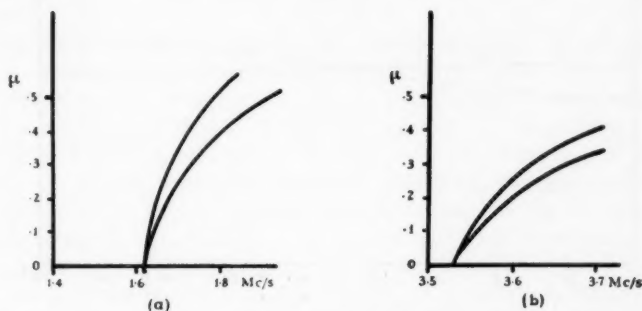


FIG. 5.—Refractive index near zero. (a) $f_H=1$ Mc/s, $f_p=1$ Mc/s; (b) $f_H=1$ Mc/s, $f_p=3$ Mc/s. Upper curves refer to transverse, lower to longitudinal, propagation.

It will be noted that the change in μ with frequency is very rapid near the critical frequency, and also that above this frequency μ is dependent on the direction of propagation. If for example it were required to place a receiver where $\mu=0.2$ in the situation of Fig. 5(a), the frequency could be adjusted so that μ lay in the range 0.15 to 0.25 according to direction ($f=1.63$ Mc/s), but a receiver bandwidth of 10 kc/s would further widen this range to, say, 0.15 to 0.30. At the higher frequencies of Fig. 5(b) the situation is easier, with splitting between 0.20 and 0.26, widening to between 0.20 and 0.28 for a bandwidth of 10 kc/s.

Splitting of μ according to azimuth affects the shape of the beam in a way which depends on the inclination of the magnetic field. An example has been calculated by N. Capon, of the Cambridge University Mathematical Laboratory, for conditions where the inclination is high, giving only a small distortion of the beam. The model used for the ionosphere had a penetration frequency of 6 Mc/s, and the observing frequency was 3.6 Mc/s. To obtain a refractive index $\mu_0=0.2$, the receiver was considered to be 270 km above the maximum, where the electron density was decreasing roughly exponentially with a scale height of 70 km. The magnetic field was taken as a dipole field, and allowance was made for the curvature of the Earth. Fig. 6 shows the results of ray tracing for a position over southern England (magnetic latitude 55°). It is seen that the distortion of the beam is not serious.

5. *Irregularities.*—Local variations of refractive index are known to exist in the upper *F*-region. The condition of ionospheric echoes known as "Spread-F" indicates that the variations of density may often exceed

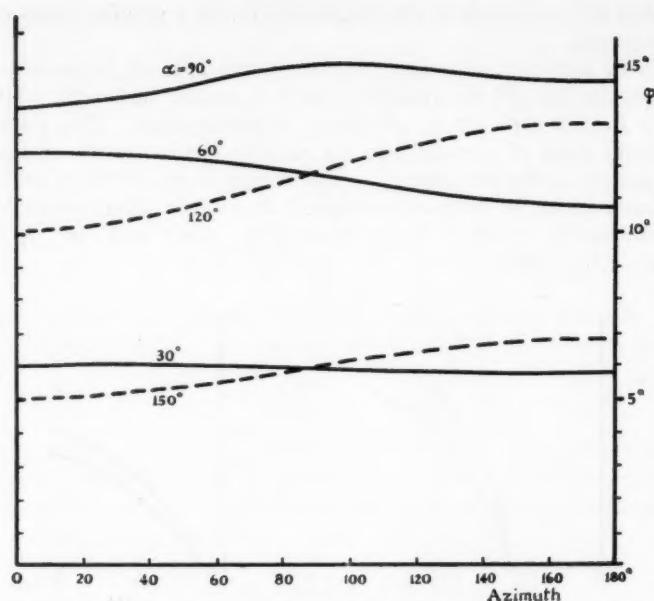


FIG. 6.—Angles of emergence ϕ for rays leaving a satellite at various elevations α for azimuthal directions. Observing frequency 3.6 Mc/s, scale height 70 km. Magnetic latitude 55° .

one-tenth of the mean density. However, this condition is generally only observed at night time, and is even then rare in geomagnetic latitudes between about 15° and 45° . Clear *F*-region echoes correspond to less than 1 per cent variation of density; we may reasonably expect that less than 2 per cent variations usually occur. For $\mu_0 = 0.2$, this corresponds to a variation of about 0.05 in the value of μ_0 .

6. *Practical limits of focusing.*—The detection of galactic radio noise at these low frequencies with simple receivers suitable for mounting in satellites demands the use of appreciable bandwidths. Both from convenience in construction and from the necessary smoothing of the noise output when a short output time constant must be employed, it seems reasonable to take 10 kc/s as a typical bandwidth. From Section 4 we see that at 1 Mc/s this places a lower limit at $\mu_0 = 0.2$ for useful focusing, where the frequency bandwidth together with the magneto-ionic splitting provides a maximum range of μ_0 between 0.15 and 0.30 according to direction. At 3 Mc/s the same bandwidth may be used to provide a maximum range of μ_0 between 0.09 and 0.17 or between 0.20 and 0.28. Clearly focusing may be achieved only down to $\mu_0 \approx 0.15$ or 0.2, the changes being better at higher frequencies, and at high geomagnetic latitudes. This limitation is in any case close to the limit set by our present knowledge of irregularities of electron density.

The forward gain, from Section 2, is 25 for $\mu_0 = 0.2$ and 100 for $\mu_0 = 0.1$. The increased gain at the edges of the beam will not be realized because of the variations of μ_0 with ray direction and because of the necessary frequency

bandwidth, nor for the same reasons can interference effects be expected. However, a directivity of this order will be of considerable use in the exploration of the galactic background, even though the actual value of the gain may be in doubt under practical conditions.

7. *Observational methods.* (i) *Rockets.*—It might be possible to observe a focusing effect during the short duration of a rocket flight, but the chances of success depend on the smoothness of the ionosphere at the place and time of launch. Since a rocket traverses the ionosphere rapidly, little will be gained by sweeping the frequency of the receiver, and it would be best to use several narrow band receivers at separated frequencies, all connected to the same aerial. At each frequency there will be two opportunities of observation, during ascent and descent.

(ii) *Satellites.*—A satellite, placed in a nearly circular orbit at a height of about 400–500 km, would be in a suitable part of the ionosphere for much of its orbit. A sweep in frequency over say 2–5 Mc/s, each sweep lasting about 1 minute, would require data to be telemetered at a rate of about 10 numbers per second, each with an accuracy of about 5 per cent. This is well within the capabilities of typical telemetry systems. Allowing for the difficulties of monitoring and recording the telemetry transmission, and for the incidence of ionospheric irregularities over as much as half the orbit, there should still be about 20 good observations of focusing each day, and a few weeks of observation should cover most of the sky with a 20° beam. A narrower beam might prove possible for some parts of the sky, but it is unlikely that many observations will be possible at a width of 10° .

(iii) *Aerial systems.*—Bearing in mind the need for simplicity in satellite equipment, it is reasonable to specify that a suitable aerial system must provide a signal considerably larger than receiver input noise. An electric dipole can be extended to an overall length of 100 ft, either by the extension of flexible metal strip or by the release of a thin wire under centrifugal force, and such an aerial can produce a signal more than ten times receiver noise even when very broadly tuned. The impedance of the dipole will change when it is immersed in the ionosphere, but this is of no consequence under the conditions required for focusing.

A magnetic loop, using a ferrite rod of several pounds weight, can also be used at frequencies of about 3–5 Mc/s to produce a signal several times receiver noise. It is, however, now necessary to tune to the aerial with a narrow-band circuit, and the receiver will consequently be more complicated. It is also necessary to take into account the variation of inductance of the loop with temperature, although there is no effect due to the ionosphere itself.

In either case the measured field will be inversely proportional to the square root of the refractive index. Interpretation of the records will therefore require a knowledge of μ_0 . A value of μ_0 should be obtainable from the record of the frequency sweep of the receiver, since a sudden change of output should be obtained at the frequency where $\mu_0 = 0$.

Conclusions.—It seems likely that ionospheric focusing sufficient to give a forward gain of 25, and possibly more, could be observed at many points in the orbit of a satellite, between heights of about 350 to 600 km. The chief limitations are the irregularities in the ionosphere, and the narrowness of the receiver bandwidth that must be used. The frequency range is best chosen as

high as is allowed by typical values of the penetration frequency, since the bandwidth limitation is less severe at higher frequencies.

The aerial beam would only apply for one of the two characteristic modes of propagation, but it would be sufficiently narrow (say 20° across) to delineate some of the major features of the galactic radiation. The principal objects of interest here are the spectral indices of the various components, especially the remarkable spur of radiation near galactic longitude $l^{\text{III}}=0$, and also the measurement of the distribution of ionized hydrogen close to the galactic plane, shown by its absorption of the background radiation. It is unlikely that many discrete sources will be detected, since the aerial gain available for focusing is inadequate, but it is possible that enhanced radiation from the Sun will be observed.

Observations from rockets are necessarily limited, but would serve to test the precision expected from ionospheric focusing.

Acknowledgments.—I have been greatly helped in the application of the simple theory to a more realistic ionospheric model by discussions with Dr K. G. Budden and Mr I. N. Capon, who also computed the ray paths for Fig. 6.

*Mullard Radio Astronomy Observatory,
University of Cambridge:
1961 March.*

References

- Budden, K. G., 1961, in preparation.
Costain, C. H., 1960, *M.N.*, **120**, 248.
Haselgrove, C. B., Haselgrove, J., and Jennison, R., 1961, *Proc. Roy. Soc. A.*, **261**, 423.
Hoyle, F., 1960, *M.N.*, **120**, 338.
Shklovsky, I. S., 1952, *Astr. Zhur. U.S.S.R.*, **29**, 418.
Tunmer, H., 1959, *M.N.*, **119**, 184.

THE ROTATION OF BARRED GALAXIES UNDER GRAVITATIONAL FORCES, II

S. Aarseth

(Communicated by F. Hoyle)

(Received 1961 May 4)

Summary

Several models of barred spiral galaxies in rotation under purely gravitational forces are computed. A homology relation is found thereby extending the range of the results available for rotating systems. Approximate formulae are given for the period of rotation and the bar mass in terms of the inner and outer radius and the central mass.

The problem is modified by taking the nucleus to be an oblate spheroid and it is found that the stability of the bar remains approximately the same for eccentricities < 0.5 . It is predicted that the inner bar will develop trailing arms. The mass of the barred system NGC 7479 is estimated to lie in the region $2.4-2.9 \times 10^{10} \odot$.

1. *Introduction.*—The problem of the rotation of a barred spiral galaxy under purely gravitational forces has been dealt with theoretically in a previous paper (1) where one typical model was done by hand calculation. Since then a whole sequence of models has been worked out with the help of the digital computer EDSAC 2.

In this problem we take a spherical nucleus with mass M and radius R_1 . The bar is chosen to be cylindrical with diameter $2a$, and the mass density per unit length is $\rho(r)$. The two diametrically opposite parts of the bar run from $\pm R_1$ to $\pm R_2$. The equation of motion at an axial point r_p in the bar is given by equation (3) of (1);

$$r_p \alpha = \frac{1}{2r_p^2} + \frac{1}{a^2} \left[\int_{R_1}^{r_p} \rho'(r) \left\{ 1 - \frac{r_p - r}{[(r_p - r)^2 + a^2]^{1/2}} \right\} dr \right. \\ \left. - \int_{r_p}^{R_2} \rho'(r) \left\{ 1 + \frac{r_p - r}{[(r_p - r)^2 + a^2]^{1/2}} \right\} dr \right. \\ \left. + \int_{-R_1}^{-r_p} \rho'(|r|) \left\{ 1 - \frac{r_p - r}{[(r_p - r)^2 + a^2]^{1/2}} \right\} dr \right]. \quad (1)$$

Let G be the constant of gravitation and T the period of rotation, then

$$\alpha = \frac{2\pi^2}{GMT^2}. \quad (2)$$

As before we take the density function scaled by M to be

$$\rho'(|r|) = \sum_{n=-2}^2 A_n |r|^n \quad (3)$$

The 5 coefficients A_n are determined by introducing the requirement of uniform rotation at the points

$$r_p = R_1 + \frac{n(R_2 - R_1)}{5}$$

where

$$n = 0, 1, 2, 3, 4.$$

The parameter α and hence the absolute value of the density function $\rho'(r)$ is determined by introducing the same requirement at $r_p = R_2$. The solution of $\rho'(r)$ can be checked, either by using the Stirling-Simpson formula for approximate integration or by computing the forces at intermediate points.

2. *Numerical results.*—The numerical results of the computations for the parameter α and the total bar mass M_b are given in Table I and some of the density functions are drawn in Fig. 1. R_1 is taken to be 3 kpc and two sets of models are included, namely $a = R_1/3$ and $a = R_1/4$.

TABLE I
Numerical results of computed models with $R_1 = 3$ kpc.

R_2	$a = \frac{1}{3}R_1$			$a = \frac{1}{4}R_1$		
	$\alpha \times 10^2$	M_b/M	$\alpha R_2^{3/2}$	$\alpha \times 10^2$	M_b/M	$\alpha R_2^{3/2}$
6	0.6920	0.233	0.1017	0.6799	0.172	0.0999
6.5	0.6166	0.282	0.1022			
7	0.5535	0.331	0.1025			
7.5	0.5002	0.382	0.1027			
8	0.4548	0.433	0.1029	0.4425	0.333	0.1001
8.5	0.4158	0.486	0.1030			
9	0.3818	0.539	0.1031	0.3701*	0.419*	0.0999
9.5	0.3522	0.593	0.1031			
10	0.3261	0.648	0.1031	0.3151	0.508	0.0996

The model marked * has been computed from a homologous model and eqns. (7) and (10).

If the units for M and T are \odot and 10^6 years respectively and the length unit is kpc we have from equation (2)

$$T^2 = \frac{4.39 \times 10^{12}}{M\alpha}. \quad (4)$$

Taking $M = 5 \times 10^{10} \odot$, as a tentative value for the central mass we get T in the range 1.1 to 1.7×10^6 years.

In columns 4 and 7 of Table I $\alpha R_2^{3/2}$ is evaluated and it is seen that we have

$$\alpha R_2^{3/2} = c \quad (5)$$

where c is very nearly constant for one set of models. Also it is easily seen that a linear relation for the bar mass is satisfied to a close approximation, viz.

$$M_b/M = dR_2 + e \quad (6)$$

where d and e are constants for the same values of a and R_1 . The actual deviation from the relations (5) and (6) is very small in the examined range of R_2 .

In Fig. 1 the density distribution in the bar is drawn for the cases $R_2 = 6, 8$, and 10 kpc. The curves for intermediate values of R_2 are of similar form to those shown.

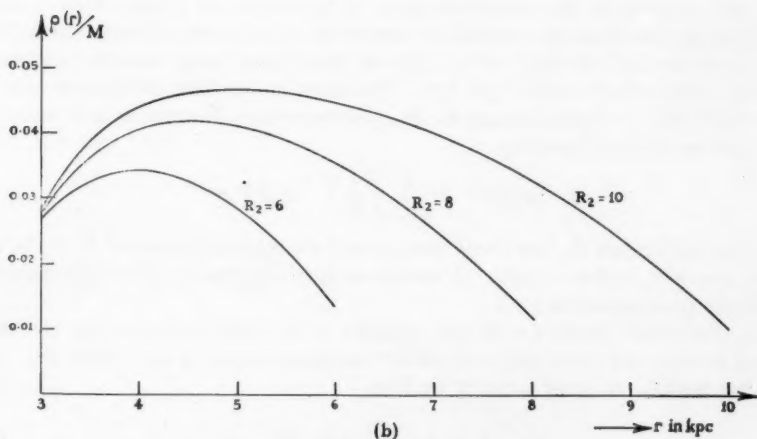
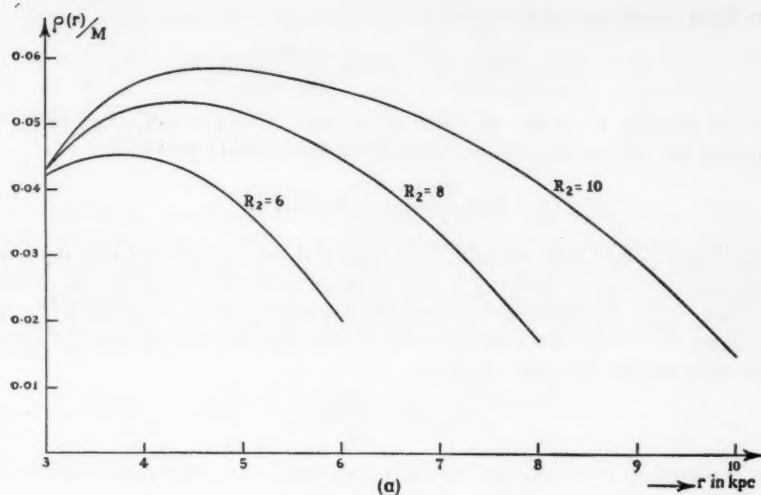


FIG. 1

(a) Scaled density distribution in the bar for 3 models with $a = \frac{1}{3}R_1$.(b) Scaled density distribution in the bar for 3 models with $a = \frac{1}{4}R_1$.

3. *Homology relations.*—Two systems are said to be homologous if they have the same mass and their size is related by a linear scaling factor k . Dimensionally we have that $GMT^2 \propto L^3$ where L is the length unit. Thus for a homologous system of period T and scale factor k we have $T'^2 = k^3 T^2$ and hence from (2)

$$\alpha' = k^{-3}\alpha \quad (7)$$

where α' is the parameter corresponding to α . Writing $k^{-1} R_2'$ for R_2 we then have from equations (4) and (5)

$$T'^2 = \frac{4.39 \times 10^{12}}{M\alpha'} = \frac{4.39 \times 10^{12}}{Mc} k^{3/2} R_2'^{3/2}. \quad (8)$$

For the models $a = 1/3 R_1$ we take $c = 0.1027$. Using $k = R_1'/R_1 = R_1'/3$ and dropping the primes the general formula for the rotation period is

$$T^2 = \frac{8.23 \times 10^{12}}{M} (R_1 R_2)^{3/2}. \quad (9)$$

In the cases of $a = 1/4 R_1$ we take $c = 0.0999$ and the constant 8.23 in (9) should be replaced by 8.46. Hence T is not sensitive to variations in the bar radius.

Since M_b is the same for homologous models equation (6) gives $d'R_2' = dR_2$ and hence $d' = k^{-1}d$. By putting $k = R_1'/3$ and dropping the primes the general expression for the bar mass becomes

$$M_b/M = \frac{3dR_2}{R_1} + e. \quad (10)$$

For the models $a = 1/3 R_1$ we have $d = 0.101$ and $e = -0.375$ and in the cases $a = 1/4 R_1$ the values are 0.082 and -0.320 respectively.

In two homologous models the mass density scales as the cube of the scale factor k . In the bar, however, we are concerned with a mass per unit length, and this scales as k , viz. $\rho'(r') = k^{-1}\rho(r)$. It is immaterial in the latter equation whether the densities are scaled with respect to mass or not, since the mass M is the same for both models. From (3) we then have, using unscaled densities; $\rho'(|r'|) = M \sum A_n' |r'|^n = M k^{-1} \sum A_n |r|^n$. By equating similar coefficients we get $A_n' = k^{-(n+1)} A_n$. Again writing $k = R_1'/3$ we can drop the primes and write for the general density function

$$\rho(|r|) = M \sum_{n=-2}^2 \left(\frac{3}{R_1} \right)^{n+1} A_n |r|^n. \quad (11)$$

The coefficients A_n have been computed for a range of values of R_2 in the two cases $a = 1/3 R_1$ and $a = 1/4 R_1$. A restricted range of density curves are therefore available from equation (11).

4. *Rotational stability.*—It now remains to be examined whether the computed models can retain their shapes for comparatively long time intervals. For the bar force at an axial point r_p we have

$$F_b(r_p) = \sum_{n=-2}^2 f_n(r_p) A_n \quad (12)$$

where the forces $f_n(r_p)$ correspond to terms in $\rho(r)$. We use the determined values of A_n and compute $f_n(r_p)$ at points intermediate to the fitting points. The bar force required for uniform rotation, viz.,

$$r_p \alpha = \frac{1}{2r_p^2},$$

has been compared with equation (12) and the deviations of force obtained.

It was found that the agreement with rigid body rotation is very good everywhere except near the ends of the bar. In Table II the maximum deviation of total force dF/F in the inner and outer bar is given for three representative models.

TABLE II

Maximum deviation of force in inner and outer bar for $R_1 = 3$ kpc and $a = \frac{1}{3}R_1$.

R_2	$-dF/F$	r_p	dF/F	r_p
6	0.25 per cent	3.2	0.05 per cent	5.8
7.5	2.2	3.2	0.1	7.2
9	5.2	3.3	-0.2	8.5

In the above computations a spherical nucleus has been used. The bar mass introduces a force on the matter in the central body which is directed in the outward sense parallel to the bar. Hence a more realistic choice would be to use a slightly flattened nucleus. Taking an oblate spheroid of constant density with major axis R_1 and eccentricity e the attractive force at an exterior point r on the major axis is (2);

$$F(r, e) = \frac{3GM}{2(R_1 e)^3} r [\beta - \sin \beta \cos \beta] \quad (13)$$

where

$$\sin \beta = \frac{R_1 e}{r}.$$

The model $R_1 = 3$ kpc, $a = \frac{1}{3}R_1$, and $R_2 = 3R_1$ was chosen and density functions were computed for a range of e -values. In Fig. 2 $\rho(r)$ is only drawn for two cases; viz. $e = 0$ and $e = 0.5$ since the other curves are very similar.

It is found that the density function and the parameter α are raised with increasing eccentricity, and contrary to expectations the stability in the inner bar is not improved. Between $e = 0$ and $e = 0.5$ the maximum deviation of the required force remains approximately the same and the stability decreases gradually above $e = 0.5$.

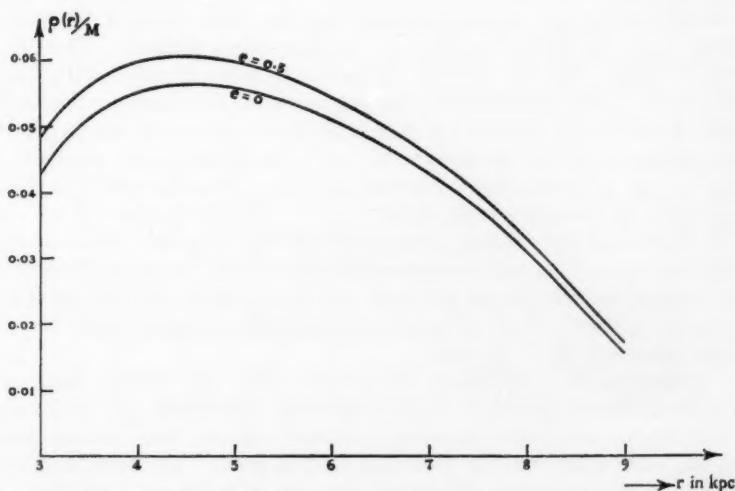


FIG. 2.—Scaled density distribution in the bar for different eccentricity of the nucleus. For $e = 0$, $\alpha = 0.003818$, $M_b = 0.539M$; and, for $e = 0.5$, $\alpha = 0.004030$, $M_b = 0.580M$.

Equation (5) of (1) gives the time deviation from uniform rotation dT after n periods when the relative force deviation is dF/F ;

$$dT \approx -\frac{nT}{2} \cdot \frac{dF}{F}. \quad (14)$$

If we take $dT = 0.1T$ as the stability criterion we get from Table II $n \approx 400, 200$, and 100 respectively for the outer bar. The corresponding times are in the range 4.5 to 1.5×10^{10} years for $M = 5 \times 10^{10} \odot$.

The variation of the lack of force in the inner bar shows that the shortest bar is also the most stable. This lack of force will lead to trailing of matter just outside the nucleus. Indeed, on some photographs the nucleus seems to be wrapped in two symmetrical arms, and their presence has been a puzzling feature of galactic structure (3).

5. *Discussion.*—The existence of an appreciable number of galaxies with a straight bar suggests that the bar is a laterally stable configuration. The transverse velocity of escape from the bar can be estimated as follows. The potential due to a cylinder of length $2l$ and with mass per length ρ is

$$V \approx -2G\rho \ln \frac{a}{2l} \quad (15)$$

at a point in the middle when the axial distance is a and $a \ll l$. For the velocity of escape v we then have; $\frac{1}{2}v^2 \approx V$. If we take $a = 1$ kpc and $2l = 6$ kpc, this gives $v \sim 250$ km sec $^{-1}$ when $M = 5 \times 10^{10} \odot$. For comparison, the orbital velocity at say 6 kpc is 240 km sec $^{-1}$. The relative velocity of escape from the bar is thus higher than one might have suspected and much higher than the transverse components that are likely to exist in the bar. Hence the stars in a bar will remain in the bar.

In none of the computed models do we have that $\rho(|R_2|) \rightarrow 0$ which is a requirement of physical continuity. A small mass element situated immediately outside the end of the bar will be subject to a smaller attractive force than if it were at the end point. Given a circular velocity with period T the matter in question would lag behind the bar in the subsequent rotation. Thus a small amount of matter added to the ends of the bar in order to make $\rho(|R_2 + dr|) = 0$ would lead to trailing arms without affecting much the conditions in the bar itself.

Barred galaxies are observed to have trailing arms of matter starting from the sudden disappearance of the straight bar and in some cases they extend to form a more or less complete ring. Furthermore, it is also observed that the arms emerge from the bar at an angle of nearly $\pi/2$. The composition of the trailing arms is not known but analogy with normal spirals suggests a predominance of gas and dust whereas the main contents of the bar may well be in the form of stars. At the ends of the bar the gas and dust may be squeezed out and trailing arms would then develop. The influence of such trailing matter would be to start breaking down the bar at its ends.

6. *Application to NGC 7479.*—Since this paper was written some observations of the barred galaxy NGC 7479 have been published (4). It is reported that a linear relation exists between rotational velocity and central distance out to the point where the bar turns into trailing arms. The total length of the bar is 18.5 kpc for an assumed Hubble's constant of 75 km sec $^{-1}$ per Mpc. The reduced circular velocity at the ends of the bar is found to be 220.8 km sec $^{-1}$, making the period of rotation $\approx 257 \times 10^6$ years. With T and R_2 known we can

use equations (9) and (10) to determine the total mass of the system provided that an estimate can be given for R_1 and a .

From the photograph and a drawn isophote $R_1 \approx 1/3 R_2$ and $a \approx 1/3 R_1$. Equation (9) now gives $M \approx 1.9 \times 10^{10} \odot$. The total mass is then

$$M + M_b \approx 2.9 \times 10^{10} \odot,$$

neglecting the mass and influence of the trailing arms. Burbidge *et al.* got a total mass of $2.20 \times 10^{10} \odot$ on the simple model of an oblate spheroid of constant density rotating about the minor axis.

The value of the total mass is only changed slightly if we use a different value for a or take the nucleus to be an oblate spheroid. Furthermore, choosing $R_1 = 2.5$ kpc instead, the total mass becomes $2.4 \times 10^{10} \odot$; the dependence of the mass upon R_1 is therefore not very sensitive. By writing $T = 2\pi R_2 v^{-1}$ in (9), where v is the circular velocity, it is seen that the derived mass depends linearly on the adopted distance of the galaxy.

The writer wishes to express his thanks to the staff of Cambridge University Mathematical Laboratory for the use of EDSAC 2 and to Professor F. Hoyle for valuable discussions on the contents of this paper.

Fitzwilliam House,
Cambridge:
1961 March

References

- (1) Aarseth, S., *M.N.*, **121**, 525, 1960.
- (2) Schmidt, M., *B.A.N.*, **13**, 15, 1956.
- (3) Hoyle, F., *Frontiers of Astronomy*, Chapter 16. London: Heinemann, 1955.
- (4) Burbidge, E. M., and G. R., Prendergast, K. H., *Ap. J.*, **132**, 654, 1960.

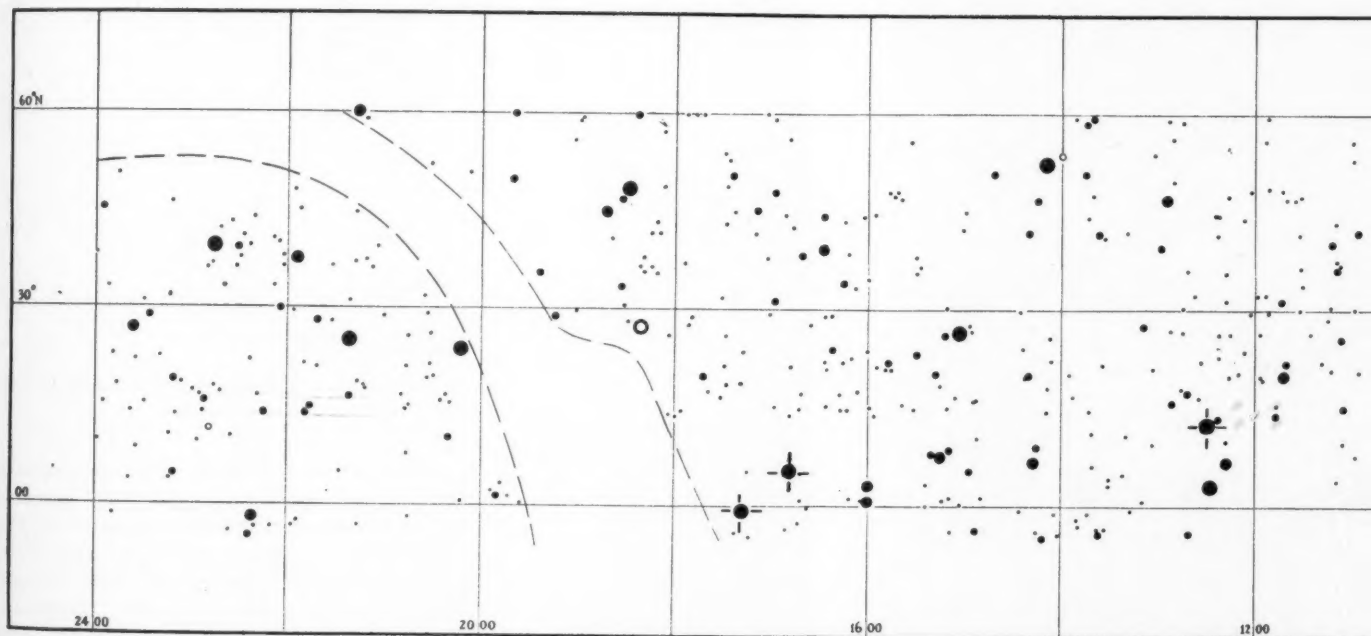
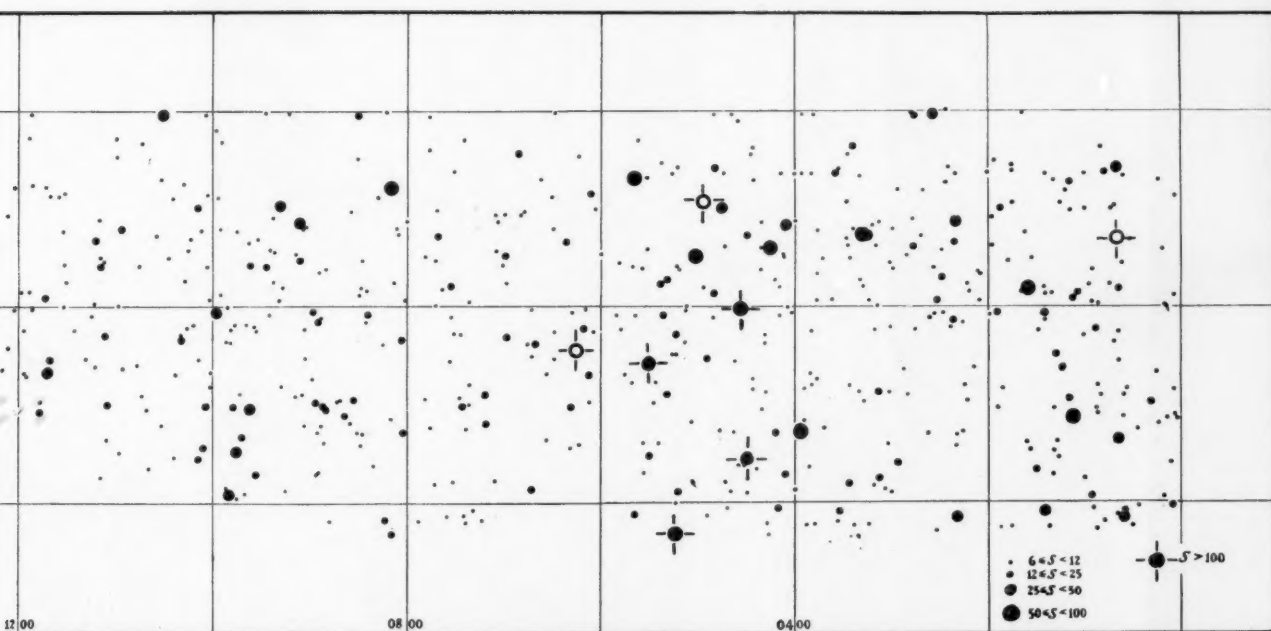


FIG. 7.—Map showing the positions of all sources observed. Open circles indicate



in circles indicate sources with angular diameters greater than $10'$ arc.